

# 修 士 論 文

## 題 目

ミューオン電子転換実験による放射線環境下における超  
伝導ソレノイドに関する研究

指導教員 石橋 健二 教授

執行 信寛 助教

荻津 透 教授

吉田 誠 助教

九州大学大学院工学府エネルギー量子工学専攻

氏名 楊 叶

提出年月 平成27年2月



# Contents

<b>1</b>	<b>Introduction</b>	<b>1</b>
1.1	Charged lepton flavor violation . . . . .	1
1.2	Searches for cLFV with muon . . . . .	2
1.2.1	$\mu \rightarrow e\gamma$ . . . . .	2
1.2.2	$\mu \rightarrow eee$ . . . . .	3
1.2.3	$\mu \rightarrow e$ conversion . . . . .	3
1.3	COMET experiment . . . . .	4
1.3.1	Proton beamline . . . . .	5
1.3.2	Signal of $\mu^- N \rightarrow e^- N$ conversion . . . . .	6
1.3.3	Background of $\mu^- N \rightarrow e^- N$ conversion . . . . .	7
1.4	Objetive . . . . .	8
<b>2</b>	<b>Superconducting solenoid system for COMET experiment</b>	<b>9</b>
2.1	Superconducting magnet system . . . . .	9
2.2	Pion capture solenoid . . . . .	10
2.2.1	Coils structure . . . . .	10
2.2.2	Production target . . . . .	12
2.2.3	Radiation shield . . . . .	12
2.2.4	Quench protection system . . . . .	12
2.3	Muon transport solenoid . . . . .	14
2.4	Detector solenoid . . . . .	15
<b>3</b>	<b>Radiation estimation</b>	<b>17</b>
3.1	Hadronic models . . . . .	17
3.1.1	PHITS . . . . .	17
3.1.2	FLUKA . . . . .	18
3.1.3	GEANT4 . . . . .	18
3.2	Modification of PHITS code . . . . .	18
3.2.1	Proton beam . . . . .	18
3.2.2	Magnetic field . . . . .	19
3.3	Prompt radiation . . . . .	20
3.3.1	Physical model comparison . . . . .	20

3.3.2	Geometry	21
3.3.3	Radiation estimation	22
3.4	Residual radiation estimation	24
3.4.1	Residual radiation	24
3.5	Radiation shielding optimization	26
3.5.1	Radiation shield for MS	26
3.5.2	Radiation shield for CS	27
<b>4</b>	<b>Irradiation test for superconducting magnet material</b>	<b>31</b>
4.1	Glass Fiber Reinforced Plastic	31
4.1.1	Experiment	31
4.2	Quench protection diode	33
4.2.1	Experiment	33
4.2.2	Neutron measurement	34
4.2.3	Electrical property of diode	35
4.2.4	Electrical property at cryogenic temperature	37
4.2.5	Forward voltage at 210 A	37
4.3	Insulation tape	38
4.4	Radiation test for conductor	39
4.4.1	Discussion	42
<b>5</b>	<b>Thermal stability of superconducting solenoids</b>	<b>45</b>
5.1	Quench estimation	45
5.1.1	Specific heat	45
5.1.2	Electrical resistivity	48
5.1.3	Thermal conductivity	51
5.1.4	MIITs	52
5.2	Cooling estimation	54
5.2.1	Geometry	54
5.2.2	Heat generation	55
5.2.3	Maximum temperature of cooling	56
5.2.4	Discussion	58
<b>6</b>	<b>Conclusion</b>	<b>61</b>
<b>Acknowledgement</b>		<b>63</b>
<b>References</b>		<b>65</b>
<b>Michel decay</b>		<b>69</b>
<b>cLFV in Standard Model</b>		<b>71</b>

<b>cLFV in supersymmetry</b>	<b>73</b>
<b>Impact of cLFV</b>	<b>77</b>
<b>Magnetic field interpolation</b>	<b>79</b>



# List of Figures

1.1	SINDRUM-II experiment observes a $\mu^- + Ti \rightarrow e^- + Ti$ conversion with branching ratio of $7 \times 10^{-13}$ . Two signal is founded in high energy region but it is out of the range of $\mu^- \rightarrow e^-$ signal. . . . .	3
1.2	A schematic layout of COMET. 8 GeV proton from B-line hits the target and produce pion first, these pions are captured by pion capture solenoid, and decays to muons in muon transport solenoid. Then, the muon with low momentum is captured by stopping target, meanwhile, an electron with 105 MeV/c from $\mu \rightarrow e$ conversion will be transported to E-cal to take a measurement by detector solenoid. . . . .	4
1.3	Dedicated proton beamline for COMET experiment. A new proton beamline, B-line is under construction. COMET Hall is located beside Hadron Hall. . . . .	5
1.4	The time concept of proton beam. The time window will open from 700 nsec to take data. . . . .	6
2.1	Schematic layout of superconducting magnet system for COMET phase-I experiment. . . . .	9
2.2	Coil and conductor structure of CS1. . . . .	11
2.3	Schematics of quench protection circuit. . . . .	13
2.4	Schematics of quench protection system for pion capture solenoid. . . . .	13
3.1	The physical model used in PHITS code. Default hadronic model is JAM_INCL4.6_JENDL, moreover, JAM_BERT_JENDL and JAM_INC-ELF_JENDL are able to be selected in PHITS code. . . . .	17
3.2	Proton beam distribution simulated by TURTLE code. Top two are the momentum distribution of x and y axis, respectively. Bottom two are the momentum distribution and spatial distribution. Here, intensity means the normalized intensity. . . . .	19
3.3	Tracking of 100 MeV electron with uniform 5 Tesla field. One electron is injected with angle of 30 degree. Magnetic field is applied in a cylinder with radius of 50 cm and length of 300 cm. . . . .	19
3.4	Magnetic field map of phase-I experiment used in PHITS simulation. It is calculated by FEM with iron yoke. Mangetic field vector at z = 0 cm is shown on the right. . . . .	20

3.5 Compared the backward particle yield and integral yield with GEANT4 and PHITS. Left one is the backward pion and muon yield, red and blue line represent the yield calculated by QGSP_BERT_G4NDL and JAM_BERT_JENDL respectively. Right one shows the integral yield of pion and muon from target, red and blue point are the result of QGSP_BERT_G4NDL and JAM_BERT_JENDL. . . . .	21
3.6 COMET phase-I experiment geometry in PHITS simulation. . . . .	21
3.8 Neutron and photon distribution for COMET phase-II experiment. Top two show the neutron distribution from x-z and y-z view. Bottom two are the distribution of photon from x-z and y-z view. . . . .	22
3.9 Energy spectrum of muon, photon and neutron from both experimental hall and beamline at the end of 90 degree bending. Most of neutrons are at the low energy region, and photon are all higher than 10 keV. . . . .	23
3.10 The energy deposition of each magnets in phase-I and phase-II experiment. Black and red point represent the energy deposition of phase-I and phase-II experiment respectively. The energy deposition of phase-II is one order higher than phase-I's, and its peak is located in CS0 coil. . . . .	23
3.11 Residual radiation of vacuum vessel, magnet, radiation shield and iron yoke with 1 month operation and 10 month cooling. . . . .	24
3.12 Activity and peak of dose equivalent of each magnets with 1-month operation and 10-month cooling. . . . .	25
3.13 Compared the residual radiation distribution of pion capture solenoid between PHITS and FLUKA. Left and right represent the PHITS and FLUKA result respectively. . . . .	25
3.14 The concept of COMET radiation shield. It consists of tungsten alloy, stainless steel and copper. Tungsten ally and stainless steel are employed on the high and low radiation side respectively. On the downstream of target, copper is used. Right figure shows the distribution of neutron from x-y view. Azimuthal angle is also defined in here. The peak of neutron flux is located at 180 degree of CS coils. . . . .	28
3.15 Compared the azimuthal DPA and energy deposition of middel part of CS1 coil in different verion of shielding design. The long CS1 coil is cut to 3 parts along the z axis and 12 parts along the azimuthal axis. . . . .	28
3.16 High energy neutron ( $E \geq 0.1$ MeV) along the azimuthal direction of CS1 coils. . . . .	29
3.17 A relation of muon and pion yield with shielding backward radius. Current shielding backward radius is 36 cm. Black line: $\mu^-$ , red line: $\pi^-$ , blue line: $\mu^- + \pi^-$ . . . . .	30
 4.1 GFRP samples before the irradiation are shown on the left. The samples are tensioned until break after irradiation (right). . . . .	32
4.2 The tensile strength of irradiated samples (G10, CE, BMI and BT) when it breaks. Left and Right figure represent 1 MeV electron irradiation test in JAEA, Takasaki and 30 MeV electron irradiation test in LINAC, KURRI. . . . .	32
4.3 Sample setup for neutron irradiation test. Diode is set up in front of MPPC, APD, Artix-7 and ROESTI where is 30 cm far from the neutron production target. . . . .	33

4.4	The detection efficiency is calibrated by using $^{152}\text{Eu}$ radiation source. Several peak of $^{152}\text{Eu}$ is fitted as convolution on left, and the detection efficiency of HPGe is fitted on right. . . . .	34
4.5	Neutron flux is measured by Au wire, Al and Ni foils. The comparison of experimental data with simulation (left). The neutron flux on the place where samples are set up is shown on right. . . . .	35
4.6	The temperature during the irradiation (left). The turn-on voltage decreases with the neutron fluence (right). . . . .	36
4.7	Measured turn-on voltage for quench protection diode. It is fitted as diode V-I function. Black and green point represent the original V-I curve and V-I curve after $10^{12} \text{ n/m}^2$ irradiation. . . . .	36
4.8	Measurement of the forward voltage of diode at cryogenic temperature. . . . .	37
4.9	Relative increase of the forward voltage versus neutron fluence at room temperature. . . . .	38
4.10	Forward V-I curve measured at room temperature and nitrogen temperature without irradiation (left). The measurement of turn-on voltage at 100 mA from room temperature to 77 K (right). . . . .	38
4.11	Insulation tape is made of glass cross and polyimide film impregnated by BT and epoxy resin (left). The two pieces of insulation tapes are sandwiched with aluminum strip to take tensile test (right). . . . .	39
4.12	3 samples of each BTGU, BTGK-A, BTGK-B and BTGK-C are tensioned without irradiation (left). BTGU shows no degradation after irradiated with 10 MGy at limit by cobalt $\gamma$ ray source. . . . .	39
4.13	all kinds of particles which hit the CS1 coil (left). The displacement cross section of aluminum for neutron (right). . . . .	40
4.14	Neutron spectrum at core of KUR reactor. . . . .	40
4.15	Predicted the RRR-neutron curve from the neutron irradiation test in KUR. . . . .	41
4.16	A relation between DPA and RRR. . . . .	43
5.1	The specific heat of aluminum is fitted from the range from 4.5 K to 22.67 K, 22.67 K to 46 K and 46 K until 350 K respectively. . . . .	46
5.2	Fitted copper specific heat curve. . . . .	47
5.3	Fitted aluminum resistivity. . . . .	49
5.4	Fitted the Kohler plot with experimental data for pure aluminum. . . . .	50
5.5	Thermal conductivity of aluminum with difference RRR. . . . .	51
5.6	The MIITs calculation of CS1 coils with 5.5 Tesla magnetic field and 2700 A current. . . . .	53
5.7	Improvement of power supply according to the results of MIITs estimation. . . . .	53
5.8	Details of the geometry used in magnet thermal simulation. . . . .	54
5.9	Mesh cutting of CS1 coils. . . . .	55
5.10	Calculated the energy deposition distribution with realistic radiation shield geometry. . . . .	55
5.11	Calculated the temperature rising during the operation. . . . .	56
5.12	Maximum temperature for the original coil structure. . . . .	57
5.13	The maximum temperature against the operation time. . . . .	58
5.14	the thermal conductivity dependance of insulation tape. . . . .	58

5.15	The temperature peak increases linearly with the energy deposition factor.	59
5.16	The CS1 coils can be optimized by imcreasing the thickness of aluminium strip.	59
5.17	The scenario of CS1 seperating.	60
1	Feynman diagram of $\mu^- \rightarrow e^- \gamma$ predicted by massive neutrino. cLFV occurs through a neutrino oscillation, and $\gamma$ is emitted from a $W^-$	71
2	Feynman diagram of $\mu^- \rightarrow e^- \gamma$ predicted by slepton mixing. it occurs through its superpartner $\tilde{\mu}$ and $\tilde{e}$ mixing.	73
3	Pridiction of branching ratio of $\mu \rightarrow e$ conversion in SUSY-GUT SU(5). Mass of right-hand $\tilde{e}$ can be observed indirectly if the $\mu \rightarrow e$ conversion experiment gets more precision sensitivity.	74
4	Prediction of branching ratio of $\mu \rightarrow e\gamma$ in SUSY-Seasaw model.	75
5	<i>The size of the observable flavor effect for a variety of SUSY and non-SUSY models.</i>	77

# List of Tables

1.1	Decay modes and branching ratio of muon.	2
1.2	History of $\mu^- \rightarrow e^-$ conversion experiments.	3
1.3	Current running muon beamline around the world. Current most intense muon beamline is in PSI, COMET muon beamline will be 3 orders higher than PSI muon beamline.	5
1.4	Different requirement of proton beam in phase-I and phase-II.	6
1.5	Potential backgrounds for searching $\mu^- N \rightarrow e^- N$ conversion.	7
2.1	Details of coils for pion capture solenoid.	10
2.2	Details of design parameters for capture solenoid magnet.	11
2.3	Design parameters of transport solenoid.	14
2.4	Coils parameters for muon transport solenoid.	15
3.1	Comparison of PHITS with GEANT4. $\sigma$ represents (G4-PHITS)/PHITS.	20
3.2	Residual radiation of vacuum vessel between CS0 and iron yoke.	25
3.3	Compared the residual radiation along the z axis. z=0 is at the production target, z=-300 is 3 m far from the target on upstream of target, z=300 is 3 m far from the target on downstream of target, and z=-500 is 5 m far from the target.	26
3.4	Maximum residual radiation after cooling for 10 months, 1.75 year and 2 years.	26
3.5	Heat load of stainless steel and copper shield.	27
3.6	Activated isotopes of copper (left) and stainless steel (right).	27
3.7	Material property of tungsten alloy (AN-1800).	28
3.8	Details of the shielding design. CS1 is cut to 3 parts along the z axis, 12 parts along the azimuthal direction.	29
4.1	Neutron activation reactions.	34
4.2	Fitting parameters for detection efficiency.	35
4.3	Fitting parameters for V-I curve.	36
4.4	Fitting parameters for forward voltage of diode at 300 K and 77 K.	37
4.5	Factor for the neutron induced resistivity.	41
4.6	Details of RRR degradation for pion capture solenoid after 280-day operation.	41
4.7	DPA estimation for the neutron irradiation test of pure aluminum.	42

4.8	The Frenkel pair resistivity $\rho_{FP}$ of aluminum. Methods of the data derivation: Exp D is X-ray diffraction method, Exp T is the threshold energy determination for electron irradiation of single crystals at low temperature. Exp T(p) is for the electron irradiation of polycrystals, Evl S is the estimation made with the help of the systematics <sup>(1)</sup> . . . . .	42
5.1	The details for fitting the aluminum specific heat. . . . .	47
5.2	Fitting parameters for copper specific heat. . . . .	47
5.3	The fit parameters for NbTi specific heat. . . . .	47
5.4	NIST fitting parameters for copper electrical resistivity. . . . .	48
5.5	NIST fitting parameter for pure aluminum. . . . .	50
5.6	Hust fitting parameter for pure aluminum. . . . .	50
5.7	Fitting parameters for pure aluminum magnetoresistivity. . . . .	51
5.8	Fitting parameters for copper magnetoresistivity. . . . .	51
5.9	The parameters for MIITs estimation of CS1. . . . .	52
5.10	Heat generation for the capture solenoid. . . . .	55
5.11	Parameter setting in thermal estimation of CS1 coils. . . . .	56
5.12	Meshing set in thermal analysis of CS1 coils. . . . .	56

# Chapter 1

## Introduction

Although the Higgs boson has been found in 2012 by CMS and ATLAS collaboration <sup>(2)</sup>, there are no clues of new physics in last running with 3.5 TeV per beam. the Standard Model still remains many unsolved problems such as neutrino oscillation, the lack of dark matter candidate, fine-tuning and matter anti-matter asymmetry. On the other hand, it is known that the quarks and neutrinos are mixing as the Cabibbo-Kobayashi-Maskawa (CKM) matrix and Pontecorvo-Maki-Nakagawa-Sakata (PMNS) matrix, respectively <sup>(3)</sup>. However, as the same family with neutrino, it is strange that charged lepton flavor violation (cFLV) is still not founded. As the prediction of lower branching ratio from the physics beyond the Standard model (BSM), new physics is possible to be probed through the cLFV.

Coherent muon to electron transition (COMET) experiment is planning to seek the cLFV channel of  $\mu^- N \rightarrow e^- N$  from 2017. To achieve the better sensitivity, the most intense muon beamline in J-PARC is under designing and construction.

### 1.1 Charged lepton flavor violation

In Standard Model, the neutrino oscillation is constricted and massless, in addition, the lepton number is totally conserved when they decay, like

$$\begin{aligned} \mu^- &\rightarrow e^- + v_\mu + \bar{v}_e \\ L_\mu : & \quad 1 \quad 0 \quad 1 \quad 0 \\ L_e : & \quad 0 \quad 1 \quad 0 \quad -1 \end{aligned}$$

where the electron lepton number  $L_e$  and muon lepton number  $L_\mu$  on left side is conserved on right side. This decay is the ordinary muon decay and also called Michel decay. However this is not the only decay for muon, all kinds of muon decay is listed in table 1.1 <sup>(4)</sup>.

Unlike to the michel decay, decay mode of charged lepton like  $\mu^- \rightarrow e^- \gamma$  has very tiny probability of decay, observely, its electron and muon lepton number are not conserved on two sides. The branching ratio predicted by standard model is less than  $10^{-54}$ , which the details are described in Appendix. Otherwise, the physics beyond the standard model such as SUSY-Seasaw, SUSY-GUT etc. predicts the branching ratio higher than  $10^{-15}$ , which is possible to be obversed. The reaction like this is called charged lepton flavor

violation.

Decay modes	Fraction ( $\Gamma_i/\Gamma$ )	Confidence level	Reference
$\mu^- \rightarrow e^- \bar{\nu}_e \nu_\mu$	$\approx 100\%$	$1.4 \pm 0.4\%$	(5)
$\mu^- \rightarrow e^- \bar{\nu}_e \nu_\mu \gamma$	$1.4 \pm 0.4\%$		
$\mu^- \rightarrow e^- \bar{\nu}_e \nu_\mu e^+ e^-$	$3.4 \pm 0.4 \times 10^{-5}$		
Flavor violating modes			
$\mu^- \rightarrow e^- \nu_e \bar{\nu}_\mu$	$< 1.2\%$	90 %	(6)
$\mu^- \rightarrow e^- \gamma$	$< 2.4 \times 10^{-12}$	90 %	(7)
$\mu^- \rightarrow e^- e^+ e^-$	$< 1.0 \times 10^{-12}$	90 %	(8)
$\mu^- \rightarrow e^- \gamma \gamma$	$< 7.2 \times 10^{-11}$	90 %	

Table 1.1: Decay modes and branching ratio of muon.

## 1.2 Searches for cLFV with muon

$\mu \rightarrow e\gamma$ ,  $\mu \rightarrow eee$  and  $\mu \rightarrow e$  conversion are three main decay modes for cLFV seeking, and each mode has its different view in  $\mu \rightarrow e$  transition. In these modes,  $\mu \rightarrow e\gamma$  and  $\mu \rightarrow eee$  belong to a dipole-type like interaction, however,  $\mu \rightarrow e$  conversion is a four-fermion like interaction. The effective Lagrangian which includes both dipole-type and four-fermion operators is given by (9).

$$\mathcal{L} = \frac{1}{1 + \kappa} \frac{m_\mu}{\Lambda^2} \bar{\mu}_R \sigma^{\mu\nu} e_L F_{\mu\nu} + \frac{\kappa}{1 + \kappa} \frac{1}{\Lambda^2} (\bar{\mu}_L \gamma^\mu e_L) (\bar{q}_L \gamma_\mu q_L) \quad (1.1)$$

where  $\kappa$  is a parameter which governs the relative size of dipole-type and four-fermion operators. Parameter  $\Lambda$  represents the effective mass (energy) scale of new physics. The first and second term of this equation are meant to the dipole-like ( $\kappa \ll 1$ ) and four-fermion interaction ( $\kappa \gg 1$ ), which correspond to  $\mu \rightarrow e\gamma$  and  $\mu \rightarrow e$  conversion, respectively.

### 1.2.1 $\mu \rightarrow e\gamma$

$\mu \rightarrow e\gamma$  is a 2-body back-to-back decay with monoenergetic  $e$  and  $\gamma$ . The way to search this decay is to reconstruct these back-to-back monoenergetic  $e$  and  $\gamma$ . The earliest  $\mu \rightarrow e\gamma$  search dates back to 1947 with branching ratio of 0.1 (90% C.L.) (10), and the most recent experiment for seeking this mode is the MEG experiment.

MEG experiment searches the  $\mu^+ \rightarrow e^+ \gamma$  in Paul Scherrer Institute (PSI) with  $3 \times 10^7 \mu^+/sec$ . The data is taken from 2009 to 2010, and MEG experiment is now under upgrading to the phase-II experiment. As the result, MEG collaboration presents a new upper limit on the branching ratio of this decay of  $5.7 \times 10^{-13}$  (90% C.L.) with  $3.6 \times 10^{14}$  stopped muons on target (11).

Unfortunately, with the branching ratio of  $5.7 \times 10^{-13}$ , there is no signal of interest founded finally. The MEG-II experiment will start data-taking from 2016 to 2019 with 180 days per year and aim to reach the branching ratio of  $6 \times 10^{-14}$  (12).

### 1.2.2 $\mu \rightarrow eee$

The first experiment for searching  $\mu \rightarrow eee$  decay is taken in 1958 at Nevis cyclotron with the branching ratio of  $3.0 \times 10^{-5}$ <sup>(13)</sup>. Recent best branching ratio is  $10^{-12}$  which is measured by SINDRUM-I experiment. A new experiment called Mu3e purposes to start from 2016 to reach a branching ratio of  $< 10^{-16}$  with the requirement of muon stop rate of about  $2 \times 10^9 \mu^+/\text{sec}$ . Mu3e has two phases, which phase-I and phase-II will take in  $\pi E5$  beamline and HiMB beamline of PSI respectively.

Unlike to  $\mu \rightarrow e\gamma$  decay,  $\mu^+ \rightarrow e^+e^+e^-$  is a 3-body decay. The reconstruction of signal of positron and electron must be from the same vertex. Thus, the challenges of Mu3e are the vertex, timing and momentum resolution<sup>(14)</sup>.

### 1.2.3 $\mu \rightarrow e$ conversion

$\mu \rightarrow e$  conversion is a different process from the other two, because the processes of  $\mu \rightarrow e\gamma$  and  $\mu \rightarrow eee$  are detector-limited owing to accidental background, whilst, the  $\mu \rightarrow e$  conversion has no accident background but the background from beam, which depends on the beam qualities. The past experiments for searching  $\mu^- \rightarrow e^-$  conversion is listed in table 1.2.

Target	Upper limit	Place/Collaboration	Year
Cu	$< 1.6 \times 10^{-8}$	SREL	1972
<sup>32</sup> S	$< 7 \times 10^{-11}$	SIN	1982
Ti	$< 1.6 \times 10^{-11}$	TRIUMF	1985
Ti	$< 4.6 \times 10^{-12}$	TRIUMF	1988
Pb	$< 4.9 \times 10^{-10}$	TRIUMF	1988
Ti	$< 4.3 \times 10^{-12}$	PSI/SINDRUM II	1993
Pb	$< 4.6 \times 10^{-11}$	PSI/SINDRUM II	1996
Ti	$< 6.1 \times 10^{-13}$	PSI/SINDRUM II	1998
Au	$< 7 \times 10^{-13}$	PSI/SINDRUM II	2006

Table 1.2: History of  $\mu^- \rightarrow e^-$  conversion experiments.

The most precision branching ratio is measured by SINDRUM-II experiment with gold target at PSI. As shown in figure 1.1, there is one event found at high momentum region, but it just outside the region of interest.

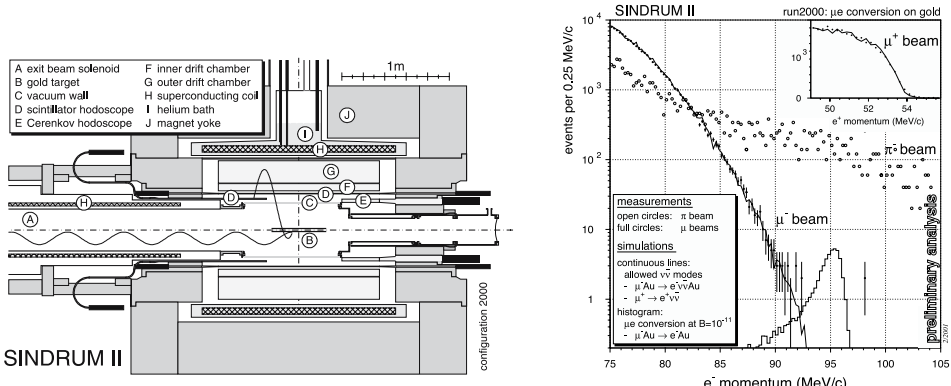


Figure 1.1: SINDRUM-II experiment observes a  $\mu^- + Ti \rightarrow e^- + Ti$  conversion with branching ratio of  $7 \times 10^{-13}$ . Two signal is founded in high energy region but it is out of the range of  $\mu^- \rightarrow e^-$  signal.

COMET and Mu2e experiment are aiming to achieve the branching ratio less than  $10^{-17}$ , which is 4 orders less than the previous experimental result.

### 1.3 COMET experiment

The COMET experiment is designed to search the following  $\mu \rightarrow e$  conversion and be carried out at J-PARC.

$$\mu^- + N(A, Z) \rightarrow e^- + N(A, Z) \quad (1.2)$$

It has two steps for searching cLFV, which are phase-I and phase-II. phase-I experiment is to measure the background and search for cLFV because the  $\mu \rightarrow e$  conversion totally depends on the beam qualities. phase-II experiment is to search the  $\mu \rightarrow e$  conversion with the sensitivity of  $3 \times 10^{-17}$ . As shown in figure 1.2, 8 GeV proton hits the target to produce pions, then these pions are captured by magnetic field and transported to the stopping target to generate the signal of  $\mu \rightarrow e$  conversion. The background measurement is taken at the end of 90 degree bending.

To achieve the experimental sensitivity of  $3 \times 10^{-17}$  which corresponds to the branching ratio, a total  $2 \times 10^{18}$  muons stopped in stopping target is needed. Thus, the high intense muon source with about  $10^{11} \mu^-/\text{sec}$  is required for COMET experiment. As for COMET experiment, one COMET dedicated beamline is under construction in J-PARC.

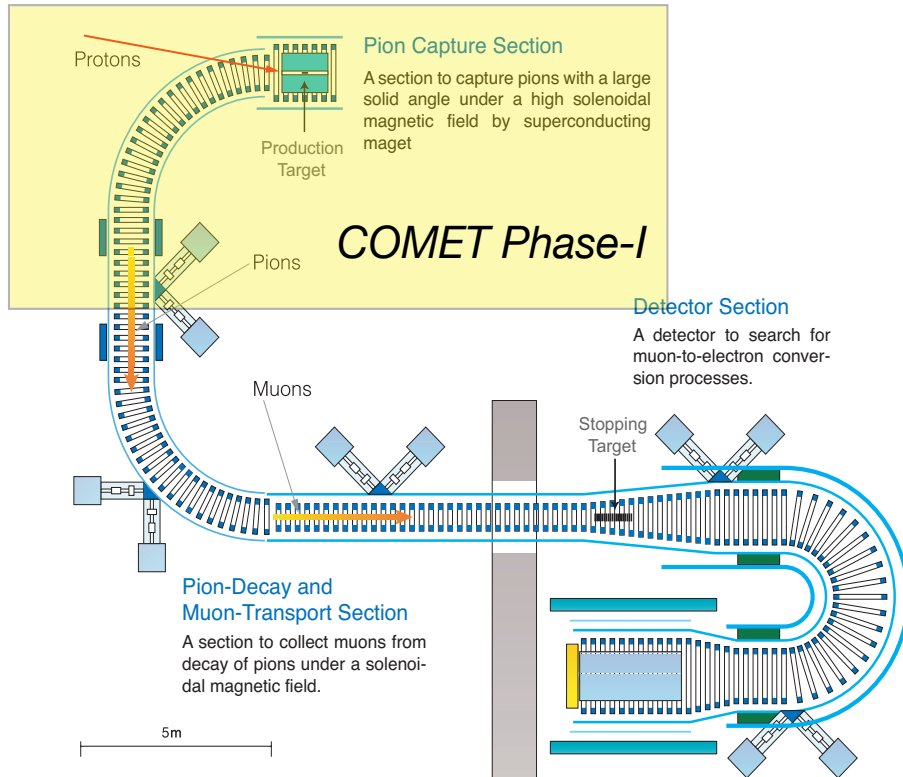


Figure 1.2: A schematic layout of COMET. 8 GeV proton from B-line hits the target and produce pion first, these pions are captured by pion capture solenoid, and decays to muons in muon transport solenoid. Then, the muon with low momentum is captured by stopping target, meanwhile, an electron with 105 MeV/c from  $\mu \rightarrow e$  conversion will be transported to E-cal to take a measurement by detector solenoid.

### 1.3.1 Proton beamline

To obtain the more precision branching ratio of  $\mu \rightarrow e$  conversion, more stopped muon is required. Stopped muon can be gained from two ways, increasing the operating time and increasing the muon beam intensity. Since the most intense muon beamline over the world is located in PSI, and it only provides the muon with  $4 \times 10^8$ , a new high intense muon beamline is necessary for future particle physics. Table 1.3 lists the current and future muon beamline, apparently, COMET muon beamline will be the most intense muon beamline over the world in future.

Lab/Beamline	Energy and power	Present $\mu$ rate [Hz]	Future $\mu$ rate [Hz]
<b>PSI:</b>			
LEMS	590 MeV, 1.3 MW, DC	$4 \times 10^8$	
$\pi$ E5	590 MeV, 1.3 MW, DC	$1.6 \times 10^8$	
HiMB	590 MeV, 1 MW, DC		$4 \times 10^{10} (\mu^+)$
<b>J-PARC:</b>			
MUSE D-line	3 GeV, 1 MW, Pulsed	$3 \times 10^7$	
MUSE U-line	3 GeV, 1 MW, Pulsed		$4 \times 10^8 (\mu^+)$
COMET	8 GeV, 56 kW, Pulsed		$> 10^{11} (\mu^-)$
<b>FNAL:</b>			
Mu2e	8 GeV, 25 kW, Pulsed		$5 \times 10^{10} (\mu^-)$
<b>TRIUMF:</b>			
M20	500 MeV, 75 kW, DC	$2 \times 10^6$	
<b>KEK:</b>			
Dai Omega	500 MeV, 2.5 kW, Pulsed	$4 \times 10^5$	
<b>RAL-ISIS:</b>			
RIKEN-RAL	800 MeV, 160 kW, Pulsed	$1.5 \times 10^6$	
<b>RCNP:</b>			
MUSIC	400 MeV, 400 W, Pulsed	$10^8 (\mu^+)$	
<b>DUBNA:</b>			
Phasatron Ch: I-III	660 MeV, 1.65 kW, Pulsed	$3 \times 10^4$	

Table 1.3: Current running muon beamline around the world. Current most intense muon beamline is in PSI, COMET muon beamline will be 3 orders higher than PSI muon beamline.

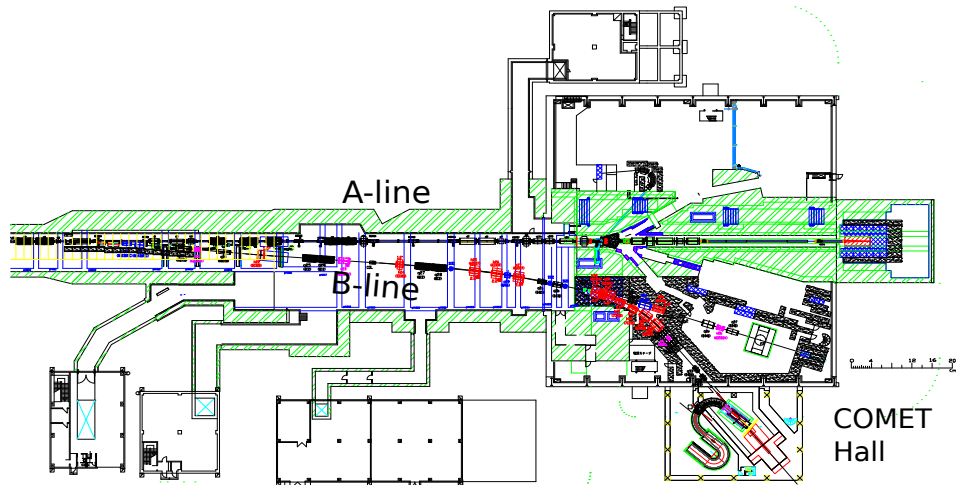


Figure 1.3: Dedicated proton beamline for COMET experiment. A new proton beamline, B-line is under construction. COMET Hall is located beside Hadron Hall.

To accommodate the COMET experiment, a new beamline (B-line) is under construction. As shown in figure 1.3, A-line is the existing beamline from the main ring into the Nuclear and Particle Physics (NP) Hall. B-line is a dedicated proton for COMET experiment.

Both phase-I and phase-II require a pulsed, 8 GeV proton beam slow-extracted from the J-PARC main ring into COMET experimental hall. The proton beam intensity and production target for phase-I and phase-II is different, which is shown as follows. In table 1.4, the requirement of COMET is compared with Mu2e as well.

COMET	Target	Beam intensity [pps]	Power [kW]	stopped muon [ $\mu^-$ /sec]	Sensitivity
phase-I	graphite	$2.5 \times 10^{12}$	3	$1.30 \times 10^9$	$3.1 \times 10^{-15}$
phase-II	tungsten	$4.4 \times 10^{13}$	56	$> 10^{11}$	$< 3 \times 10^{-17}$

Table 1.4: Different requirement of proton beam in phase-I and phase-II.

### 1.3.2 Signal of $\mu^- N \rightarrow e^- N$ conversion

When the  $\mu^- N \rightarrow e^- N$  conversion is occurred, the event signal of electron is mono-energetic with energy

$$E_{\mu e} = m_\mu - B_\mu - E_{rec} \quad (1.3)$$

where  $m_\mu$  and  $B_\mu$  are mass of muon and bind energy of the 1s monic atom respectively.  $E_{rec}$  is the nuclear recoil energy, which is given by  $E_{rec} \approx (m_\mu - B_\mu)^2 / 2m_N$ . It is very small and can be neglected. The signal depends on the nuclei, for instance, it is 105.0 MeV for Al stopping target. This mono-energetic signal is beyond the background, and one tail behind electron background can be observed in  $\mu^- N \rightarrow e^- N$  conversion.

Since the muon in aluminum have lifetimes of about 864 nsec, a pulsed proton beam with interval time of 1.17  $\mu$ sec is employed to eliminate the prompt background. As shown in figure 1.4, the prompt background like  $\pi^-$  decay is occurred after 100 nsec beyond the proton beam. Due to the long lifetime of muonic atoms, the time window is opened from 700 nsec to distinguish the background events and signal events.

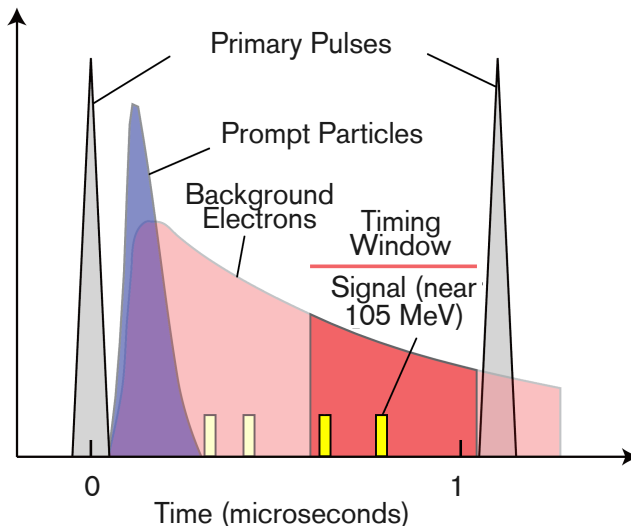


Figure 1.4: The time concept of proton beam. The time window will open from 700 nsec to take data.

The proton beam energy requires a pulsed beam with low production of antiproton and extinction, which will produce the backgrounds. Therefore, the best choice is 8 GeV for COMET experiment, and the its limit intensity is  $4.4 \times 10^{13}$  pps. Antiproton can produce the signal like electron and tracked by CDC when it hits the material. The proton extinction factor is defined as

$$R_{Ext} = \frac{N_{leak}}{N_{pulse}} \quad (1.4)$$

where  $N_{leak}$  is the proton leaked from the pulse, it becomes the background if it comes into the time window, and  $N_{pulse}$  is the proton number in the pulse.

### 1.3.3 Background of $\mu^- N \rightarrow e^- N$ conversion

In COMET experiment, once a  $\mu^-$  with low momentum is captured by nuclei,  $\mu^-$  will transit to the ground state of 1s. During this transition, the specific X-ray is emitted from muonic atom. In addition, the Michel decay in orbit (DIO) emits a electron and dominates the intrinsic background of  $\mu \rightarrow e$  conversion. Without the direct background like DIO, there are many background such as beam related background listed in table 1.5 will cause the indistinguishable signal in CDC during the reconstruction of signal.

Intrinsic physics backgrounds	
Muon decay in orbit	$\mu^- \rightarrow e^- \nu_\mu \bar{\nu}_e$
Radiative muon capture (external)	$\mu^- + A \rightarrow \nu_\mu + A' + \gamma$
Radiative muon capture (internal)	$\mu^- + A \rightarrow \nu_\mu + A' + e^+ + e^-$
Neutron emission	$\mu^- + A \rightarrow \nu_\mu + A' + n$
Charged particle emission	$\mu^- + A \rightarrow \nu_\mu + A' + p$ (or $d$ or $\alpha$ )
Beam related backgrounds	
Radiative pion capture (external)	$\pi^- + A \rightarrow \gamma + A'$ , $\gamma \rightarrow e^- + e^+$
Radiative pion capture (internal)	$\pi^- + A \rightarrow e^+ + e^- + A'$ $e^-$ scattering
Beam electrons	$\mu^-$ decays in flight to produce $e^-$ $\pi^-$ decays in flight to produce $e^-$
Muon decay in flight	$\mu^-$ decays in flight to produce $e^-$
Pion decay in flight	$\pi^-$ decays in flight to produce $e^-$
Neutron induced backgrounds	neutrons hit material to produce $e^-$
Anti-proton induced backgrounds	anti-proton hit material to produce $e^-$
Other background	
Cosmic-ray induced background	
Room neutron induced background	
False tracking	

Table 1.5: Potential backgrounds for searching  $\mu^- N \rightarrow e^- N$  conversion.

### Requirement of magnetic field

Because the background depends on the muon beam quality, to eliminate the background, the muons must be captured and transported to stopping target efficiently, which can be carried out by using superconducting solenoid magnet system. The COMET superconducting magnets must be designed with requirements

- high magnetic field around the production target to capture the pions.
- appropriate magnetic field to transport the low momentum muons to stopping target.

- low magnetic field for detector to track the signal electron.
- smooth magnetic field to eliminate the trapping of charged particles.

The details of magnetic field and superconducting magnet design will be explained in next chapter.

## 1.4 Objetive

The branching ratio of  $\mu^- \rightarrow e^-$  conversion is predicted to around  $10^{-15}$  by the physics beyond the Standard model such as SUSY-GUT, SUSY-Seasaw. To obtain that experimental sensitivity for searching  $\mu^- \rightarrow e^-$  conversion less than  $10^{-17}$ , a 8 GeV,  $4.4 \times 10^{13}$  pps proton beam is employed to produce high intense muon beam of  $10^{11} \mu^-/\text{sec}$  with low momentum.

As the significant part of COMET muon beamline, the pion capture solenoid in superconducting magnet system surrounds a production target with high magnetic field of 5 Tesla and small radius of 672 mm. Its main issue is the radiation, which cause the over-heat and quench of superconducting magnet due to the thermal conductivity degradation of cooling path and stabilizer. Thus, the radiation effects on COMET superconducting solenoid are studied in this thesis.

In chapter 2, the design details of superconducting magnets for COMET phase-I experiment, pion capture solenoid, muon transport solenoid and detector solenoid, will be explained.

In chapter 3, to investigate how much radiation will be produced in COMET experiment, Monte Carlo code is modified to carry out the calculation with COMET condition. Using the real geometry of COMET experiment, the prompt radiation for phase-II and the residual radiation after phase-I experiment is estimated. In addition, one radiation shield is designed for protecting the superconducting coils of pion capture solenoid.

In chapter 4, the radiation resistance of the material and device, GFRPs, quench protection diode, insulation tape and pure aluminum, which are used in COMET superconducting magnet system has been tested.

In chapter 5, considering the thermal conductivity will degrade after irradiation, the most important CS1 coils where close to the production target is under risk of quench and over-heat. Thus, the cooling and quench simulation is estimated.

## Chapter 2

# Superconducting solenoid system for COMET experiment

COMET phase-I experiment is aiming to measure the background and search the  $\mu \rightarrow e$  conversion with the sensitivity of  $10^{-14}$ . Its superconducting magnet system consists of pion capture solenoid, muon transport solenoid and detector solenoid. In phase-II experiment, nowadays' 90 degree bent transport solenoid will be extended to 180 degree curved solenoid, and another spectrometer solenoid will be added.

### 2.1 Superconducting magnet system

Superconducting magnet system plays a key role in pion capture, muon transport and signal tracking. In the case of COMET phase-I experiment, the 8 GeV proton with high intensity is injected into superconducting magnet and hits the target to produce pion, then these backward pions are captured by pion capture solenoid, which provides 5 Tesla magnetic field at peak.

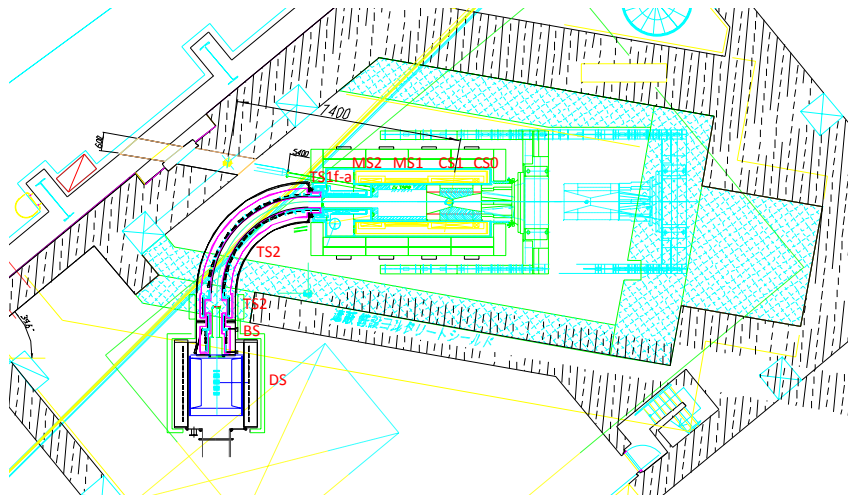


Figure 2.1: Schematic layout of superconducting magnet system for COMET phase-I experiment.

Muons with low momentum from the decay of captured pions are transported to stopping target by the muon transport solenoid with 3 Tesla. Because the high momentum muon and the other particles will cause the background on detector, the muon transport solenoid is designed with 90 degree curve to throw out these

particles. After the muon captured by stopping target, the emitted electron from stopping target will be bent by detector solenoid which provides 1 Tesla magnetic field and tracked in cylindrical drift chamber (CDC).

The schematic layout of COMET superconducting solenoid is given in figure 2.1. Pion capture solenoid consists of CS0, CS1, MS1, MS2 and TS1a-TS1f superconducting coils. Meanwhile, muon transport solenoid includes TS2, TS3 and BS coils, and detector solenoid has 12 DS coils.

## 2.2 Pion capture solenoid

Pion capture solenoid is most critical magnet for capturing the pions from production target with a large solid angle. Considering the valleys of magnetic field causes the trapping of charged particle, the magnetic field distribution must be smooth. The details of the magnetic field of pion capture solenoid is shown in table 2.1.

Coils	$B_z$ [T]	Inner radius [mm]	Outer radius [mm]	Length [mm]	Current [A]	Current density [A/mm <sup>2</sup> ]
CS0	4.0	662	806	175	2700	33.75
CS1	5.0	662	806	1350	2700	33.75
MS1	4.0	662	742	1425	2700	33.75
MS2	3.0	662	774	700	2700	33.75
TS1a	3.0	250	266	200	2700	33.75
TS1b	3.0	250	298	240	2581	32.26
TS1c	3.0	250	314	200	2700	33.75
TS1d	3.0	250	314	200	2619	32.74
TS1e	3.0	250	298	200	2538	31.73
TS1f	3.0	400	496	350	2916	36.45

Table 2.1: Details of coils for pion capture solenoid.

All of the superconducting coils in pion capture solenoid is connected together with the same current provided by one power supply. Furthermore, conduction cooling is employed in whole COMET superconducting magnet system due to the tritium production under high radiation environment by reaction of  $^3\text{He}(n,p)^3\text{H}$ . Also the direct cooling needs helium vessel and the coils must be enlarged, the more radiation and stored energy deposits in larger coils. From all aspect, the conduction cooling is the best choice for COMET superconducting magnet system. Aluminum-stabilized conductors is used in all the coils for reducing the heat load and preventing the over heat of coils after quench.

### 2.2.1 Coils structure

To reduce the energy deposition in coils, superconducting wires are all merged with 5N aluminum (0.1% Ni) due to its low density. The reason why 0.1% nickel is mixed to enhance the mechanical property of conductor.

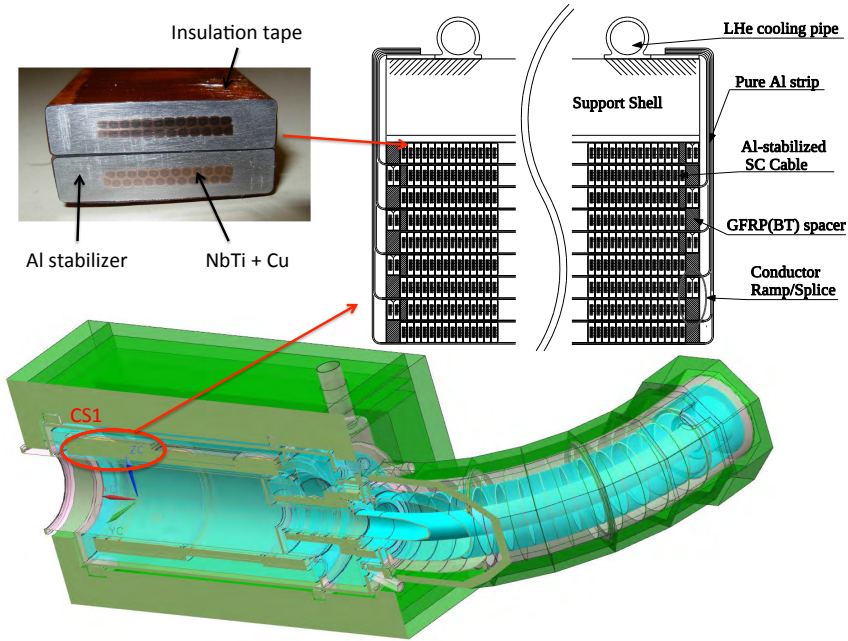


Figure 2.2: Coil and conductor structure of CS1.

The aluminum-stabilized conductor with the size of  $15.0 \times 4.7 \text{ mm}^2$  is wound with two layers of insulation tape, which is made of polyimide film covered by boron free glass with BT and epoxy resin. Here, The reason why BT and epoxy resin is used because it has good mechanical property under the high radiation. In addition, the insulated conductor is impregnated by the BT and epoxy resin mixed with silica filler during the coils winding.

The coil structure of CS1 and detail of design parameters are shown in figure 2.2 and table 2.2 respectively. There are 9 layers superconducting coils totally, and each layer is cooled by inserting 1 mm thick pure aluminum strip with RRR of 2000. Each aluminum strip is installed between two conductor layers, and connected to the liquid helium cooling pipe. Support shell with 5 cm thick is located on the top of superconducting coils to suppress the deformation of coils.

Item	Value
Conductor	Aluminum stabilized SC cable Al:Cu:NbTi = 7.3:0.9:1
Cable dimensions	$15.0 \times 4.7 \text{ mm}^2$ (without insulation) $15.3 \times 5.0 \text{ mm}^2$ (with insulation)
Cable insulation	Polyimide film/Boron-free glass cloth /BT-epoxy prepreg
Magnet length	$\sim 6 \text{ m}$
Number of coils	10
Operation current	2700 A
Max. field on conductor	$5.5 \text{ T}$ ( $T_{cs} = 6.5 \text{ K}$ )
Stored energy	47 MJ
Coil layer	9 (CS0+CS1), 5 (MS1), 7 (MS2), 1~6 (TSa~TS1f)
Quench protection	active quench back heater

Table 2.2: Details of design parameters for capture solenoid magnet.

### 2.2.2 Production target

Production target is to make amounts of pions in the capture solenoid. Phase-I is going to use the IG-43 graphite target rod with length of 60 cm, radius of 2 cm and density of 1.82 g/cm<sup>3</sup>. 3.2 kW proton beam will deposit a heat load of approximately 100 W in the graphite target. The temperature of target grows up to 190°C at peak when 100 W energy is deposited in target. A target support system accurately locates the target within the solenoid inner shield.

To achieve more pion production in COMET phase-II experiment, the target will be changed to pure tungsten rod with length of 16 cm and radius of 0.3 cm after the implementation of phase-I. In addition, due to 56 kW proton beam power, phase-II target must be cooled on low temperature. The proton beam also has to be fitted to a gaussian beam with 0.2 cm radius.

### 2.2.3 Radiation shield

A radiation shield is installed inside the CS and MS coils to protect superconducting coils from radiation. This radiation shield has to be designed for both phase-I and phase-II experiment due to the high residual radiation. The neutron came from production target directly is about  $3 \times 10^{12}$  n/cm<sup>2</sup>/sec in COMET phase-II experiment, which corresponds to  $10^{24}$  n/m<sup>2</sup>. Both NbTi superconducting cable and stabilizers degrade if they are irradiated by neutrons with this order. Therefore, due to a small radius of capture solenoid, a powerful radiation shield is needed to stop or decrease the radiation in short distance. The most ideal radiation shield is made of pure tungsten with density of 19.25 g/cm<sup>3</sup>.

However, to reduce the costs, a new composited radiation shield is designed and the details will be described in next chapter.

### 2.2.4 Quench protection system

Quench is caused by a hot spot in superconducting magnet. When a hot spot quenches, temperature will rise suddenly, and propagate to all magnet. Superconducting magnets has a risk of burn-out at temperature of quench.

Because the current becomes the joule heat after quench, decreasing the current quickly can suppress the temperature rise after quench. There are two ways to speed up the current decay. As shown in figure 2.3, one is to use the dump resistor in superconducting magnet circuit. Once the quench is detected, the power supply will be turned off and current will flow towards to the dump resistor. One quench protection diode is a switch for the quench protection circuit. It is connected with superconducting wire and cooled to 4.2 K during operation. The time constant is written as

$$\tau = \frac{L}{R_{dump}} \quad (2.1)$$

where  $L$  is the inductance of magnets and  $R_{dump}$  is the resistance of dump resistor respectively. Higher resistance of dump resistor makes current decay quicker. In the case of the pion capture solenoid, it is covered by the aluminum stabilizer. Once quench is occurred, the current will flow into the aluminum stabilizer and copper matrix. The current must decay more quickly due to the self resistance of stabilizer

and matrix. The time constant is written as

$$\tau = \frac{L}{R_{dump} + R_{self}} \quad (2.2)$$

Another way is to make the superconducting magnet quench to increase the self resistance by external heater. It needs external power supply to heat the heater.

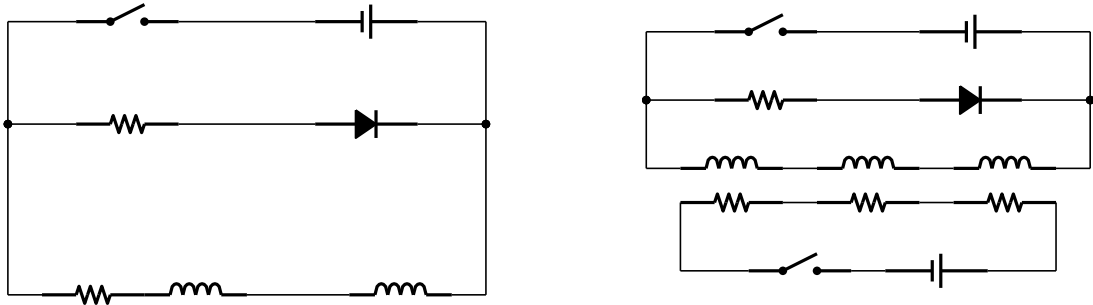


Figure 2.3: Schematics of quench protection circuit.

The quench protection system for pion capture solenoid is shown in figure 2.4. All superconducting magnets in pion capture solenoid are connected together. The power supply for capture solenoid is 2700 A, and 4 reserve trim power supplies and dump resistors are to reduce the current for TS1b, TS1d, TS1e and TS1f. A dump resistor for capture solenoid is  $0.185 \Omega$ , supposed the power supply is 500 V. Once quench is occurred in one of the superconducting magnet of pion capture solenoid, the power supply will be turned off, and quench back heater will heat the all magnets. Total resistivity of pion capture solenoid increases after heated, thus, the current will decay to zero in 1 min.

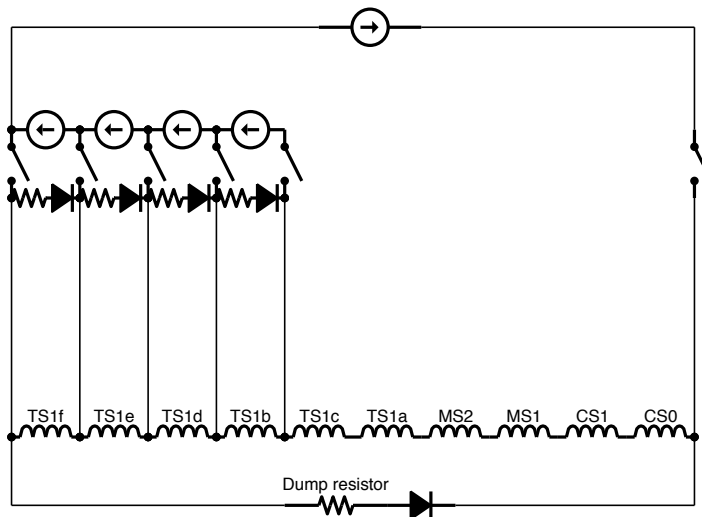


Figure 2.4: Schematics of quench protection system for pion capture solenoid.

## 2.3 Muon transport solenoid

Muons are transported to the stopping target through the muon transport solenoid, which consists of curved superconducting magnets. The muon transport solenoid must be designed to select the muons with low momentum and eliminate muons with high momentum ( $p_{\mu^-} > 75 \text{ MeV}/c$ ), in addition, it also must be long enough for the pion decay. Due to the beam dispersion in muon transport solenoid, the selection of charged particle depends on their momentum. The magnitude of drift is given by

$$D = \frac{1}{qB} \left( \frac{s}{R} \right) \frac{p_L^2 + p_T^2/2}{p_L} = \frac{1}{qB} \left( \frac{s}{R} \right) \frac{p}{2} (\cos\theta + \frac{1}{\cos\theta}) \quad (2.3)$$

where  $q$  is the electric charge of particle,  $B$  is the magnetic field,  $s$  and  $R$  are the path length and the radius of curvature of solenoid respectively.  $s/R$  is the bending angle,  $p_L$  and  $p_T$  [ $\text{GeV}/c$ ] are longitudinal and transverse momnetum. To keep the center of the helical trajectories of muons in the bending plane, a compensating dipole field parallel to the drift direction is applied, which is given by

$$B_{comp} = \frac{1}{qR} \frac{p_0}{2} (\cos\theta_0 + \frac{1}{\cos\theta_0}) \quad (2.4)$$

The muon transport solenoid consists of 16 coils without stabilizer and a dipole coil with 0.056 Tesla compensating field is attached on the outer surface of each solenoid. Details of each coil and design parameters are listed in table 2.4 and 2.3.

Item	Value
Conductor	NbTi/Cu wire Cu:NbTi = 6:1
Cable dimensions (solenoid)	$\phi$ 1.5 mm (without insulation) $\phi$ 1.56 mm (with insulation)
Cable dimensions (dipole)	$\phi$ 1.2 mm (without insulation) $\phi$ 1.3 mm (with insulation)
Cable insulation	Polyimide-imide enamel (AIW), PVF (TS2-15, TS3)
Magnet length	$\sim$ 6 m
Curvature radius	3 m
Number of solenoid coils	18
Number of dipole coils	16 pairs
Operation current	210 A (solenoid) 165 A (dipole)
Field on axis	$\sim$ 3 T (solenoid) $\sim$ 0.056 T (dipole)
Stored energy	5.6 MJ
Total inductance	254 H
Refrigeration	conduction from forced flow 2-phase LHe piping (7-10 g/sec)
Quench protection	semi-active quench back heater

Table 2.3: Design parameters of transport solenoid.

Coil	$B_z$ [T]	$B_y$ [T]	Length [mm]	Inner radius [mm]	Outer radius [mm]	Current [A]	Current density [A/mm <sup>2</sup> ]
TS2a	3	NA	255	234	249	210	72
TS2-1	3	0.06	205	234	264	210	95
TS2-2~15	3	0.06	205	234	272	210	95
TS2-16	3	0.06	205	234	254	210	94
TS3	3	NA	600	400	437	190	85.5

Table 2.4: Coils parameters for muon transport solenoid.

## 2.4 Detector solenoid

The detector solenoid consists of 14 DS coils and 5 BS collimator coils with 1 and 1.57 Tesla magnetic field respectively. The superconducting wires of BS and DS have diameter of 1.26 mm with copper ratio of 4.2, and RRR of copper is higher than 60. Superconducting cable is insulated by PVF with 30  $\mu\text{m}$  thick. The stored energy of DS and BS are about 4.45 MJ and 0.166 MJ respectively. Inductance of these two solenoids are 240 H and 13.8 H. The detector solenoid is cooled by GM refrigerators independently.



# Chapter 3

## Radiation estimation

Since the high energy and high intensity proton beam is used in COMET experiment, the radiation is an important issue for superconducting magnet design. In this chapter, the details of prompt and residual radiation will be described. Moreover, one radiation shield is designed for protecting the pion capture solenoid.

### 3.1 Hadronic models

Monte Carlo code is usually used in high energy physics to simulate the physical process. Recently, it is also playing increasingly role in the other studies, like heavy ion therapy<sup>(15)</sup>, nuclear fusion reactor et al. The hadron model in some Monte Carlo codes which is used in the paper is introduced as follows.

#### 3.1.1 PHITS

Particle and Heavy Ion Transport code System (PHITS) is developed by Japan Atomic Energy Agency (JAEA)<sup>(16)</sup>. The PHITS code is written in FORTRAN, and it can deal with the transport of almost all particles over a wide energy range.

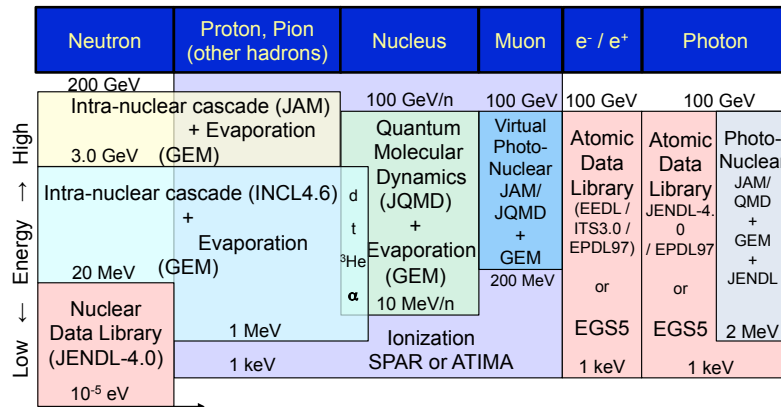


Figure 3.1: The physical model used in PHITS code. Default hadronic model is JAM\_INCL4.6\_JENDL, moreover, JAM\_BERT\_JENDL and JAM\_INC-ELF\_JENDL are able to be selected in PHITS code.

PHITS uses its own models for nuclear collisions and for hadron reactions. The details of physical model

in PHITS are shown in figure 3.1. As for 8 GeV hadron collision, the Japanese nuclear library, JENDL-4.0, is employed in the low energy region ( $\leq 20$  MeV). Between 20 MeV and 3 GeV, there are three kinds of different model in hadron reaction, which are the INCL4.6<sup>(17)</sup>, Bertini and INC-ELF<sup>(18)</sup>.

### 3.1.2 FLUKA

FLUKA is a fully integrated particle physics Monte Carlo simulation package developed by CERN<sup>(19)</sup>. Two hadronic models are included in FLUKA, the Generalized IntraNuclear Cascade (GINC) model in high energy region ( $\geq 5$  GeV) which is treated in the Glauber-Gribov formalism and PEANUT model in the low energy region<sup>(20)</sup>.

### 3.1.3 GEANT4

GEANT4 is the most powerful toolkit for simulation of high energy physics experiment<sup>(21)</sup>. Like PHITS, GEANT4 is using the G4 neutron data library (G4NDL) in the energy less than 20 MeV. Between 20 MeV and 5 GeV, three models, Binary, Bertini and INCL++, can be selected in G4. G4 also provides the FTF String model from the range of 5 GeV to 20 TeV and QG String model to 100 TeV.

## 3.2 Modification of PHITS code

Here, the modification of PHITS code will be introduced to achieve the realistic simulation of COMET experiment. The main optimization of PHITS code is listed as follows.

- Bridged PHITS and the accelerator simulation code TURTLE.
- Enable to read the external field map.
- The charged particle can be bended in user defined field.
- The output file from PHITS can be read into GEANT4 code.
- Enable to use the ROOT toolkit in PHITS.

### 3.2.1 Proton beam

The proton beam source is simulated by the accelerator simulation code, called TURTLE in COMET experiment. The simulation of TURTLE has been already shown in figure 3.2, and one bunch of the proton beam where locates in front of production target is gaussian distribution with size of  $2\text{ cm} \times 0.8\text{ cm}$  and momentum of  $8.9\text{ MeV}/c$ . PHITS can read the external file as the radiation source, but due to the different coordinate used in PHITS and TURTLE. One script has been written to convert the coordinate and pretend the PHITS dump file to be read. The proton beam used in radiation estimation is TURTLE data for phase-I and gaussian beam for phase-II, respectively.

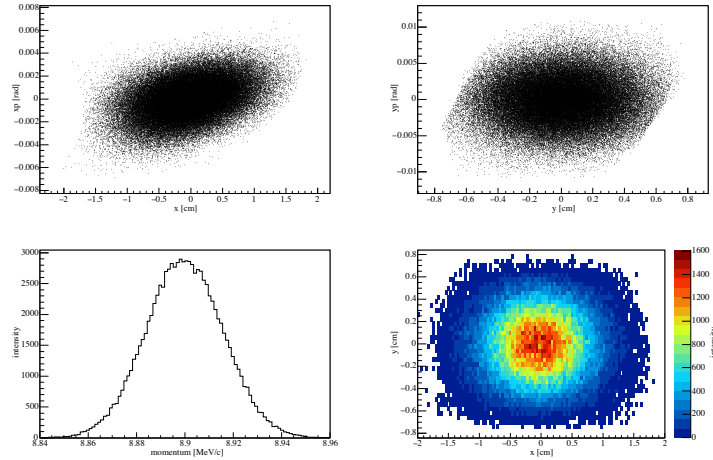


Figure 3.2: Proton beam distribution simulated by TURTLE code. Top two are the momentum distribution of x and y axis, respectively. Bottom two are the momentum distribution and spatial distribution. Here, intensity means the normalized intensity.

### 3.2.2 Magnetic field

As for nowadays' PHITS, it still cannot bend the charged particles in user's field map. However, the radiation estimation is affected by the magnetic field sensitively. To solve this issue, one magnetic field interpolation subroutine written by C is compiled with FORTRAN files. The details of the magnetic field interpolation is described in appendix A. The charged particles are bended with a circular path in the magnetic field which is written as

$$R = \frac{p}{eB} = \frac{m\gamma\beta c}{eB} = p \cdot \frac{3.336}{B} \quad (3.1)$$

To ensure the magnetic field interpolation, the uniform field map with 5 Tesla has been tested and the tracking is shown in 3.3. Following the equation 3.1, the bending radius of 0.1 GeV/c momentum electron in 5 Tesla is 6.6 cm. The radius from the simulation is totally agree with the calculation.

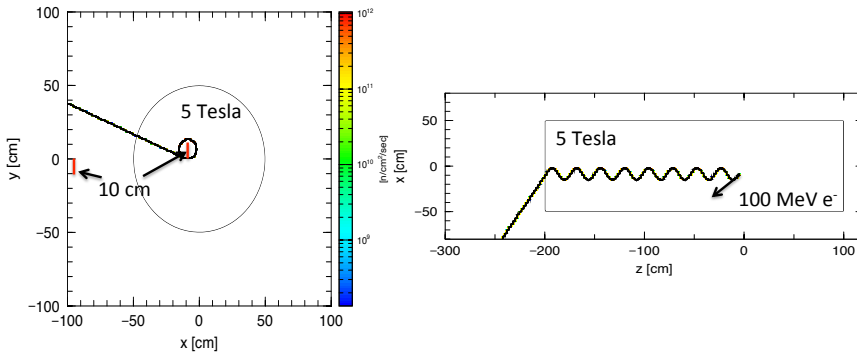


Figure 3.3: Tracking of 100 MeV electron with uniform 5 Tesla field. One electron is injected with angle of 30 degree. Magnetic field is applied in a cylinder with radius of 50 cm and length of 300 cm.

The field map included into COMET PHITS simulation is calculated by Finite Element Method (FEM) with iron yoke, which is shown in figure 3.4. There are still some missing part of field map, like the field around the iron yoke and proton beam transport pipe. It will affect the proton beam transportation definitely,

but this map is enough for the radiation study.

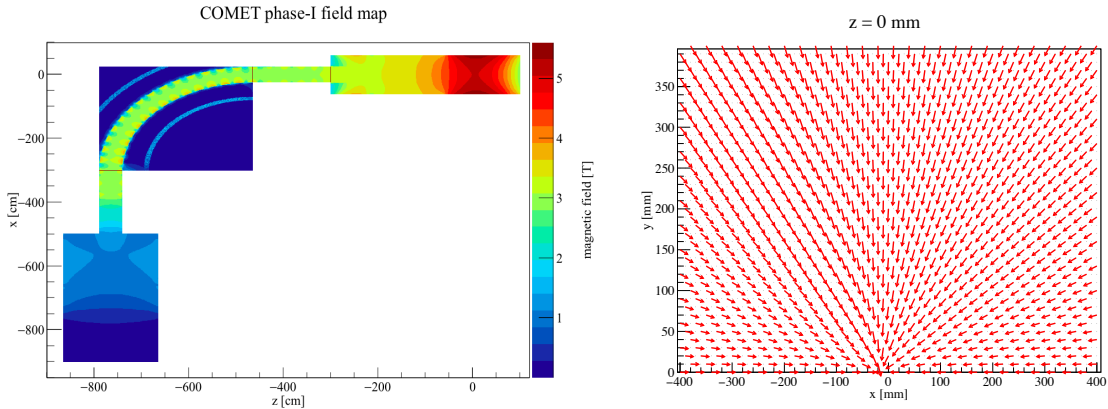


Figure 3.4: Magnetic field map of phase-I experiment used in PHITS simulation. It is calculated by FEM with iron yoke. Mangetic field vector at  $z = 0$  cm is shown on the right.

### 3.3 Prompt radiation

#### 3.3.1 Physical model comparison

Since PHITS does not include a lot of physics model involved muon such as muon decay on the orbits, specific X-ray of muon capture, rate decay of muon et al., on the other hand, GEANT4 physics model is almost implement compared to PHITS, the comparison of particle yield between GEANT4 and PHITS is necessary to make sure the missing physics model can be neglected in radiation estimation.

The comparison is taken by using a very simple geometry, which is only one graphite target with 60 cm length and 2 cm radius. Incident proton beam is 8 GeV with gaussian distribution. Magnetic field is included in the region around target with 30 cm radius and 140 cm length. As the result shown in figure 3.5 and table 3.1, the integral yield of pion and muon from target predicted by PHITS is higher than GENAT4's with factor 12.9%. For the neutron, the production yield has 17% difference between GEANT4 and PHITS.

	$\mu^-$ [n/proton]	$\pi^-$ [n/proton]	$\mu^+$ [n/proton]	$\pi^+$ [n/proton]	neutron [n/proton]
GEANT4	0.033	0.613	0.053	0.786	2.891
PHITS	0.034	0.723	0.044	0.876	3.464
$\sigma$	-3%	-15%	21%	-10%	-17%

Table 3.1: Comparison of PHITS with GEANT4.  $\sigma$  represents  $(G4-PHITS)/PHITS$ .

The backward production of muon and pion at high energy region is difficult to predict because of the lack of experimental data. Especially for the COMET experiment which is employed the backward muon, prediction of backward muon and pion is quite different from the different physics model. Thus, as the comparison of backward pion and muon at 1 m far from the target, compared with JAM\_BERT\_JENDL, the pion energy spectrum predicted by QGSP\_BERT\_G4NDL has high energy tail and lower peak. Because the pion only comes from the high energy cascade model, the different must be between JAM and QGSP.

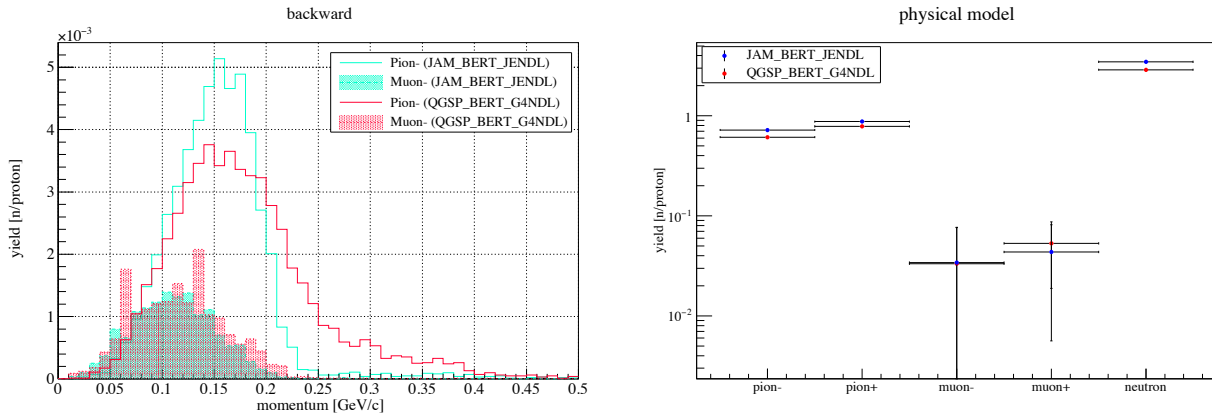


Figure 3.5: Compared the backward particle yield and integral yield with GEANT4 and PHITS. Left one is the backward pion and muon yield, red and blue line represent the yield calculated by QGSP\_BERT\_G4NDL and JAM\_BERT\_JENDL respectively. Right one shows the integral yield of pion and muon from target, red and blue point are the result of QGSP\_BERT\_G4NDL and JAM\_BERT\_JENDL.

### 3.3.2 Geometry

The geometry plays an important role in radiation simulation, especially for the high energy physics. Every detail of COMET phase-I geometry is established in PHITS simulation in terms of the design drawing from KEK.

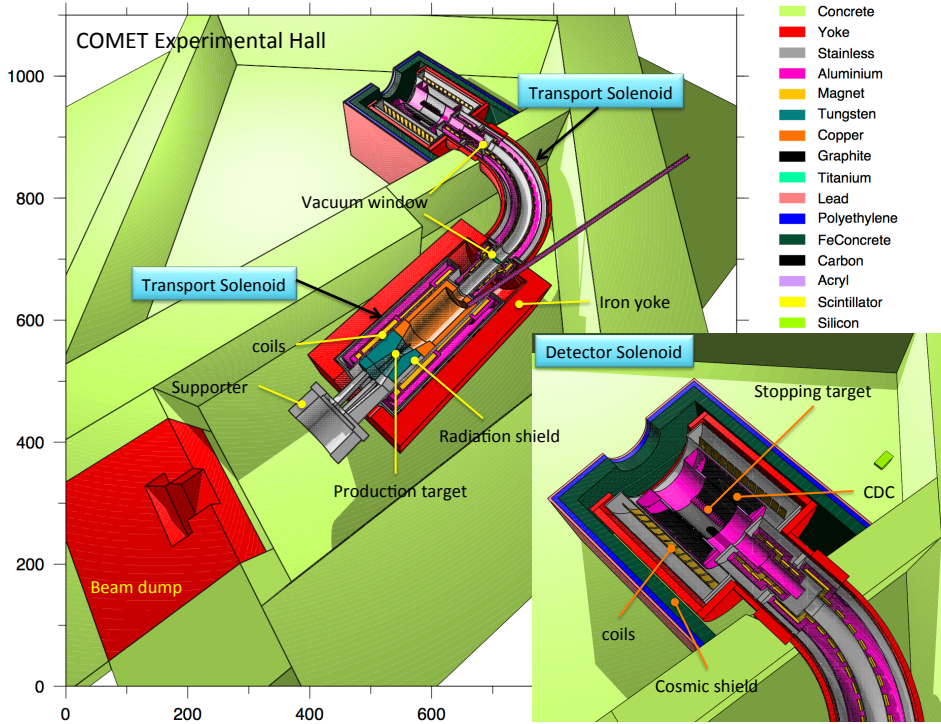


Figure 3.6: COMET phase-I experiment geometry in PHITS simulation.

As shown in figure 3.6, the COMET experimental hall is separated by concrete wall with 1 m thickness at end of 90 degree bending and 2 m at beam dump. The concrete wall between experimental hall and control room and accelerator hall is with 3 m thickness to prevent the radiation leaking. Beam dump consists of iron yoke with  $1.5 \times 1.5 \times 1$  m and  $2.5 \times 2.5 \times 1$  m holes which is same to the Mu2e beam absorber design

and concrete (22). Ceiling board is made of iron yoke with thickness of 0.6 m, gas (air) with thickness of 0.7 m and concrete with 3.7 m thickness. Shielding supporter structure is made of stainless steel (SUS-304) with two holes for proton beam exit and target changing. Radiation shield is employed the composit shield which will be described later. In the muon beamline, two 1 mm titanium vacuum windows are set up in the end of pion capture solenoid and muon transport solenoid respectively. Cosmic shield is consist of 20 cm concrete with 50% iron, 10 cm polyethylene and 10 cm lead.

### 3.3.3 Radiation estimation

Since only backward pion is employed to create muon in high magnetic field, the main radiation is neutron and photon because they are not affected with magnetic field. As implemented the geometry and magnetic field, the neutron and photon distribution is calculated and shown in figure 3.8. Because the geometry is only for phase-I experiment, the production target is replaced from graphite to pure tungsten target, and the proton beam intensity is changed to  $4.4 \times 10^{13}$  pps to estimate the radiation for phase-II experiment.

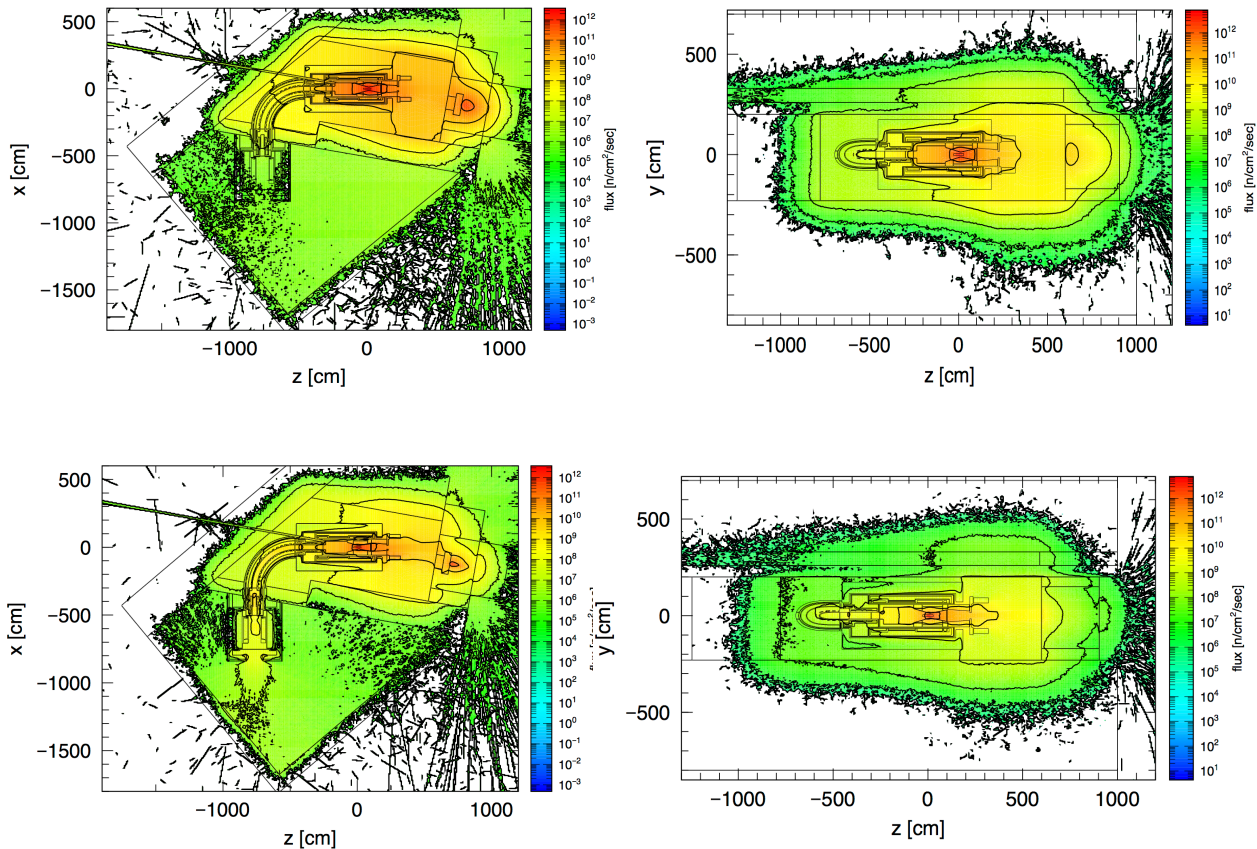


Figure 3.8: Neutron and photon distribution for COMET phase-II experiment. Top two show the neutron distribution from x-z and y-z view. Bottom two are the distribution of photon from x-z and y-z view.

Furthermore, to prevent neutrons leak to the detector room, the concrete wall with 2 m thick is replaced by iron yoke. Even if the iron yoke is employed as a wall here, it still has  $5 \times 10^6 \text{ n/cm}^2/\text{sec}$  neutrons at least which leak from experimental room to detector room which is 5 times higher than phase-I exipертment. The neutron along the muon beamline is with low energy and it is easy to be capture or scattered in the detector solenoid. While, as for the photon, it comes from the neutron capture, muon capture, bremsstrahlung et al.

Thus, the photon in the detector solenoid is about  $10^9$  n/cm<sup>2</sup>/sec at peak, which is 100 times higher than phase-I experiment at same place.

Figure 3.9 shows the energy spectrum of muon, photon and neutron for phase-II experiment at the end of 90 degree bending. Compared with the other particle, neutron and photon is most dominated particle along the beamline. Almost neutron is in the range of low energy, and photon is with energy from 0.01 MeV to 100 MeV.

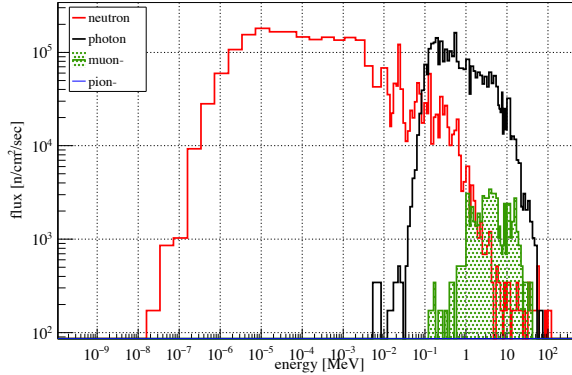


Figure 3.9: Energy spectrum of muon, photon and neutron from both experimental hall and beamline at the end of 90 degree bending. Most of neutrons are at the low energy region, and photon are all higher than 10 keV.

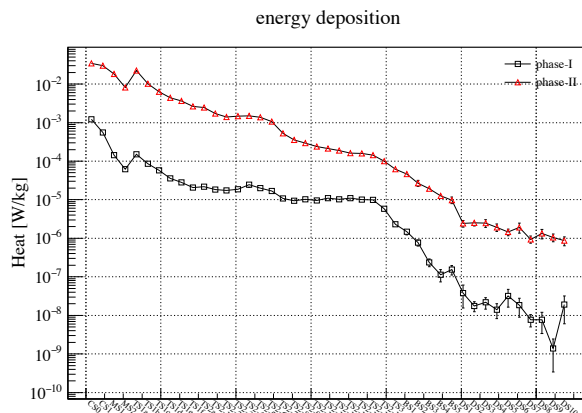


Figure 3.10: The energy deposition of each magnets in phase-I and phase-II experiment. Black and red point represent the energy deposition of phase-I and phase-II experiment respectively. The energy deposition of phase-II is one order higher than phase-I's, and its peak is located in CS0 coil.

The radiation remains their energy into superconducting coils, which will cause the hot spot inside the magnets. Once the hot spot is generated in the superconducting magnet, these magnets are at risk from quench. The heat load of each magnet for phase-I and phase-II experiment are shown in figure 3.10. Compared with phase-I experiment, heat load of phase-II experiment is 10 times higher than phase-I experiment at least. The peak of heat load is at CS0 coil which 0.03 W/kg corresponding to 0.73 MGy for 280-day operation.

## 3.4 Residual radiation estimation

To achieve the muon with higher intensity, the graphite target will be replaced by pure tungsten target after phase-I experiment finished. Thus, the residual radiation plays an important role in target changing and maintenance of the superconducting magnets. The residual radiation has been investigated by using FLUKA code and PHITS code.

### 3.4.1 Residual radiation

The residual radiation of each part of solenoid is estimated by PHITS and DCHAIN-SP code (23). DCHAIN-SP code is a dedicated software for the residual radiation developed by JAEA. Using the result of nucleus yield from PHITS code, the photon flux and its intensity is able to be calculated by DCHAIN-SP. Then, the distribution of residual radiation is estimated by

$$E(\epsilon) = f(\epsilon) \cdot \phi(\epsilon) \quad (3.2)$$

where  $E(\epsilon)$  and  $\phi(\epsilon)$  are the effective dose and the gamma ray flux calculated in DCHAIN-SP. The fluence-to-effective dose conversion coefficients  $f(\epsilon)$  is shown in reference (24) with unit of  $\text{Sv}/\text{cm}^2$ .

The operation time schedule used in calculation are 1-year cooling after 1-month running with intensity of  $2.5 \times 10^{12}$  pps, which are all base on the phase-I experiment. Residual radiation of vacuum vessel, magnet, radiation shield and iron yoke are given by figure 3.11. To reduce the residual radiation as much as possible, considering copper is hard to weld with stainless steel, some parts of vacuum vessel is able to be changed to iron. As listed in table 3.2, residual radiation of stainless steel is 10 times higher than iron's. Thus, the stainless steel is replaced by iron for vacuum vessel outside the superconducting magnet due to magnetism of iron.

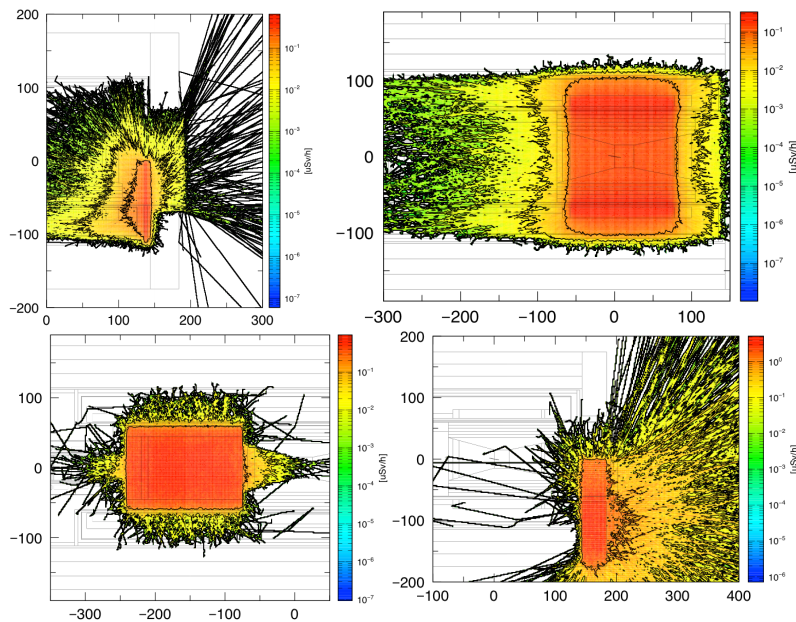


Figure 3.11: Residual radiation of vacuum vessel, magnet, radiation shield and iron yoke with 1 month operation and 10 month cooling.

	Stainless steel	Iron
Radiation dose [ $\mu\text{Sv}/\text{h}$ ]	7.00	0.65

Table 3.2: Residual radiation of vacuum vessel between CS0 and iron yoke.

The residual radiation of superconducting magnet is calculated as one conductor which consists of aluminum, copper and NbTi with density of  $4.0 \text{ g/cm}^3$ . The activity and radiation dose given by figure 3.12 shows that the maximum radiation dose is  $0.33 \mu\text{Sv}/\text{h}$  after 1 month operation and 10 month cooling for phase-I experiment and the peak of activation is at CS0 and CS1. Isotopes like  $^{93}\text{Nb}$ ,  $^{22}\text{Na}$ ,  $^3\text{H}$ ,  $^{60}\text{Co}$  et al. with long half life are generated in CS1 and CS0 coils.

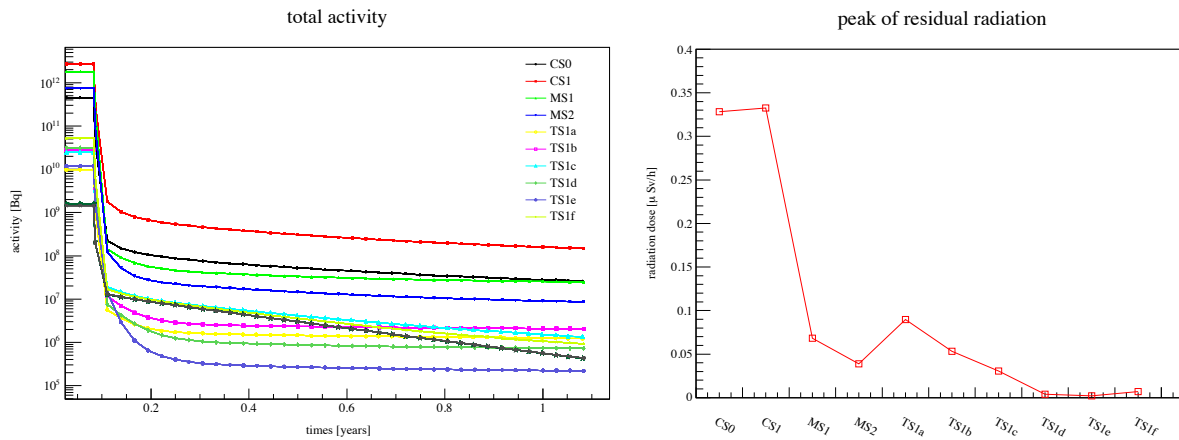


Figure 3.12: Activity and peak of dose equivalent of each magnets with 1-month operation and 10-month cooling.

Because PHITS and DCHAIN-SP only can calculate the residual radiation from a defined region, it may cause the average of the radiation if the geometry is cut to many tiny meshes. Figure 3.13 (left) shows the total dose equivalent predicted by PHITS and DCHAIN-SP. It is added from many parts of small regions. The maximum dose equivalent is predicted to  $0.75 \text{ mSv}/\text{h}$  for 1-month operation and 10-month cooling at production target. To ensure the dose equivalent, we also compare this result with FLUKA code which can simulate the residual radiation dose without region cutting. M. Brugger et al. present the residual radiation calculated from FLUKA code has good agreement experimental data<sup>(25)</sup>.

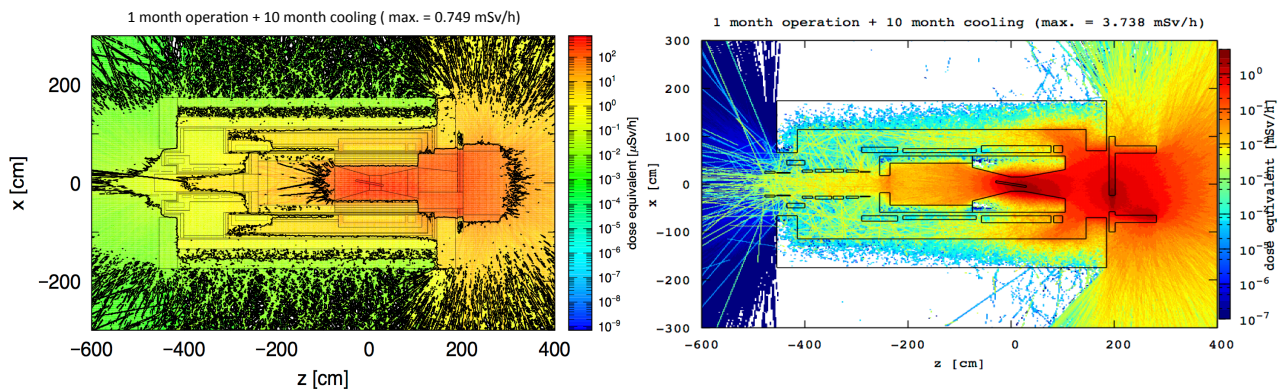


Figure 3.13: Compared the residual radiation distribution of pion capture solenoid between PHITS and FLUKA. Left and right represent the PHITS and FLUKA result respectively.

As the result shown in figure 3.13 (right), the maximum dose equivalent is predicted to 3.74 mSv/h with same time schedule, which is 5 times higher than PHITS result. In figure 3.3, the dose equivalent at different position along the axis is compared. Besides the place where peak is, the dose equivalent is quite similar between the FLUKA and PHITS. Difference may be owing to the mesh cutting of PHITS calculation around target.

Code	$z = 0$ [mSv/h]	$z = 300$ [mSv/h]	$z = -300$ [mSv/h]	$z = -500$ [mSv/h]
FLUKA	3.74	0.04	0.009	0.002
PHITS	0.75	0.03	0.01	0.002

Table 3.3: Compared the residual radiation along the z axis.  $z=0$  is at the production target,  $z=-300$  is 3 m far from the target on upstream of target,  $z=300$  is 3 m far from the target on downstream of target, and  $z=-500$  is 5 m far from the target.

Because of the target changing after phase-I experiment, this residual radiation is still too high for co-workers. Table 3.4 gives the maximum residual radiation after cooling for 10 months, 1.75 year and 2 years.

Time [year]	Maximum residual radiation [mSv/h]
0.83	3.738
1.75	1.125
2.00	1.013

Table 3.4: Maximum residual radiation after cooling for 10 months, 1.75 year and 2 years.

From this estimation, the residual radiation will be reduced about 3 times after cooling for 2 years compared with 10 month cooling. Considering the beam dump is not included into this simulation, working for 1 hour is possible for co-workers.

## 3.5 Radiation shielding optimization

The heat and radiation shield (HRS) is located around the production target to protect the superconducting from the radiation exposure. This radiation shield consists of two parts, one is for protecting MS magnets, another one is for protecting CS magnets. It is unable to take long time to change the radiation shield after phase-I experiment due to the residual radiation. Thus, radiation shield must be designed for both phase-I and phase-II experiment.

Pure tungsten is most ideal material as the radiation shield due to its high density. However, it has several disadvantages such as high costs, heavy mass and complex fabrication. Therefore, some parts of radiation shield can be replaced by the other materials.

### 3.5.1 Radiation shield for MS

Inside the superconducting magnets, radiation shield must be made of material without magnetism. Thus, there are two candidates for MS radiation shield, copper and stainless steel. The heat load of each

CS and MS magnet when the copper and stainless steel is used as radiation is estimated by PHITS code in table 3.5. It shows that copper shield has better shielding ability than stainless steel shield.

	CS0 [W]	CS1 [W]	MS1 [W]	MS2 [W]	CS + MS [W]
SUS304	8.03	51.82	27.80	10.49	98.13
Copper	7.56	50.14	22.99	8.73	89.42

Table 3.5: Heat load of stainless steel and copper shield.

Considering the residual radiation of radiation shield, the activated isotopes and activity after 1-month operation and 10-month cooling are investigated and shown in table 3.6. Apparently, copper shield's activity is quite lower than stainless steel shield's. Furthermore, the dose equivalent of copper and stainless steel shield are  $1.51 \mu\text{Sv/h}$  and  $7.02 \mu\text{Sv/h}$  respectively.

From the aspect of shielding ability and residual radiation, copper is the better material for MS radiation shield. Noting that the induced current will be generated by the changing of magnetic field, the copper should be cut in somewhere.

Nuclei	Activity [MBq]	Half life [year]	Nuclei	Activity [MBq]	Half life [year]
$^{60}\text{Co}$	192	5.27	$^{55}\text{Fe}$	4950	2.73
$^{57}\text{Co}$	111	0.75	$^{54}\text{Mn}$	1500	0.86
$^{63}\text{Ni}$	80.9	100	$^{49}\text{V}$	878	0.90
$^{58}\text{Co}$	56.9	0.19	$^{57}\text{Co}$	585	0.75
$^{54}\text{Mn}$	54.7	0.86	$^{58}\text{Co}$	387	0.19
$^3\text{H}$	30.9	12.3	$^{51}\text{Cr}$	92.6	0.08
$^{55}\text{Fe}$	29.3	2.73	$^{59}\text{Fe}$	29.4	0.12
$^{49}\text{V}$	16.7	0.90	$^{63}\text{Ni}$	26.5	100
$^{56}\text{Co}$	5.52	0.21	$^3\text{H}$	26.0	12.3
$^{65}\text{Zn}$	5.13	0.67	$^{60}\text{Co}$	21.7	5.27

Table 3.6: Activated isotopes of copper (left) and stainless steel (right).

### 3.5.2 Radiation shield for CS

Proton is injected into pion capture solenoid with 10 degree, thus, a hot spot is created on the one side of CS1 and CS0 coils, which is the one of the reason why quench occurs. Thus, the radiation shield for CS requires

- Limit the maximum heat load in coils.
- Limit the maximum radiation induced damage in coils.
- Reduce the mass of radiation shield.
- Pion yield should not be reduced significantly.

To eliminate the hot spot and keep the balance, the low radiation region which corresponds to the side far to incident proton enables to be fabricated by another kind of material. As for the material, the ideal material is pure tungsten but only the tungsten alloy is cheaper and easy to fabricate. Thus, the details of tungsten alloy (AN-1800) are listed in table 3.7.

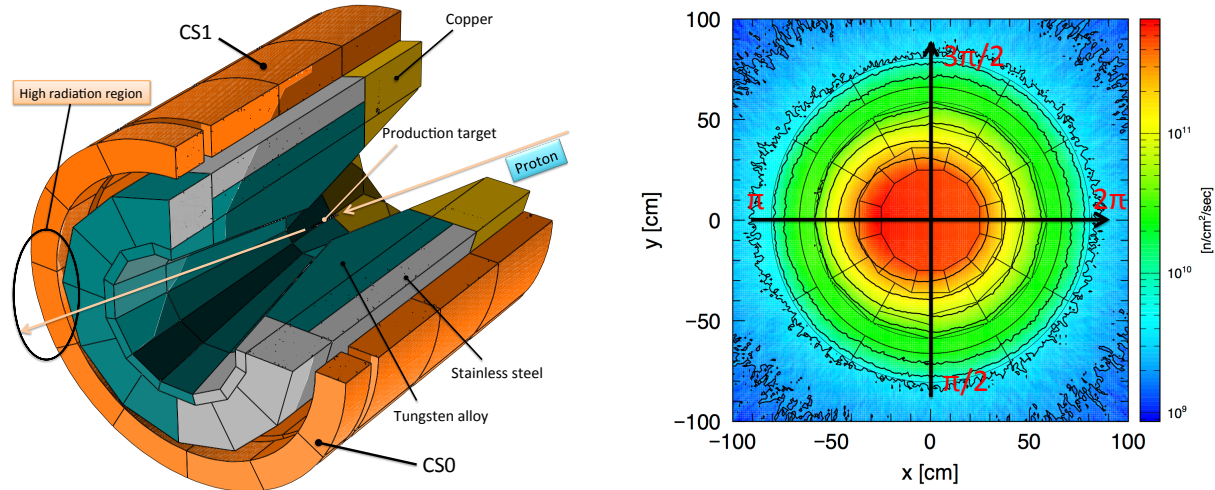


Figure 3.14: The concept of COMET radiation shield. It consists of tungsten alloy, stainless steel and copper. Tungsten alloy and stainless steel are employed on the high and low radiation side respectively. On the downstream of target, copper is used. Right figure shows the distribution of neutron from x-y view. Azimuthal angle is also defined in here. The peak of neutron flux is located at 180 degree of CS coils.

Composition [wt.%]	Ni: $3.0 \pm 0.25$ ; Cu: $2.0 \pm 0.25$ ; W: $95.0 \pm 0.5$
Density [g/cm³]	$18.0 \pm 0.2$
Hardness	$HV 320 \pm 50$
Tensile strength	620 MPa
Offset yield strength	500 MPa
Elastic modulus	310 GPa
Thermal conductivity	104 W/m/K
Thermal expansion coefficient	$5.5 \times 10^{-6} \text{ K}^{-1}$

Table 3.7: Material property of tungsten alloy (AN-1800).

As shown in figure 3.14, the radiation shield is designed which consists of tungsten alloy, copper and stainless steel. The DPA, neutron fluence and heat load of several shielding design concepts along azimuthal direction is compared in figure 3.15 and 3.16. Details of several shielding designs are listed as follows.

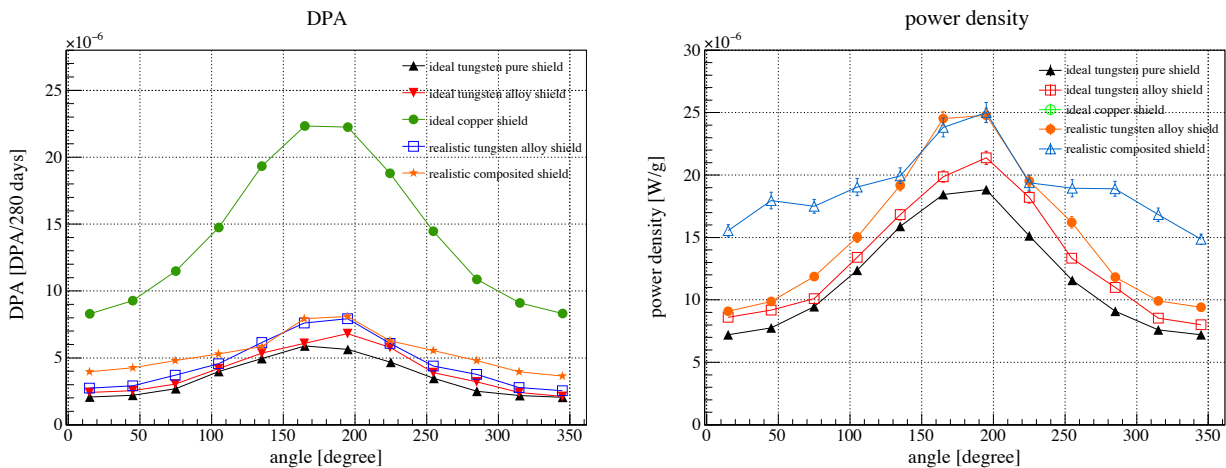


Figure 3.15: Compared the azimuthal DPA and energy deposition of middel part of CS1 coil in different verion of shielding design. The long CS1 coil is cut to 3 parts along the z axis and 12 parts along the azimuthal axis.

- Ideal pure tungsten shield: made of pure tungsten with a cylindrical shape.
- Ideal tungsten alloy shield: made of tungsten alloy with a cylindrical shape.
- Ideal copper shield: made of copper with a cylindrical shape.
- Realistic tungsten alloy shield: made of tungsten alloy with a polygonal shape.
- Realistic composites shield: made of tungsten alloy, copper and stainless steel with a polygonal shape.

After these comparisons, we come out the conclusion

- The maximum DPA of CS1 coils increases over 4 times when the pure tungsten is replaced by copper.
- Compared with tungsten alloy, pure tungsten has stronger shielding ability.
- Shielding ability of cylindrical shape is stronger than polygonal shape.
- The peak of DPA, heat load and neutron fluence is same between composites shield and tungsten alloy shield.

The details of shielding design is listed in table 3.8.

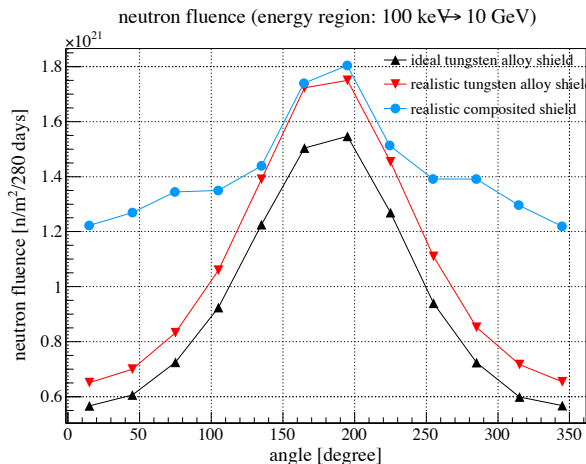


Figure 3.16: High energy neutron ( $E \geq 0.1$  MeV) along the azimuthal direction of CS1 coils.

CS1	Composites shield	Pure tungsten shield
peak neutron fluence [ $n/m^2/280$ days]	$2.35 \times 10^{21}$	$2.26 \times 10^{21}$
peak power density [W/g]	$2.50 \times 10^{-5}$	$2.40 \times 10^{-5}$
power [W]	57.5	36.6
peak dose [MGy/280 days]	0.79	0.76
peak DPA [DPA/280 days]	$1.05 \times 10^{-5}$	$0.98 \times 10^{-5}$
tungsten mass [t]	15.6	28

Table 3.8: Details of the shielding design. CS1 is cut to 3 parts along the z axis, 12 parts along the azimuthal direction.

As for the muon yield, it does not depend on the material of radiation but the backward radius of shield. Figure 3.17 shows that the muon and pion yield increases about 9% after the radius is changed from 36 cm to 50 cm.

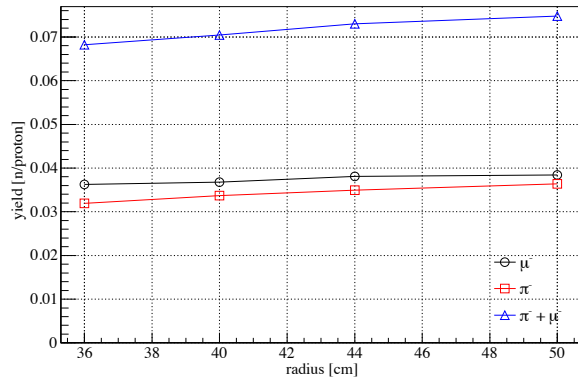


Figure 3.17: A relation of muon and pion yield with shielding backward radius. Current shielding backward radius is 36 cm. Black line:  $\mu^-$ , red line:  $\pi^-$ , blue line:  $\mu^- + \pi^-$ .

# Chapter 4

## Irradiation test for superconducting magnet material

Since the superconducting solenoid of COMET experiment is exposed under the high radiation environment, the superconducting solenoid has a risk of quench due to the radiation damage in the some part of solenoid. Thus, the study of radiation damage on the material used in COMET superconducting magnet system is quite significant. In this chapter, the irradiation test on GFRPs, Quench protection diode and pure aluminum will be introduced.

### 4.1 Glass Fiber Reinforced Plastic

Glass Fiber Reinforced Plastics (GFRP) are widely used in many engineering applications because of their superior properties such as higher specific strength, specific modulus, anti-corrosion and thermal insulation<sup>(26)</sup>. In the case of COMET experiment, GFRPs are employed as the insulation spacer for superconducting magnets which suffer high magnetic field and radiation. Due to the worse radiation resistance for the Glass-Epoxy (G10), 3 kinds of GFRPs what impregnate the Bismaleimide-Triazine (BT), Bismaleimide (BMI) and Cyanate Ester (CE) in the S-2 glass fiber have been developed to enhance the radiation resistance and mechanical properties. Here Boron is excluded from the S-2 glass in order to reduce the influence from neutron.

#### 4.1.1 Experiment

Each sample of GFRPs (G10, CE, BT and BMI) is prepared as Japanese Industrial Standards (JIS), which is with 100 mm long, 10 mm wide and 0.5 mm thick. The irradiation test of GFRPs is taken in the Takasaki Advanced Radiation Research Institute by using 1 MeV uniform electron beam and Research Reactor Institute, Kyoto University (KUR) by using 34 MeV accelerator electron beam. After irradiation, the tensile strength of irradiated samples is measured as well. Figure 4.1 shows how GFRP samples break after irradiation.

For the 1 MeV electron irradiation test, radiation dose is measured by cellulose triacetate (CTA) tape<sup>(27)</sup>

and it can be estimated from the equation as follows.

$$\text{dose} = \frac{D_e - D_0}{K} \cdot \frac{0.125}{t} \cdot f \quad (4.1)$$

where the unit of dose is kGy.  $D_e$  and  $D_0$  is the light absorption before and after irradiation.  $K$  is the constant for irradiation which is defined to 0.0063 for electron and 0.0081 for photon.  $t$  and  $f$  are the thickness of CTA tape and correction term, respectively. Average radiation dose is about 0.8 kGy/sec·mA in terms of this equation. Each sample of G10, CE, BT and BMI is irradiation with 50, 100 and 200 MGy totally. As the results shown in figure 4.2 (left), BT and BMI are definitely stronger than G10 and CE without irradiation. The tensile strength of G10 and CE drops to about 150 MPa after 200 MGy irradiation. Similarly, BMI also has a tendency to degrade. While the BT, the tensile strength has no big change after 200 MGy irradiation.



Figure 4.1: GFRP samples before the irradiation are shown on the left. The samples are tensioned until break after irradiation (right).

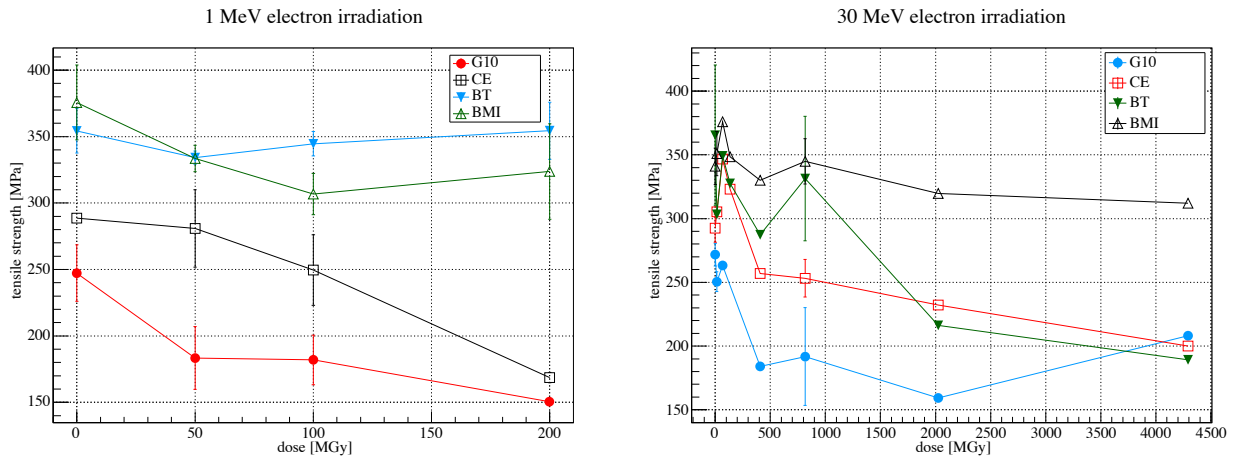


Figure 4.2: The tensile strength of irradiated samples (G10, CE, BMI and BT) when it breaks. Left and Right figure represent 1 MeV electron irradiation test in JAEA, Takasaki and 30 MeV electron irradiation test in LINAC, KURRI.

To investigate the reaction of high energy electron on GFRPs, irradiation with 34 MeV electron has been tested by using accelerator. Because of the electron with high energy, not only the electron but also the photon from Bremsstrahlung and neutron from the photonuclear reaction interact on GFRPs. LINAC

accelerator at KUR provides a gaussian beam with the width of 30 mm. GFRP sample is cooled by water during the irradiation (30°C). Unlike to the 1 MeV irradiation, CTA tape is unable to be used to measure the radiation dose because its energy is out of the range of the measurement ability of CTA tape. Thus, in this case, radiation dose is estimated by PHITS code, which is 1.25 kGy/sec·mA. Each sample is irradiated with 9, 30, 45, 90, 270, 540, 1340 and 2840 MGy totally. In figure 4.2, all samples start to degrade from 90 MGy and they drop to around 200 MPa besides BMI. The flexural strength test and outgassing test for GFRPs are described in reference <sup>(28)</sup>. Considering the mechanical property, outgassing and radiation resistance, BT will be employed as insulation spacer in COMET superconducting magnets.

## 4.2 Quench protection diode

Quench protection diode is a switch of the dump resistor. When magnets quench, the power supply will be cut off, then this diode will be turned on and current will flow toward the dump resistor. The operating voltage will increase after irradiation <sup>(29)</sup>, which causes the over heat of quench protection diode. Moreover different manufacturer fabricates diode with different electrical property. Here, a dedicated quench protection diode for COMET superconducting magnet has been irradiated by high energy neutron. Its electrical characteristics under low temperature and radiation is investigated.

### 4.2.1 Experiment

The irradiation test for quench protection diode is taken with COMET detector group together at the Tendem accelerator, Kyushu university. The fast neutron is produced from carbon target with incident 9 MeV deuteron, which creates neutron by deuteron-deuteron reaction. 5 kinds of samples are set up in front of the production target with the distance of 3 cm as the sequence of MPPC, APD, Artix-7, ROESTI and diode, which is shown in figure 4.3.

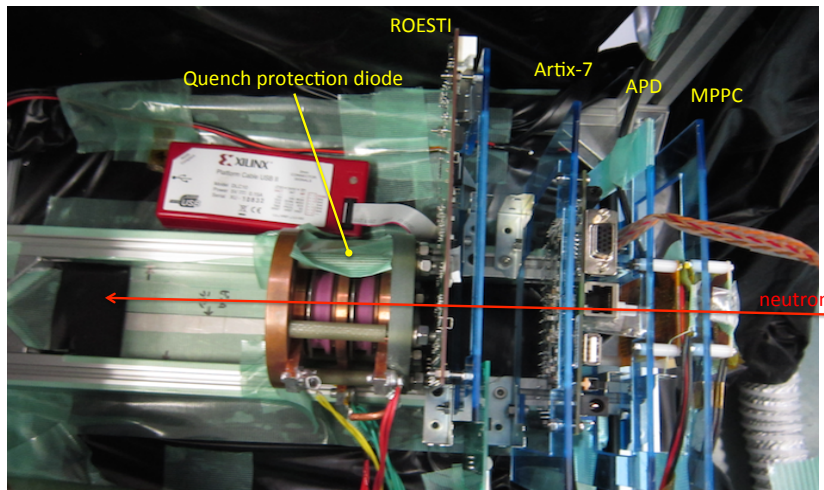


Figure 4.3: Sample setup for neutron irradiation test. Diode is set up in front of MPPC, APD, Artix-7 and ROESTI where is 30 cm far from the neutron production target.

Because diode is with the radius of 3 cm and length of 10 cm, which is possible to stop the neutron, it is located at last of samples where 30 cm far from the production target. Its turn-on voltage is measured during

the irradiation with 5 A power supply, and neutron flux is measured by activation analysis with aluminum, nickel and gold wire (0.07% Fe). Temperature of diode during the irradiation is recorded by thermometer.

### 4.2.2 Neutron measurement

Activation analysis is a common and easy way of neutron measurement, but with the bad energy resolution. Aluminum, nickel and gold wire (0.07% Fe) are employed and stuck on the surface of each sample. The photon from neutron reaction on each activation sample which is list in table 4.1 is measured by HPGe detector.

Element	Reaction	Threshold energy	Half life	Emitted radiation energy [MeV]
Aluminum	$^{27}\text{Al}(\text{n}, \text{p})^{27}\text{Mg}$	1.9 MeV	9.46 min	$\beta^-$ (1.75), $\gamma$ (0.84, 1.013)
Aluminum	$^{27}\text{Al}(\text{n}, \alpha)^{24}\text{Na}$	3.27 MeV	15 h	$\beta^-$ (1.389), $\gamma$ (1.369, 2.754)
Gold	$^{197}\text{Au}(\text{n}, \gamma)^{198}\text{Au}$	(-)	2.7 d	$\beta^-$ (0.962), $\gamma$ (0.412)
Gold	$^{197}\text{Au}(\text{n}, 2\text{n})^{196}\text{Au}$	7.36 MeV	6.18 d	$\beta^-$ , $\gamma$ (0.356)
Nickel	$^{58}\text{Ni}(\text{n}, 2\text{n})^{57}\text{Ni}$	12.09 MeV	36 h	$\beta^+$ , $\gamma$ (0.511, 1.37)

Table 4.1: Neutron activation reactions.

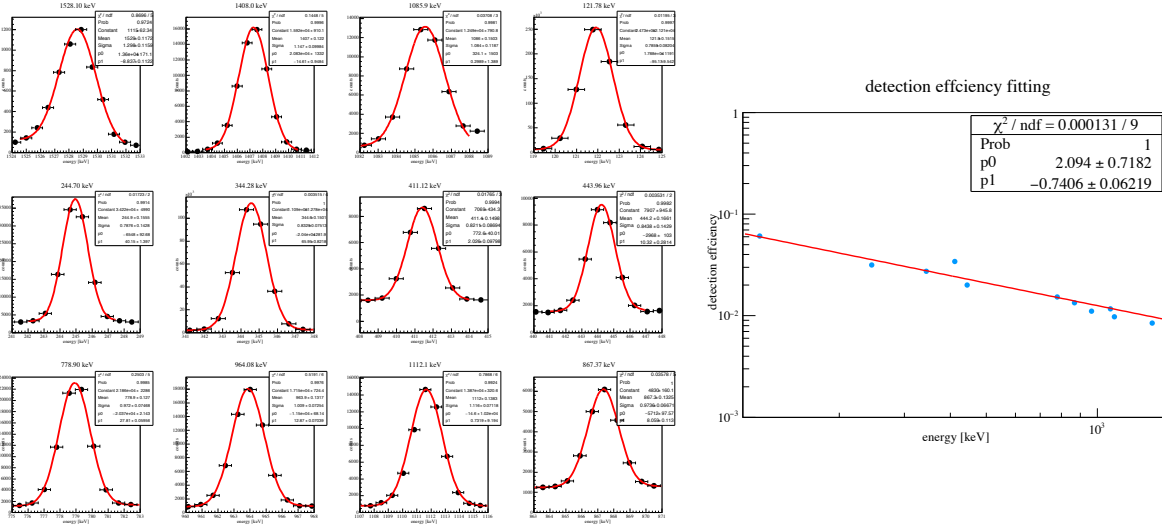


Figure 4.4: The detection efficiency is calibrated by using  $^{152}\text{Eu}$  radiation source. Several peak of  $^{152}\text{Eu}$  is fitted as convolution on left, and the detection efficiency of HPGe is fitted on right.

$^{152}\text{Eu}$  with  $2.79 \times 10^7$  Bq is employed as the calibration source to estimate the detection efficiency of HPGe detector. As shown in figure 4.4, each peak of radiation source  $^{152}\text{Eu}$  is fitted as gaussian and linear function. The detection efficiency is fitted as

$$\epsilon = a \cdot E^b \quad (4.2)$$

where the counts for the calculation of detection efficiency  $\epsilon$  is within  $1.78\sigma$ .

a	b
$2.094 \pm 0.7182$	$-0.7406 \pm 0.06219$

Table 4.2: Fitting parameters for detection efficiency.

Neutron flux measured by each activation sample is given by <sup>(30)</sup>

$$\phi = \frac{C \cdot A \cdot \lambda}{\sigma \cdot N_A \cdot \gamma \cdot m \cdot I \cdot \epsilon \cdot (1 - e^{-\lambda t_0}) \cdot (e^{-\lambda t_1} - e^{-\lambda t_2})} \quad (4.3)$$

where  $C$  is the number of counts under the peak of each activation sample.  $\sigma$  and  $\gamma$  are the cross section of a reaction which is picked up from JENDL data library and probability that a photon is emitted per decay of the isotope respectively.  $N_A$  is the Avogadro constant, and  $I$  is a weight fraction of isotope with atomic mass  $A$ .  $m$  is the mass of activation sample.  $\epsilon$  and  $t_2 - t_1$  are the detection efficiency and counting time.

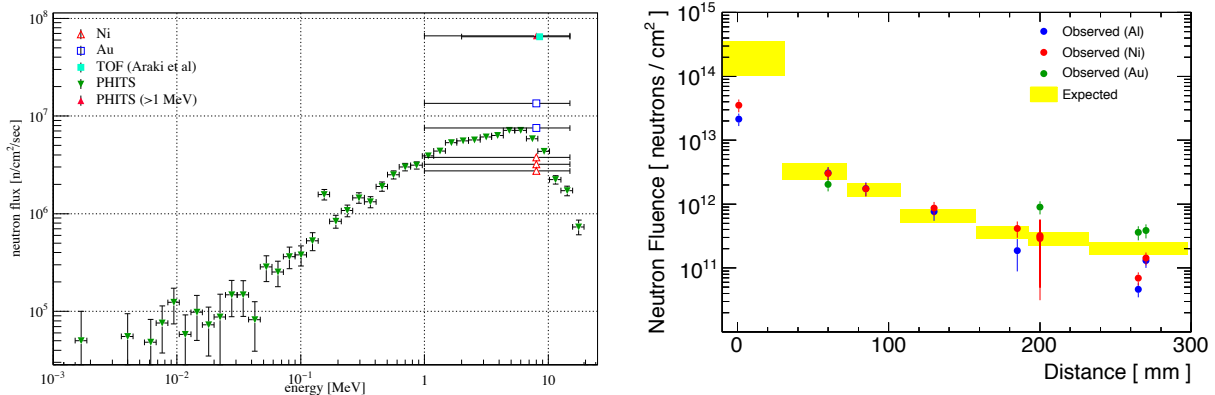


Figure 4.5: Neutron flux is measured by Au wire, Al and Ni foils. The comparison of experimental data with simulation (left). The neutron flux on the place where samples are set up is shown on right.

As shown in figure 4.5, neutron flux on diode measured by gold wire is higher than nickel's, which is  $1.35 \times 10^7$  n/cm<sup>2</sup>/sec. From the prediction of PHITS code and previous measurement with liquid scintillator, the neutron flux is  $6 \times 10^7$  n/cm<sup>2</sup>/sec which is about 5 times higher than the measurement of gold wire. It is possible that a part of neutron is stopped at flange or the other irradiation sample and causes the difference between measurement and prediction. Thus, in this case, we trust the measurement and the total neutron fluence irradiated until the end of experiment is estimated for  $10^{12}$  n/cm<sup>2</sup>/sec.

### 4.2.3 Electrical property of diode

To investigate the electrical properties of diode, the turn-on voltage is measured during the irradiation, then the voltage on the operating current is predicted by fitting the V-I curve of diode. The relation of turn-on voltage (forward voltage at 100 mA) and neutron fluence is shown in figure 4.6. It reduces with neutron fluence and slope of V-I curve becomes bigger after irradiation. Temperature from the beginning of the experiment until the end of the experiment is controlled around 25.6°C.

Figure 4.7 shows the fitting for each V-I curve as the function 4.4, and fitting parameters are listed in

table 4.3.

$$I = I_0(e^{-V/V_T} - 1) \quad (4.4)$$

where  $I$  and  $V$  are the diode current and voltage across the diode.  $V_T$  is thermal voltage and  $I_0$  is the saturation current, which are assumed the fitting parameters here.

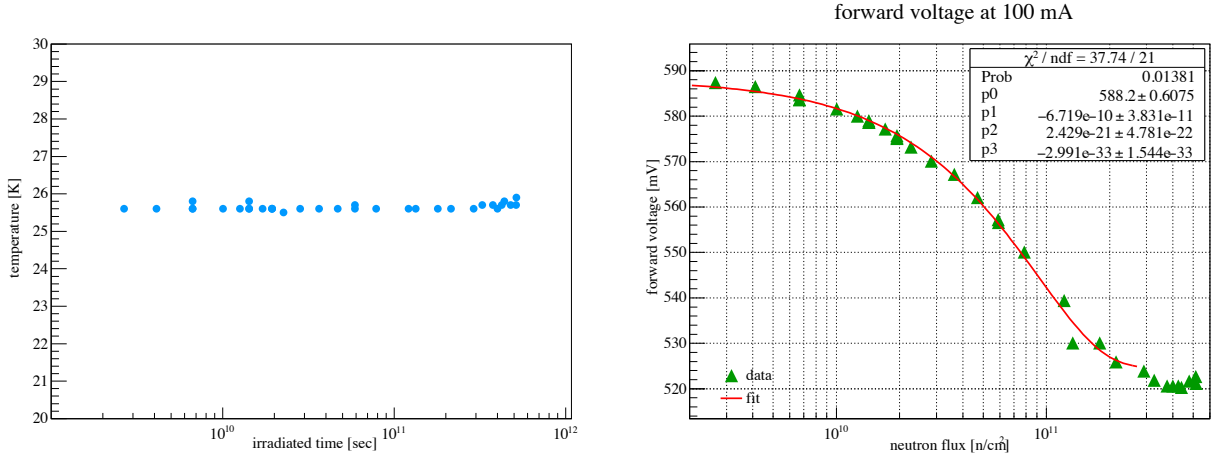


Figure 4.6: The temperature during the irradiation (left). The turn-on voltage decreases with the neutron fluence (right).

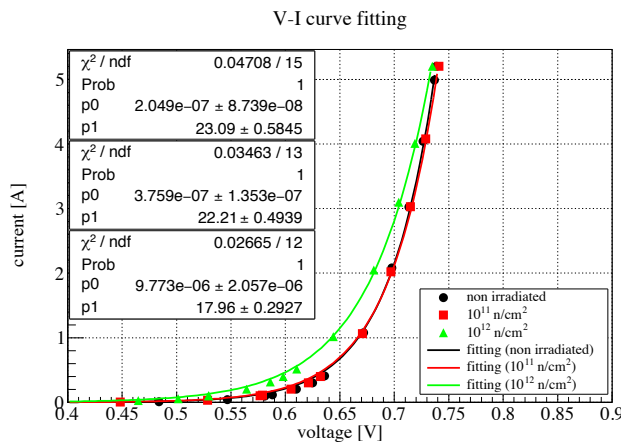


Figure 4.7: Measured trun-on voltage for quench protection diode. It is fitted as diode V-I function. Black and green point represent the original V-I curve and V-I curve after  $10^{12} \text{ n}/\text{m}^2$  irradiation.

irradiated time [sec]	$I_0$	$V_T$	irradiated time [sec]	$I_0$	$V_T$
0	$2.04883 \times 10^{-7}$	23.0918	500	$1.97681 \times 10^{-7}$	23.034
1064	$2.73547 \times 10^{-7}$	22.6213	1505	$3.75863 \times 10^{-7}$	22.2084
4274	$1.35549 \times 10^{-6}$	20.5447	9884	$5.35415 \times 10^{-6}$	18.7640
14008	$9.77339 \times 10^{-6}$	17.9582	68468	$4.15128 \times 10^{-5}$	15.7070

Table 4.3: Fitting parameters for V-I curve.

#### 4.2.4 Electrical property at cryogenic temperature

Since Quench protection diode is connected to the magnets with superconducting wire, the diode must be cooled to the temperature same as superconducting wire, 4.2 K. Therefore, the electrical property at cryogenic temperature needs to be investigated as well.

For the measurement at cryogenic temperature, Quench protection diode is cooled directly by liquid nitrogen at 77 K which shown in figure 4.8. Unlike to the result of irradiation, not only the turn-on voltage but also the V-I curve increases in 77 K. In figure 4.10, the V-I curve at 300 K and 7 K can be fitted by

Temperature [K]	$I_0$	$V_T$	Temperature [K]	$I_0$	$V_T$
300	$8.088 \times 10^{-7}$	21.05	77	$1.969 \times 10^{-12}$	25.95

Table 4.4: Fitting parameters for forward voltage of diode at 300 K and 77 K.

Using this fitting parameters, the forward voltage at 300 K and 77 K can be predicted to 0.92 V and 1.25 V respectively. Compared with the case of room temperature, 0.33 V is increased during the cooling.



Figure 4.8: Measurement of the forward voltage of diode at cryogenic temperature.

#### 4.2.5 Forward voltage at 210 A

Since the operating current for transport solenoid is 210 A, a relation between fitted forward voltage at 210 A and neutron fluence is shown in figure 4.9. The forward voltage increases following the neutron fluence which is assumed as the exponential function.

$$V = \exp(-0.09373 + 8.832 \times 10^{-14} \cdot \phi) \quad (4.5)$$

In the case of COMET phase-II experiment, the neutron at the place of quench protection diode is about  $4.02 \times 10^5$  n/cm<sup>2</sup>/sec with the energy lower than 1 MeV according to PHITS simulation. As for the 280-day operation, the total neutron fluence is estimated to about  $9.73 \times 10^{12}$  n/cm<sup>2</sup> for quench protection diode. Because the displacement cross section of silicon at low energy region is lower than the case of high energy region, irradiation for  $10^{12}$  n/cm<sup>2</sup> at the range from 1 MeV reaches to the effects of  $9.73 \times 10^{12}$  n/cm<sup>2</sup>

irradiation. After  $10^{12}$  n/cm<sup>2</sup> irradiation, the forward voltage at operating current is increased 0.08 V.

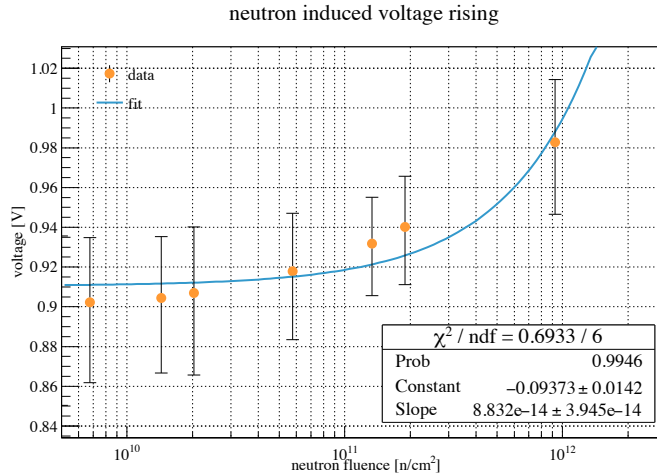


Figure 4.9: Relative increase of the forward voltage versus neutron fluence at room temperature.

Turn-on voltage at 100 mA is proportional to the temperature linearly as

$$V = 1.221 - 0.002077 \cdot T \quad (4.6)$$

Assuming the forward voltage at 210 is also linear to the temperature, the forward voltage is predicted to 1.33 V at 4.2 K and 210 A. Including the voltage change during the irradiation, we assume the forward voltage at 210 A and 4.2 K will increase from 0.9 V to 1.5 V. Even if the forward voltage increases to 1.5V, the temperature rises to about 11 K during the cooling of liquid helium which is calculated by one dimensional Finite Element Method. Without the cooling, the temperature of diode will increase up to 70 K at 10 sec.

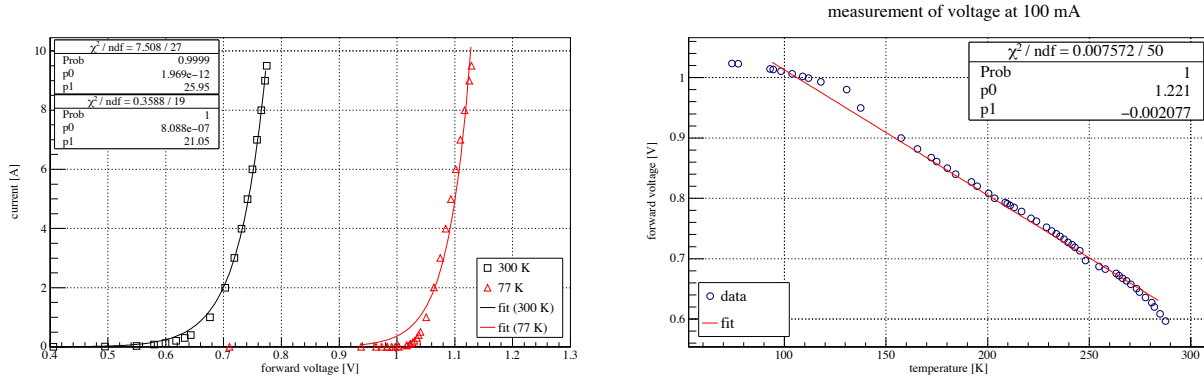


Figure 4.10: Foward V-I curve measured at room temperature and nitrogen temperature without irradiation (left). The measurement of trun-on voltage at 100 mA from room temperature to 77 K (right).

### 4.3 Insulation tape

The conductor of pion capture solenoid is wound by two layers of insulation tape so called pre-preg tape as ground insulation. This insulation tape shown in figure ?? is made of polyimide film covered by

boron free glass with BT and epoxy resin to enhance the mechanical property under the high radiation environment.

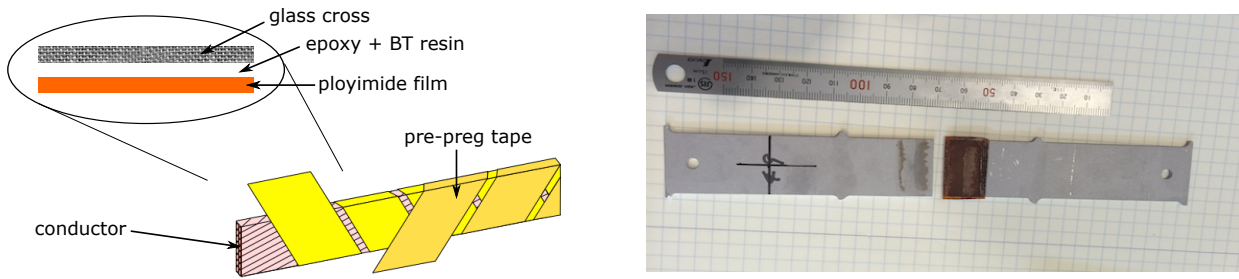


Figure 4.11: Insulation tape is made of glass cross and polyimide film impregnated by BT and epoxy resin (left). The two pieces of insulation tapes are sandwiched with aluminum strip to take tensile test (right).

Four samples, BTGU, BTGK-A, BTGK-B and BTGK-C, made of same material but different rate of BT and epoxy resin are prepared for tensile test. Here, mixing the BT and epoxy resin with different rate can adjust the viscosity of insulation tape. Two samples are struck and sandwiched with aluminum strip (Al-GU-UG-Al) as JIS standards for tensile test are cured by 170°C and 8 hours. Figure ?? shows how the pre-preg tape breaks after tensile test. The result of tensile test for the sample without irradiation is given in figure 4.12, which shows the BTGK-C is the strongest one in these sample. However, the glass layer and resin layer is not struck before the thermal process, which is hard to employ it as the insulation tape in superconducting coil. Considering the mechanical properties may reduce after irradiation, the irradiation of BTGU samples is taken in Takasaki Advanced Radiation Research Institute with cobalt radiation source. As the result shown in figure 4.12 (right), the tensile strength of BTGU sample does not reduce after irradiation, however, surprisingly, the tensile strength increases about 10% after 10 MGy irradiation.

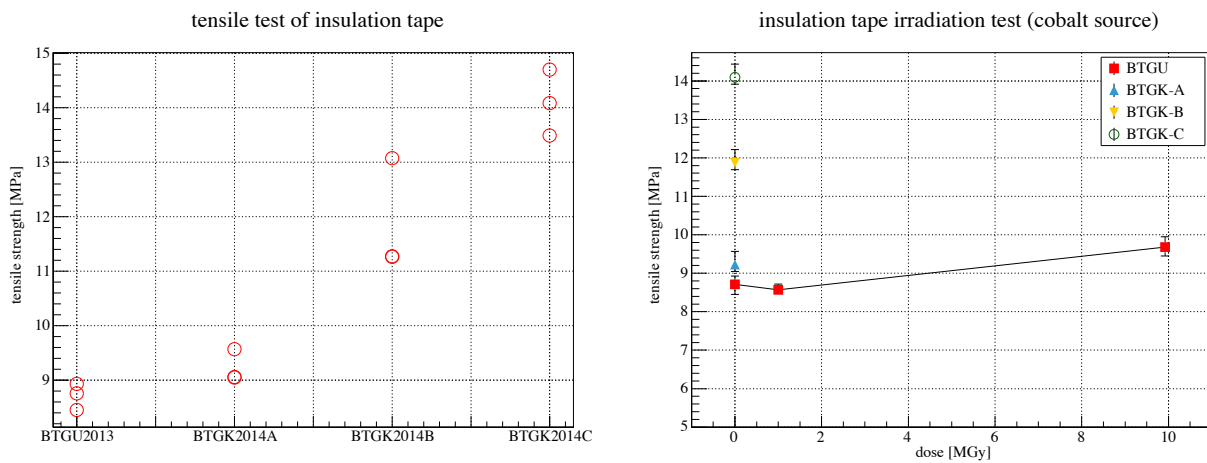


Figure 4.12: 3 samples of each BTGU, BTGK-A, BTGK-B and BTGK-C are tensioned without irradiation (left). BTGU shows no degradation after irradiated with 10 MGy at limit by cobalt  $\gamma$  ray source.

## 4.4 Radiation test for conductor

The degradation of electrical resistivity occurs when the stabilizer irradiated by radiation due to the production of Frenkel pairs. In the cryogenic temperature, since the displaced atoms are difficult to return to

the defect, a depletion region is possible to be generated under the long time irradiation. Radiation damage effects of conductor are necessary to investigate because it may cause the overheat of superconducting coils due to the RRR decreasing and quench.

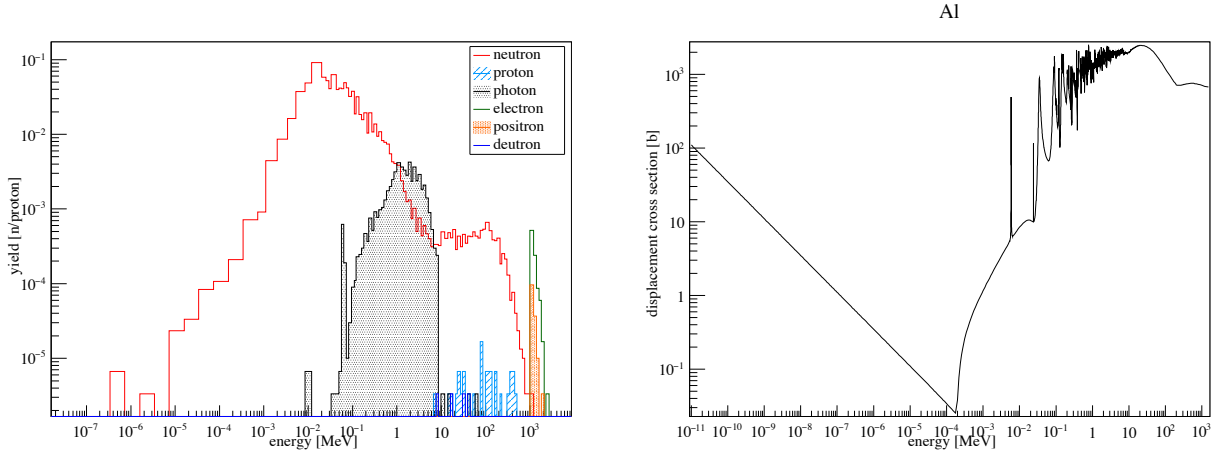


Figure 4.13: all kinds of particles which hit the CS1 coil (left). The displacement cross section of aluminum for neutron (right).

To ensure what kinds of particle hit the superconducting coils, the simulation is taken by PHITS and its yield is shown in figure 4.13. Compared with the other particles, the neutron is most biggest issue for superconducting coils. Furthermore, the energy of neutron in the range from 0.1 MeV dominates the radiation damage, which is about 100 b. Thus, irradiation test of pure aluminum and copper for conductor is studied in Kyoto University Research Reactor Institute (KURRI) with reactor neutron. The pure aluminum and copper samples are set up in the one of beamline from reactor where can irradiate with cryogenic temperature. Neutron fluence is  $1.4 \times 10^{11}$  n/m<sup>2</sup>/sec for fast neutron in terms of the KUR study (31). Figure 4.14 shows the energy spectrum at center of reactor, which is higher than the place where we take irradiation test with factor 30.34.

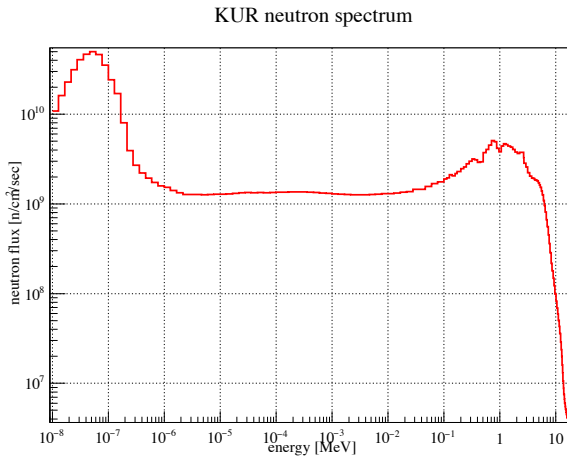


Figure 4.14: Neutron spectrum at core of KUR reactor.

As the result, we observe that the resistivity increases about  $0.03 \text{ n}\Omega\cdot\text{m}$  for aluminum and  $0.01 \text{ n}\Omega\cdot\text{m}$  for copper after  $10^{20} \text{ n}/\text{m}^2$  neutron irradiation. Thus, due to the neutron induced resistivity, the resistivity

of stabilizer at cryogenic temperature should be modified as

$$\rho(T) = \rho_0(T) + \Delta\rho_n(\Phi) + \Delta\rho_{mag}(B) \quad (4.7)$$

where  $\rho_0(T)$  is the resistivity at cryogenic temperature without magnetic field and irradiation.  $\Delta\rho(\Phi)$  and  $\Delta\rho(B)$  are the neutron induced resistivity which depends on the neutron fluence and magnetoresistivity, respectively. Thus, the RRR during the irradiation is given by

$$RRR = \frac{\rho_{RT}}{\rho_0 + f \cdot \phi \cdot t} \quad (4.8)$$

where the factor  $f$  is shown in table 4.5.

Element	Factor [nΩ·m <sup>3</sup> ]
Aluminum	$3 \times 10^{-22}$
Copper	$1 \times 10^{-22}$

Table 4.5: Factor for the neutron induced resistivity.

Since the aluminum with RRR of 2000 and 400 will be employed as strip and stabilizer respectively, the relation between RRR and neutron fluence is shown in figure 4.15. The RRR of aluminum strip and stabilizer for 280-day operation will become 40 or lower for capture solenoid according to the maximum neutron fluence of  $2 \times 10^{21}$  n/m<sup>2</sup> which is predicted by PHITS code (JAM\_INCL4.6\_JENDL4 model). Details of RRR degradation for main superconducting magnets of pion capture solenoid is listed in table 4.6 and figure 4.15 (right).

Name	neutron flux [n/cm <sup>2</sup> /sec]	DPA [DPA/280 days]	RRR (Al strip)	RRR (stabilizer)
CS0	$1.03 \times 10^{10}$	$3.44 \times 10^{-5}$	39	36
CS1	$5.12 \times 10^9$	$2.97 \times 10^{-5}$	77	67
MS1	$4.11 \times 10^9$	$1.82 \times 10^{-5}$	95	80
MS2	$1.20 \times 10^9$	$8.11 \times 10^{-6}$	293	185

Table 4.6: Details of RRR degradation for pion capture solenoid after 280-day operation.

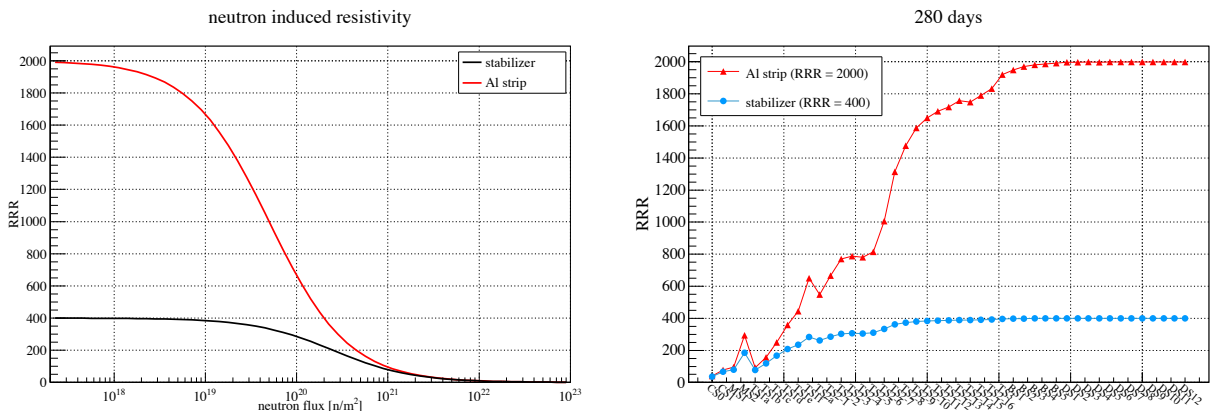


Figure 4.15: Predicted the RRR-neutron curve from the neutron irradiation test in KUR.

#### 4.4.1 Discussion

The radiation induced damage of material can be estimated by one parameter called Displacement Per Atom (DPA) which is given by

$$DPA = \sigma_{dpa} \cdot \phi_i \quad (4.9)$$

where  $\sigma_{dpa}$  and  $\phi_i$  are the displacement cross section and particle flux respectively. The displacement cross section depends on the material, and is a predicting value. Through the DPA, the radiation damage in different energy region is able to be compared. Using the neutron flux and displacement cross section of aluminum in figure 4.13, the DPA can be estimated as follows.

DPA model	DPA calculation [DPA]
BCA + MD	$1.0 \times 10^{-5}$
ABBN	$2.6 \times 10^{-5}$
NRT (Mu2e)	$2.5 \times 10^{-5}$
NRT (COMET)	$3.0 \times 10^{-5}$

Table 4.7: DPA estimation for the neutron irradiation test of pure aluminum.

Here, BCA + MD, ABBN, and NRT (Mu2e) are the estimation with different DPA models from Mu2e collaboration. Our estimation is about  $3.0 \times 10^{-5}$  DPA. J.A. Horak et al. measure the neutron induced resistivity of metals, as a result, the induced resistivity for aluminum is  $382.3 \text{ n}\Omega\cdot\text{cm}$  per  $5.6 \times 10^{-4}$  Frenkel pair <sup>(32)</sup>. In addition, reference <sup>(1)</sup> shows many results of Frenkel pair resistivity of aluminum in table 4.8.

$\rho_{FP}$ [ $\mu\Omega\cdot\text{m}$ ]	Type	Reference
$3.9 \pm 0.6$	Exp D	<sup>(33)</sup>
$4.2 \pm 0.8$	Exp D	<sup>(34)</sup>
$3.2 \pm 0.6$	Exp D	<sup>(35)</sup>
3.4	Exp T(p)	<sup>(36)</sup>
1.32	Exp T(p)	<sup>(37)</sup>
1.35	Exp T(p)	<sup>(38)</sup>
$4.0 \pm 0.6$	Evl E	<sup>(39)</sup>
$4.2 \pm 0.5$	Evl E	<sup>(40)</sup>
4.3	Evl S	<sup>(41)</sup>

Table 4.8: The Frenkel pair resistivity  $\rho_{FP}$  of aluminum. Methods of the data derivation: Exp D is X-ray diffraction method, Exp T is the threshold energy determination for electron irradiation of single crystals at low temperature. Exp T(p) is for the electron irradiation of polycrystals, Evl S is the estimation made with the help of the systematics <sup>(1)</sup>.

It shows that J.A. Horak's data is the maximum value compared with the other references. The relation between DPA and RRR by using these prediction from experimental data is shown in 4.16.

For the COMET phase-II experiment, the DPA peak of CS1 coil is about  $1.1 \times 10^{-5}$  DPA for 280-day operation from the prediction of PHITS code with NRT model. The aluminum strip will not degrade lower than 100 for 280-day operation from this estimation. However, the design has to consider the worst situation for superconducting coils, the uncertainty of the prediction from neutron DPA and neutron fluence needs to be reconsidered.

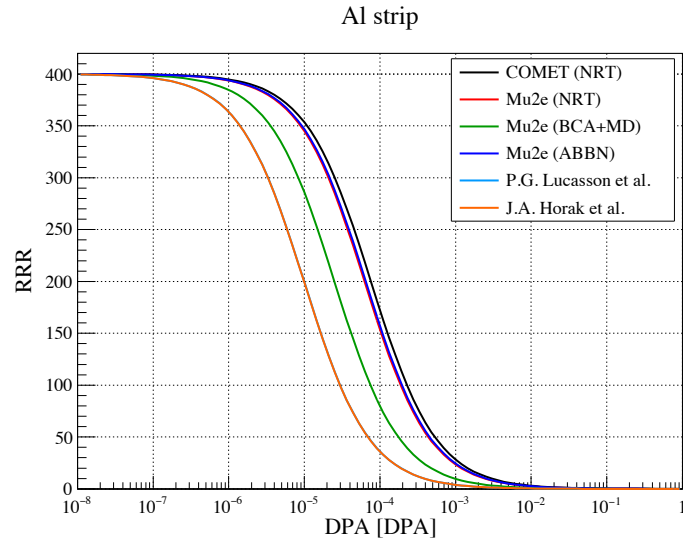


Figure 4.16: A relation between DPA and RRR.



# Chapter 5

## Thermal stability of superconducting solenoids

Radiation will not only generate the heat inside the coils but also cause the damage of superconducting material, which is possible to lead the degradation of cooling strip. Due to the conduction cooling, the consequence of aluminum strip degradation is over-heat and quench, which are the major issue for COMET superconducting magnets. Here, the thermal property of the most dangerous coil, CS1 coil, is analysed.

### 5.1 Quench estimation

Quench plays a significant role in superconducting magnet performance. Since over 2000 A current is flowing inside the superconducting wire, the resistance of NbTi will increase suddenly when superconducting state turns to the normal state. If this current cannot decay quickly, the quenching temperature will increase highly and cause the unrecoverable burn-out of superconducting wire.

In Sep. 2008, the accident caused by quench occurred in LHC superconducting magnet. As the consequence, the bus bar is burned out in the interconnect. It costs half year to fix the superconducting magnet in LHC accident. As for the COMET experiment, it is not possible to do the maintenance during the experiment due to the residual radiation of the solenoid. Thus, the quench estimation is necessary to know the temperature after magnet quenched.

One parameter called MIITs is estimated for the worst situation of quench. To calculate the MIITs, the specific heat and thermal conductivity from cryogenic temperature to room temperature is required. The specific heat and electrical resistivity of copper, aluminum and NbTi are fitted with experimental data correctly.

#### 5.1.1 Specific heat

There are two models for lattice specific heat, the Debye model and Einstein model<sup>(42)</sup>. In Debye model, the phonon energy is written as

$$U = \int d\omega D(\omega) \left( \frac{\hbar\omega}{e^{\hbar\omega/\tau} - 1} \right) \quad (5.1)$$

where  $D(\omega)$  is the density of state,  $\omega$  is the wave number. The density of state is described as  $V\omega^2/2\pi^2v^3$ , than the specific heat can be solved as

$$C_V = \frac{\partial U}{\partial T} = 9Nk_B\left(\frac{T}{\theta}\right)^3 \int_0^{x_D} dx \frac{x^4 e^x}{(e^x - 1)^2} \quad (5.2)$$

where  $\theta$  is the Debye temperature and equals to  $\frac{\hbar v}{k_B} \cdot (\frac{6\pi^2 N}{V})^{1/3}$ .  $x_D$  comes from the cut off wave number and equals to  $\theta/T$ . In the cryogenic temperature which is less than the Debye temperature ( $T \ll \theta$ ), The specific heat can be approach as

$$C_V \cong \frac{12\pi^4}{5} Nk_B\left(\frac{T}{\theta}\right)^3 \quad (5.3)$$

Debye model describes the contribution of lattice on specific heat. However, the contribution of electrons is treated approximately as the free-electron model. The electronic contribution to specific is

$$C_V = \gamma T = \frac{1}{2}\pi^2 Nk_B \frac{T}{T_F} \quad (5.4)$$

where  $\gamma = \pi^2 D(\epsilon_F) k_B^2 / 3$  is called the Sommerfeld constant and  $T_F$  is the Fermi temperature, respectively. Combining the lattice and electronic contribution, the specific heat can be written as

$$C_V \cong \gamma T + \beta T^3 \quad (5.5)$$

As for the aluminum, the Debye temperature is 428 K and the Sommerfeld constant is 1.35 mJ/mol/K<sup>2</sup>. However, it does not agree with the experimental data. Therefore, the specific heat of aluminum is fitted as polynomial function with different range of temperature. The details is shown in table 5.1 and the fitting result is given in figure 5.1. The experimental data is given in reference <sup>(43)</sup>. The fitting function does not agree with the experimental in the range from 0 K to 2 K. Because the initial temperature is 4.5 K, it will not affect the calculation here.

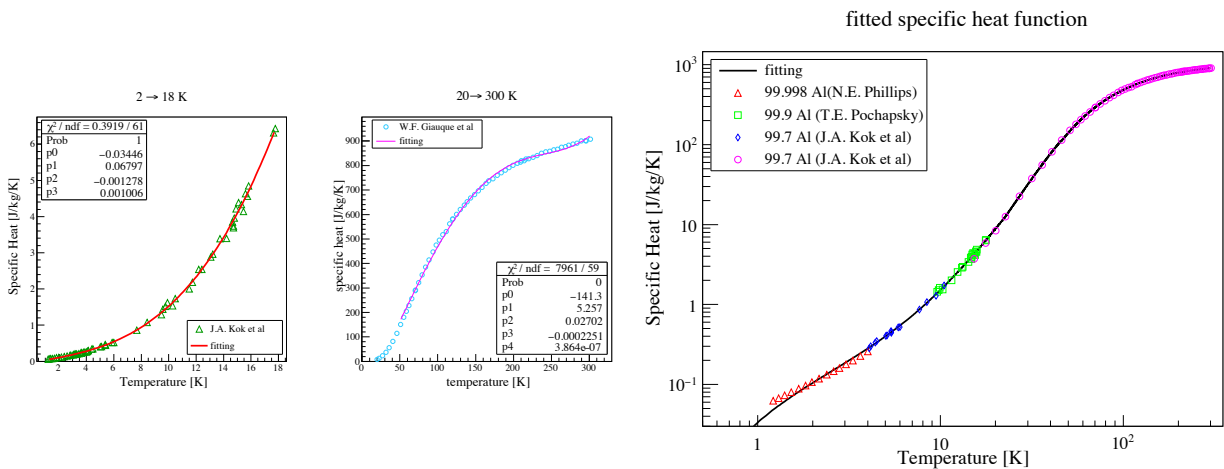


Figure 5.1: The specific heat of aluminum is fitted from the range from 4.5 K to 22.67 K, 22.67 K to 46 K and 46 K until 350 K respectively.

$$C = p_0 + p_1 \cdot T + p_2 \cdot T^2 + p_3 \cdot T^3 \quad (5.6)$$

$T_{lower}$	$T_{upper}$	$p_0$	$p_1$	$p_2$	$p_3$
0	22.67	-0.03446	0.06797	-0.001278	0.001006
22.67	46	$7.88 \times 10^{13}$	6.93201	-0.07139	46.4363
46	350	6.273517	-0.5469	0.000925	-156.932

Table 5.1: The details for fitting the aluminum specific heat.

The Copper specific heat is fitted as polynomial function with the experimental data in reference <sup>(43)</sup>. Here  $p_0$  and  $p_2 \cdot T^2$  are the correction of specific heat.  $p_1 \cdot T$  and  $p_3 \cdot T^3$  are the lattice specific heat and electronic specific heat, respectively. The fitting parameters are listed in table 5.2 and the result is shown in figure 5.2.

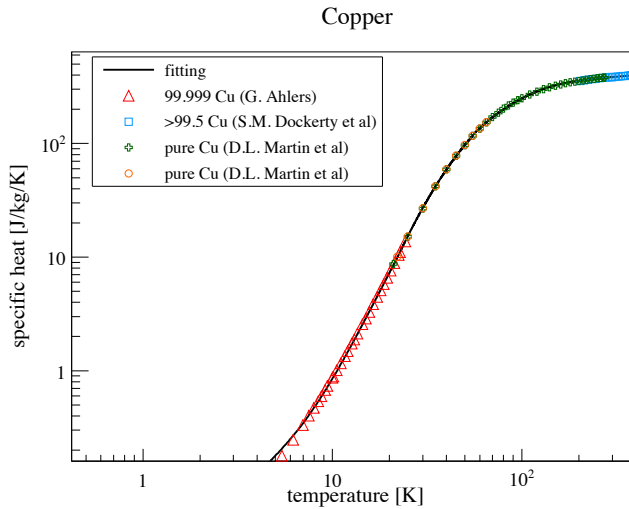


Figure 5.2: Fitted copper specific heat curve.

$T_{lower}$	$T_{upper}$	$p_0$	$p_1$	$p_2$	$p_3$
0	23	-0.104251	0.0832507	-0.0118811	0.00131157
23	55	25.2218	-3.41019	0.144053	-0.000939968
55	250	-158.094	6.40481	-0.0273429	$4.08432 \times 10^{-6}$

Table 5.2: Fitting parameters for copper specific heat.

$T_{lower}$	$T_{upper}$	$p_0$	$p_1$	$p_2$	$p_3$	$p_4$
0	$T_c(B)$	0	$64 \times B$	0	49.1	0
$T_c(B)$	26.358	0	928	0	16.24	0
28.358	50.99	41383	-7846.1	553.71	11.9838	-0.2177
50.99	165.8	$-1.53 \times 10^6$	83022	-716.3	2.976	-0.00482
165.8	496.54	$1.24 \times 10^6$	13706	-51.66	0.09296	$-6.29 \times 10^{-5}$
496.54	1000	$2.45 \times 10^6$	955.5	-0.257	0	0

Table 5.3: The fit parameters for NbTi specific heat.

The NbTi specific heat is same to the CUDI parameters which is given in ROXIE's database <sup>(44)</sup>. The fit

parameters are reported in table 5.3.

$$C = \rho_{NbTi} \cdot (p_0 + p_1 \cdot T + p_2 \cdot T^2 + p_3 \cdot T^3 + p_4 \cdot T^4) \quad (5.7)$$

### 5.1.2 Electrical resistivity

Because of collisions of free electrons with impurities, lattice and phonons, it generates the electrical resistivity. The electrical resistivity is obtained from the free electron gas model.

$$\rho = \frac{1}{\sigma} = \frac{m}{ne^2\tau} \quad (5.8)$$

In the room temperature, the collisions of electrons with phonon is dominated the electrical resistivity. However, only the collisions of electrons with impurities and defects occurs in the cryogenic temperature. Therefore, the total resistivity can be written as

$$\rho = \rho_L + \rho_i \quad (5.9)$$

where  $\rho_L$  is the resistivity from the phonon collisions,  $\rho_i$  is the resistivity from the scattering of electron waves with impurities.  $\rho_L$  will become 0 when the temperature is close to 0 K. There are two ways to fit the electrical resistivity.

- Fit the electrical resistivity directly.
- Fit the thermal conductivity first, then convert it with Wiedemann-Franz law.

In reference <sup>(45)</sup>, it gives the function to fit the copper electrical resistivity. Its function contains temperature and RRR dependence like

$$\rho(T, RRR) = \rho_0 + \rho_i + \rho_{i0} \quad (5.10)$$

$\rho_0$  and  $\rho_i$  are same to the two terms in equation 5.9, which indicate the resistivity in cryogenic temperature and room temperature, respectively.  $\rho_{i0}$  is the correction term of  $\rho_0$  and  $\rho_i$ . Hence  $\rho_0$  depends on the material purity and structure, while  $\rho_i$  depends on the temperature. Each term are given by

$$\rho_0 = \frac{\rho_{RT}}{RRR} \quad (5.11)$$

$$\rho_i = \frac{p_1 \cdot T^{p_2}}{1 + p_1 \cdot p_3 \cdot T^{(p_2-p_4)} \cdot \exp\left\{-\left(\frac{p_5}{T}\right)^{p_6}\right\}} \quad (5.12)$$

$$\rho_{i0} = p_7 \cdot \frac{\rho_i \cdot \rho_0}{\rho_i + \rho_0} \quad (5.13)$$

As for the copper, the electrical resistivity at room temperature is  $1.553 \times 10^{-8} [\Omega \cdot m]$ , and the same fitting parameters is employed in MIITs simulation which is listed in table 5.4.

$p_1$	$p_2$	$p_3$	$p_4$	$p_5$	$p_6$	$p_7$
$1.171 \times 10^{-17}$	4.49	$3.841 \times 10^{10}$	1.14	50	6.428	0.4531

Table 5.4: NIST fitting parameters for copper electrical resistivity.

On the other hand, the electrical resistivity is able to be achieved from the thermal conductivity. Reference <sup>(46)</sup> mentions the predicting of thermal conductivity which based on a set of semi-empirical equations presented by Hust et al. <sup>(47)</sup>. The thermal conductivity is written as

$$K = \frac{1}{W_0 + W_i + W_{i0}} \quad (5.14)$$

where  $W_0$  and  $W_i$  represent the electron-defect and electron-phonon interactions respectively, which is similar to the NIST equation.  $W_{i0}$  is necessary to produce acceptable fits. Each term is given as follows.

$$W_0 = \frac{\beta}{T} \quad (5.15)$$

$$W_i = \frac{p_1 \cdot T^{p_2}}{1 + p_1 p_3 T^{(p_2+p_4)} \exp\left\{-\left(\frac{p_5}{T}\right)^{p_6}\right\}} + W_c \quad (5.16)$$

$$W_{i0} = p_7 \cdot \frac{W_i W_0}{W_i + W_0} \quad (5.17)$$

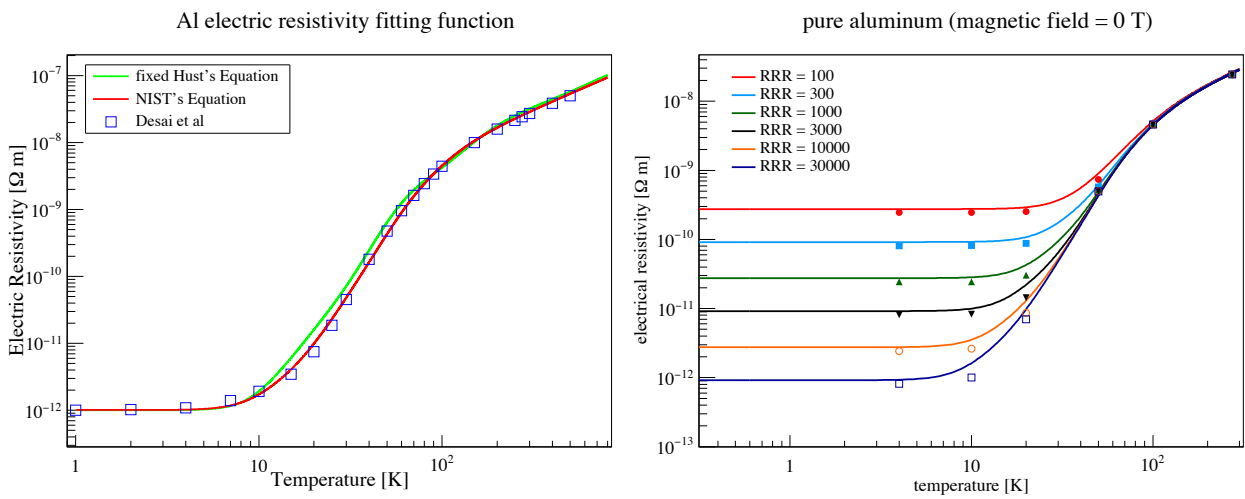
The parameter  $\beta$  is the function of the residual resistivity  $\rho_0$ , which can be represented as Wiedemann-Franz law.

$$\beta = \frac{\rho_0}{L_0} = \frac{\rho_{RT}}{L_0} \cdot \frac{1}{RRR} \quad (5.18)$$

The  $W_c$  is correction parameter for only the pure aluminum which is compared with experimental data.

$$W_c = -0.0005 \cdot \ln\left(\frac{T}{330}\right) \cdot \exp\left\{-\left(\frac{\ln(T/380)}{0.6}\right)^2\right\} - 0.0013 \cdot \ln\left(\frac{T}{110}\right) \cdot \exp\left\{-\left(\frac{\ln(T/94)}{0.5}\right)^2\right\} \quad (5.19)$$

As for the pure aluminum, the fitting parameter for NIST and Hust equation is listed in table 5.5 and 5.6 respectively.



(a) Fixed the Hust's equation and NIST's equation of aluminum electric resistivity.

(b) Comparison of the aluminum electric resistivity with different RRR.

Figure 5.3: Fitted aluminum resistivity.

$p_1$	$p_2$	$p_3$	$p_4$	$p_5$	$p_6$	$p_7$
$1.671 \times 10^{-17}$	4.36	$2.841 \times 10^{10}$	1.18	64	4.428	1.2031

Table 5.5: NIST fitting parameter for pure aluminum.

$p_1$	$p_2$	$p_3$	$p_4$	$p_5$	$p_6$	$p_7$
$4.716 \times 10^{-8}$	2.446	623.6	-0.16	130.9	2.5	0.8168

Table 5.6: Hust fitting parameter for pure aluminum.

Figure 5.3a shows the comparsion of the Hust and NIST equation with experimental data by using these fitting parameters for pure aluminum ( $\text{RRR} = 10000$ )<sup>(48)</sup>. The fixed Hust equation is higher than the experimental data in the range from 10 K to 100 K. Hence the Hust equation still needs to be fixed in future.

In figure 5.3a, only the aluminum with 10000 of RRR is compared to the fitting function. While, the pure aluminum with different RRR must be agreed to the fitting function and it is shown in figure 5.3b. (The experimental data is obtained from Prof. Nakamoto.) The fixed NIST equation is employed in here. The fitting function is higher than experimental data about factor 0.2, and its difference is only shown in low temperature. As for the high temperature, it has good agreement with data.

## Magnetoresistivity

Due to the external magnetic field, the mean free path will be shortened and the collisions between electrons and phonon is increased, which leads to the electrical resistivity increasing. The Kohler's plot is the most common expression of the magnetoresistivity. The Corruccini<sup>(49)</sup> gives the equation to calculate the magnetoresistivity in reference<sup>(50) (51)</sup>. The electrical resistivity in the high field can be written as

$$\rho(B, T) = \rho(0, T) + \rho(0, T) \cdot \frac{h^2 \cdot (p_0 + p_1 \cdot h)}{p_2 + p_3 \cdot h + p_4 \cdot h^2} \quad (5.20)$$

$$h = B \cdot \frac{\rho_{\text{ref}}}{\rho(0, T)} \cdot 10 \quad (5.21)$$

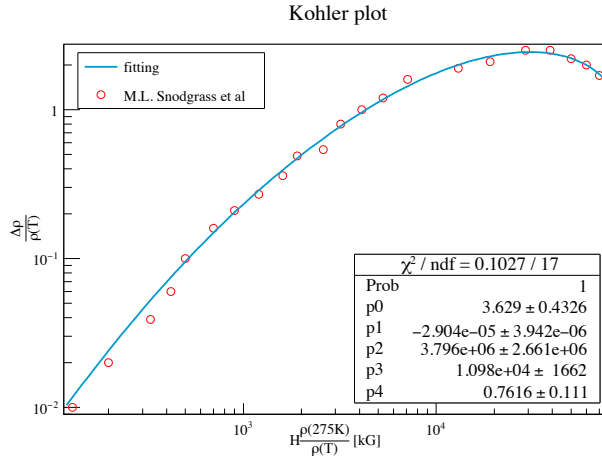


Figure 5.4: Fitted the Kohler plot with experimental data for pure aluminum.

where  $\rho_{ref}$  is  $2.75 \times 10^{-8} [\Omega \cdot m]$  and  $\rho(0, T)$  is the electrical resistivity without magnetic field. As for the aluminum, the fitting parameters are listed in table 5.7 and the fitted Kohler plot is shown in figure 5.4.

$p_0$	$p_1$	$p_2$	$p_3$	$p_4$
3.62857	$-2.90419 \times 10^{-5}$	$3.79649 \times 10^6$	10975.9	0.761609

Table 5.7: Fitting parameters for pure aluminum magnetoresistivity.

As for the copper, the same fitting equation for copper magnetoresistivity in ROXIE is employed in here. It is fitted as the polynomial function which is given as follows.

$$\begin{aligned}\rho(B, T) &= \rho(0, T) + \rho(0, T) \cdot 10^h \\ h &= p_0 + p_1 \cdot \log_{10}x + p_2 \cdot (\log_{10}x)^2 + p_3 \cdot (\log_{10}x)^3 + p_4 \cdot (\log_{10}x)^4 \\ x &= \frac{1.553 \times 10^{-8} \times B}{\rho(0, T)}\end{aligned}$$

$p_0$	$p_1$	$p_2$	$p_3$	$p_4$
-2.662	0.3168	0.6229	-0.1839	0.01827

Table 5.8: Fitting parameters for copper magnetoresistivity.

### 5.1.3 Thermal conductivity

Thermal conductivity can be obtained from the electric resistivity by using Wiedemann-Franz law, which is written as

$$k = \frac{L_0 \cdot T}{\rho} \quad (5.22)$$

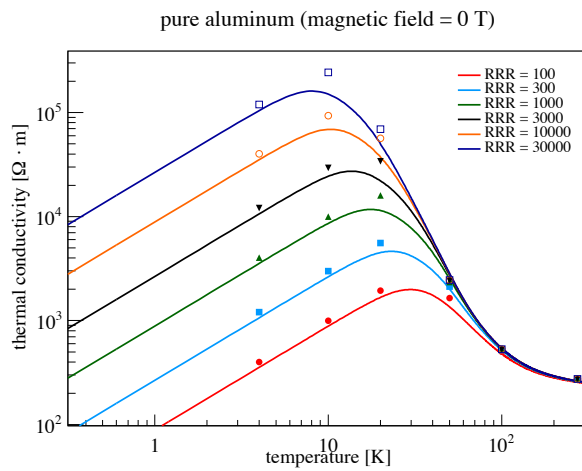


Figure 5.5: Thermal conductivity of aluminum with different RRR.

where  $\rho$  is the resistivity, and Lorentz constant  $L_0$  is defined as

$$L_0 = \frac{\pi^2}{3} \left( \frac{k_B}{e} \right)^2 = 2.44 \times 10^{-8} W \cdot \Omega / K^2 \quad (5.23)$$

The thermal conductivity used in thermal estimation is shown in figure 5.5.

### 5.1.4 MIITs

Because over 2000 A current will generate the joule heat inside the coils, the wire has a risk of burn-out after a quench. Usually, there is external sump resistor to dissipate the stored energy in magnets. Once the quench has been detected, the power supply will be switched off and the current decays due to the dump resistor. The current decay can be presented as

$$I = I_0 \cdot \exp\left(-\frac{R}{L}t\right) \quad (5.24)$$

where  $L$  is the inductance of magnet. The speed of current decay depends on the inductance and resistance and the current can totally decay in the time of  $\tau = L/R$ . The quenching temperature can be restrained if the current decays quickly.

Due to the stored energy is  $I^2(t)R(T)$ , a relation between the time dependence of the current after quench and the maximum temperature can be established. The temperature change during the a time interval  $dt$  can be written as

$$dT = \frac{1}{C(T)} R(T) I^2(t) dt \quad (5.25)$$

where specific heat  $C(T)$  and resistance  $R(T)$  depend on the temperature, and the current  $I(t)$  depends on the time. Separating and integrating the time term and the temperature term, one relation can be obtained

$$f(T_{max}) = \int_0^\infty I^2(t) \cdot dt = \int_{T_0}^{T_{max}} \frac{C(T)}{R(T)} \cdot dT \quad (5.26)$$

The unit of the time integral over the square of the current is usually defined as  $10^6 \cdot A^2 \cdot sec$ , which sometimes is called as "MIITs". As for COMET superconducting magnet, the conductor consists of NbTi superconducting filament, copper matrix and aluminum stabilizer. Thus, the specific heat  $C(T)$  and resistance  $R(T)$  need to average like

$$C(T) = \gamma_{Cu} \cdot C_{Cu}(T) \cdot A_{Cu} + \gamma_{NbTi} \cdot C_{NbTi}(T) \cdot A_{NbTi} + \gamma_{Al} \cdot C_{Al}(T) \cdot A_{Al} \quad (5.27)$$

$$R(T) = \left( \frac{A_{Cu}}{\rho_{Cu}(T)} + \frac{A_{Al}}{\rho_{Al}(T)} \right)^{-1} \quad (5.28)$$

where  $A$  and  $\gamma$  are the cross section and density respectively. Noting that the unit of  $C(T)$  must be  $[J/K/m^3]$  and the unit of each material's specific heat is  $[J/K/kg]$ . The reason why the resistance of NbTi is not included because the resistance of NbTi becomes so high that the current only flows into aluminum stabilizer and copper matrix when quench happens. The parameters used in MIITs calculation is listed as follows.

$I_0$	$R$	$L$	$\tau$	$T_0$	Al:Cu:NbTi
2700 A	0.185 $\Omega$	12.69 H	68.65 sec	4.5 K	7.3:1:1

Table 5.9: The parameters for MIITs estimation of CS1.

The resistance in table 5.9 is the resistance of dump resistor, which is calculated by assuming the allow-

able voltage of 500 V. The MIITs curve with 5.5 Tesla for different RRR is shown in figure 5.6. Since the MIITs calculated from time term is  $250 \text{ MA}^2\text{sec}$ , the maximum temperature will exceed 260 K if the RRR drops to 100 (90-day continuous operation).

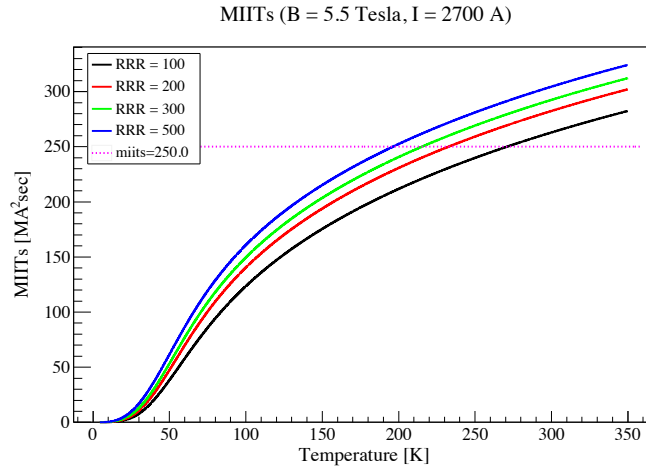
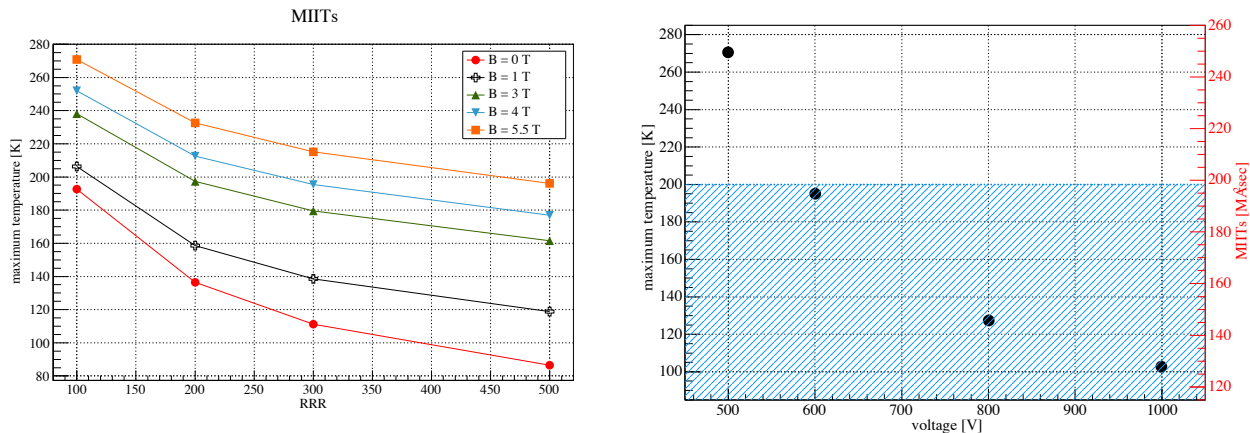


Figure 5.6: The MIITs calculation of CS1 coils with 5.5 Tesla magnetic field and 2700 A current.

Figure 5.7a shows the prediction of maximum temperature from MIITs in different magnetic field. Even the magnetic field becomes 0 Tesla, the maximum temperature is still close to 200 K if RRR drops to 100. Due to the conduction cooling, 200 K is quite high for the superconducting magnets. Following the temperature increasing, it is possible to lead to the consequence of unstuck insulation tape. To avoid the overheat after quench, the voltage should be increased. Figure 5.7b gives the relation between voltage and MIITs predicted maximum temperature. To reduce the maximum temperature after quench, the MIITs should be restrained under  $200 \text{ MA}^2\text{sec}$  and the voltage must be higher than 600 V.



(a) The maximum temperature after magnet quench predicted by MIITs calculation.

(b) A relation between voltage and maximum temperature predicted by MIITs.

Figure 5.7: Improvement of power supply according to the results of MIITs estimation.

However, MIITs can only estimate the maximum temperature of the worst situation. As the case of COMET superconducting magnets, there are aluminum stabilizer is enclosed around the coils. The current decay will be more quickly for the real case due to the aluminum stabilizer self resistance. Furthermore,

the magnetic field decay is not considered in MIITs estimation as well. Thus, the quench simulation is necessary for estimation of the temperature after quench.

## 5.2 Cooling estimation

To analyse the thermal stability of superconducting magnet, a thermal simulation code for COMET superconducting magnet has been developed. This code bases on the three dimensional equation (52), which is written as

$$\gamma C \frac{dT}{dt} = k_x \frac{\partial^2 T}{\partial x^2} + k_y \frac{\partial^2 T}{\partial y^2} + k_z \frac{\partial^2 T}{\partial z^2} + W \quad (5.29)$$

where  $\gamma$ , C, k and W are material's density, specific heat, thermal conductivity and heat generation, respectively. The specific heat only affects the speed of temperature change, and maximum temperature change during the cooling is affected by the term of thermal conductivity and heat generation. Considering the insulation tape has the worse thermal conductivity, the thermal conductivity of conductor is able to be approached like

$$\frac{\sum_{i=1}^{\infty} l_i}{k} = \sum_{i=1}^{\infty} \frac{l_i}{k_i} \quad (5.30)$$

The temperature margin for COMET superconducting magnets can be solved by using the result of energy deposition and neutron flux from PHITS code.

### 5.2.1 Geometry

The geometry which used in thermal analysis is shown in figure 5.8. CS1 coils have 9 layers and 270 turns totally, and aluminum strips with RRR of 2000 are inserted into each layer. Because there is a GFRP spacer in the edge of each layer, aluminum strips only can be inserted from single side. Every aluminum is connected to the 2 phase LHe cooling pipe with 4.5 K. On the top of coils, one aluminum supporter with 5 cm suppresses the coils from hoop stress.

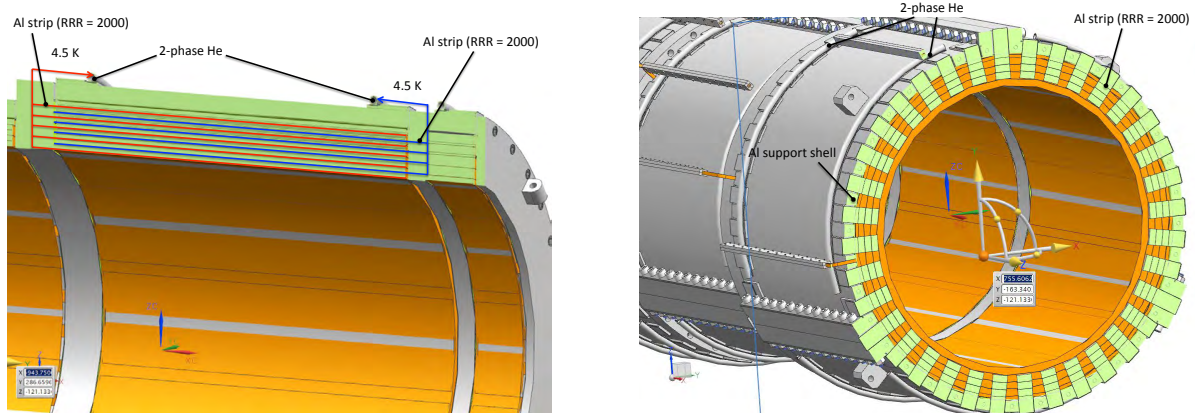


Figure 5.8: Details of the geometry used in magnet thermal simulation.

### 5.2.2 Heat generation

During the operation, heat generation inside the superconducting magnet is easy to cause the quench of magnet. Several main heat generations are listed in table 5.10. Thermal radiation is the absorption or emitting of the electromagnetic wave energy. AC loss is occurred by the alternating magnetic field. Because the prompt radiation contributes 172.5 W in heat load, the others can be neglected in simulation.

	Heat load [W]		Heat load [W]
Thermal radiation	4.16	Supporter	4.41
Current lead	2.00	Residual gas	0.20
AC loss	0.50	Radiation	172.48

Table 5.10: Heat generation for the capture solenoid.

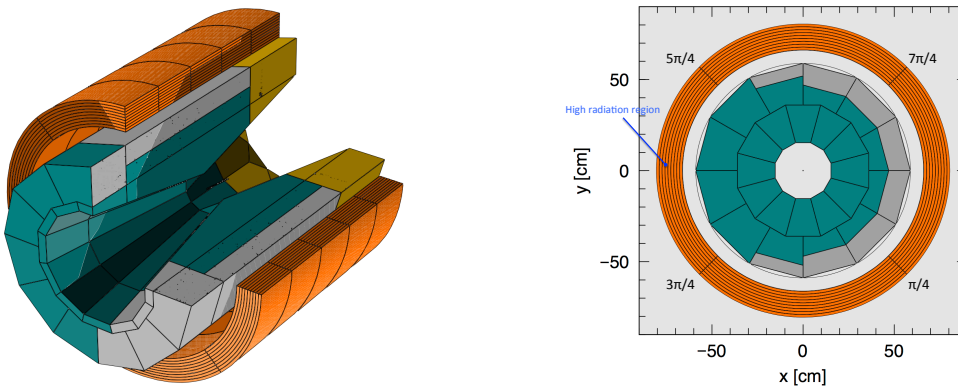


Figure 5.9: Mesh cutting of CS1 coils.

The heat load (energy deposition) is calculated by PHITS code with realistic shielding geometry in figure 5.9. Superconducting coils consist of NbTi, Al and Cu with  $3.80 \text{ g/cm}^3$  are cut for 5 parts along the z direction, 4 parts along the azimuthal direction and 9 parts along the radius direction in calculation. As the result shown in figure 5.10, the peak is located on the place 40 cm far from the production target along the z direction, and from  $3\pi/4$  to  $5\pi/4$  along the azimuthal direction. The energy deposition of inner layer is about 3 times higher than the outer layer's.

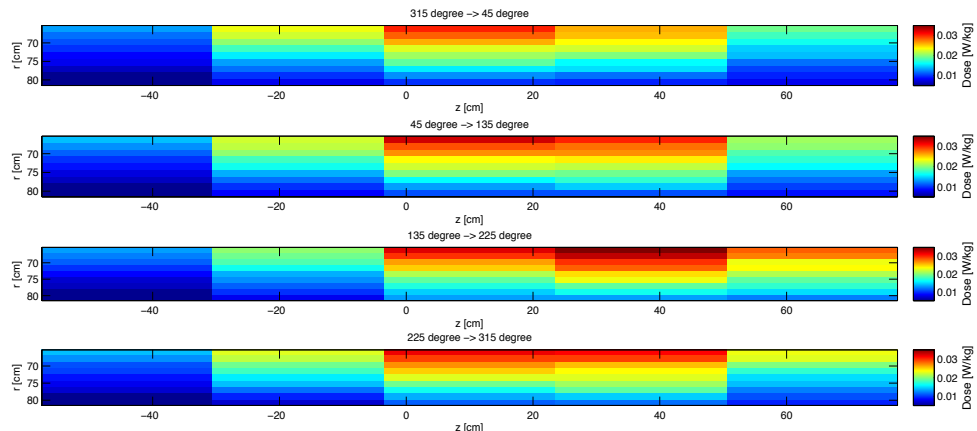


Figure 5.10: Calculated the energy deposition distribution with realistic radiation shield geometry.

### 5.2.3 Maximum temperature of cooling

The parameters used in thermal analysis for CS1 coil is listed in table 5.11. The specific heat only affects the speed of heat transfer and thermal conductivity has no remarkable in range from cryogenic temperature to about 20 K for both copper and aluminum, therefore the specific heat and thermal conductivity are set to constant which does not change with temperature here. However, the thermal conductivity of insulation tape is still unknown, so it is supposed to 0.01 W/m/K which is worse than Kapton tape. Its thermal conductivity although depends on the temperature, setting it to one constant is the worst circumstances for CS1 coil.

Al strip thickness	1mm	Conductor cross section	15 mm × 4.73 mm
Insulation tape thickness	0.075 mm × 2	Insulation thickness	0.8 mm
Al:Cu:NbTi	7.3:1:1	Supporter shell thickness	50 mm
End strip to helium	25 cm	Al density	2700 kg/m <sup>3</sup>
Conductor density	4000 kg/m <sup>3</sup>	Insulation tape density	1420 kg/m <sup>3</sup>
Tape thermal conductivity	0.01 W/m/K	Al specific heat	0.225 J/kg/K
Conductor specific heat	0.16 J/kg/K	Tape specific heat	1090 J/kg/K

Table 5.11: Parameter setting in thermal estimation of CS1 coils.

Due to the finite difference method used in thermal simulation, the result will grow up to infinite if the geometry's mesh and time mesh is not proper in calculation. Here, as for the issue of meshing, the proper mesh for thermal analysis in this time is founded and listed in table 5.12.

Axis	Meshing	Length
z	45	135 cm
$\phi$	4	503 cm
r	19	14.4 cm
time	0.0001 sec	

Table 5.12: Meshing set in thermal analysis of CS1 coils.

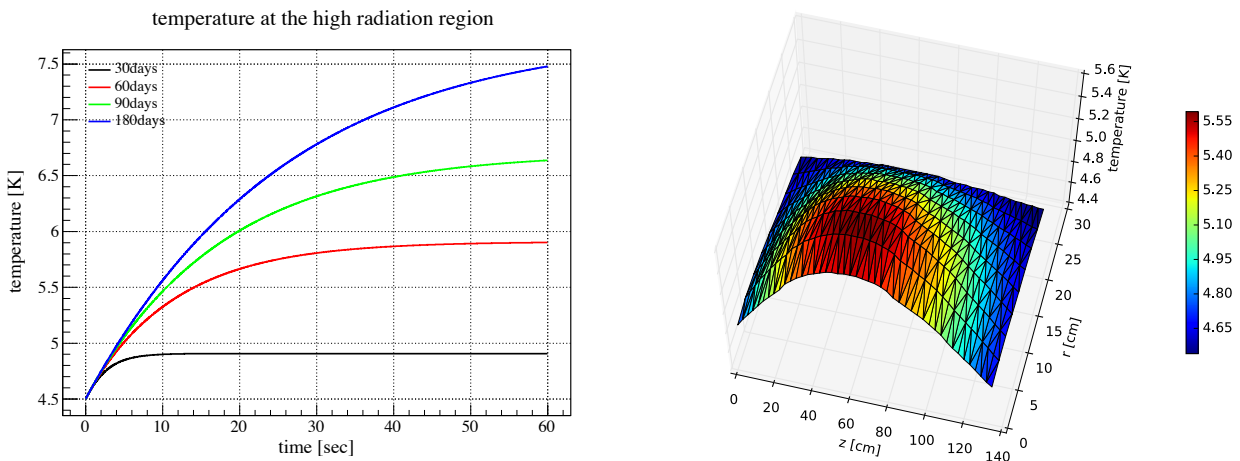


Figure 5.11: Calculated the temperature rising during the operation.

Superconducting coils have a risk of quench when its temperature closes to the current sharing temperature. Thus, the peak of temperature must be suppressed under the current sharing temperature for securing

the coils from quench. According to K. H. Mess's book, the current sharing temperature is given by

$$T_{cs} = T_0 + (T_c - T_0) \cdot \left(1 - \frac{I}{I_c(T_0)}\right) \quad (5.31)$$

where  $T_0$  is the initial temperature,  $I$  is the operating current, and  $I_c(T_0)$  is the critical current in initial temperature. The current sharing for COMET CS1 coils is 5.6 K (Dr. Sasaki's work).

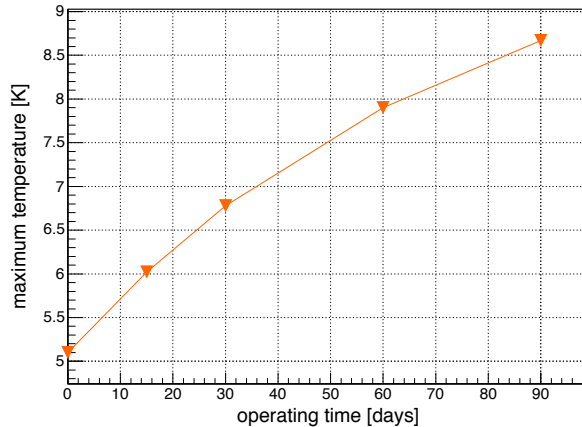


Figure 5.12: Maximum temperature for the original coil structure.

Figure 5.11 gives the temperature distribution of 9 layers of conductor and the temperature change with time. As for figure shown on the left, following the operation time increases, it needs more time to become stable. The temperature peak is in the middle of CS1 and innermost layer. Maximum temperature given in figure 5.12 and 5.13 is the peak temperature in CS1 coils. As for the original design, which shown in figure 5.12, the peak temperature will reach to the current sharing temperature after 25-day operation. Considering the simulation uncertainty, only 10-day continuous operation is allowed for phase-II experiment. Since the superconducting magnet needs almost 1 month to be cooled down to 4.2 K, the plan of 10-day operation wastes a lot of beam time for experiment. Therefore, the design must be optimized as follows.

- Insert the aluminum strips from two sides, and 3/4 part along the azimuthal direction is cooled from both side.
- Shorten the length of aluminum strip which connects to the cooling pipe from 25 cm to 5 cm.
- Enlarge the thickness of inner aluminum strip from 1 mm to 3 mm.

Because the coils will be wound to the next layer in the edge of solenoid, only 3/4 part of coils is possible to be cooled from both side. It may be hard to wind the coils if the thickness of all aluminum strips are increased. However, as the figure 5.10 already shown, the peak of energy deposition is in the inner layer of all coils. Thus, increasing the thickness of inner strip is not only possible to reduce the temperature peak but also easy to wind. After these modifications have been employed, in figure 5.14, the maximum temperature for 60 day continuous operation is 6.2 K (orange line). Operating for more than 30 days is feasible for phase-II experiment.

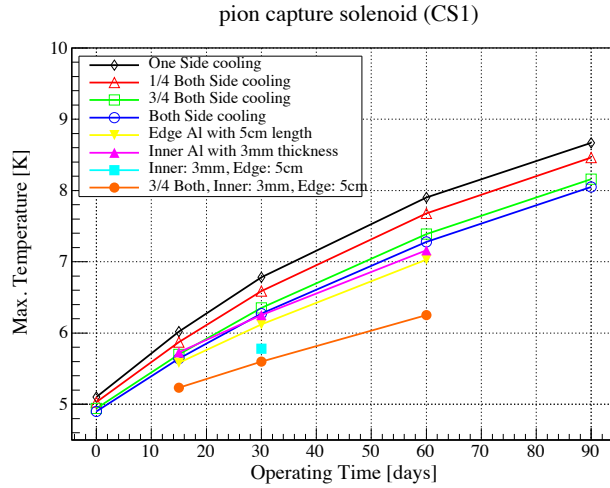


Figure 5.13: The maximum temperature against the operation time.

In previous parameter setting, the only unknown parameter is the thermal conductivity of the insulation tape. The thermal conductivity of ordinary Kapton tape at 4.2 K is around 0.01 W/m/K and it increases with temperature (53). As for the insulation tape, it develops for COMET experiment to enhance the radiation resistance, thus there is no reference shown its thermal conductivity. Figure 5.14 gives the relation between the thermal conductivity of insulation tape and the peak temperature for 30 day operation. The maximum temperature will rise close to the current sharing temperature for 30 day operation if the thermal conductivity is worse than 0.003 W/m/K. Therefore, the thermal conductivity of insulation tape is necessary to take a measurement in future.

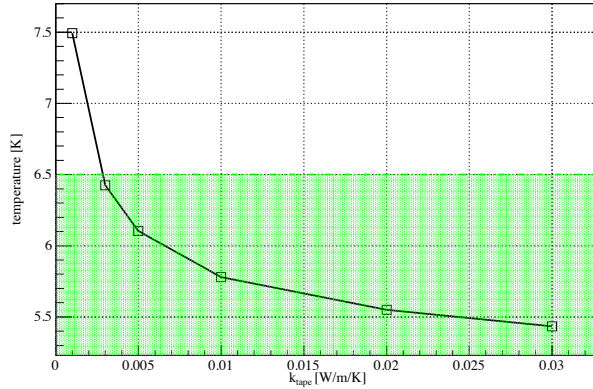


Figure 5.14: the thermal conductivity dependance of insulation tape.

#### 5.2.4 Discussion

As mentioned in previous chapter, different result of neutron production and energy deposition is obtained in terms of different physics model. Nowadays' heat calculation bases on the model of JAM\_INCL\_JENDL. We suppose there is factor of  $\pm 0.3$  in different physics model. The figure 5.15 shows the temperature changes with the factor of energy deposition for 90 day operation. The maximum temperature grows up with factor. Supposed that the energy deposition predicted by the other physics model is higher than JAM\_INCL\_JENDL by factor 1.5, cooling for 30 days is not allowed for phase-II experiment. Thus, the energy deposition and

neutron production is necessary to be checked correctly by using different physics model in future.

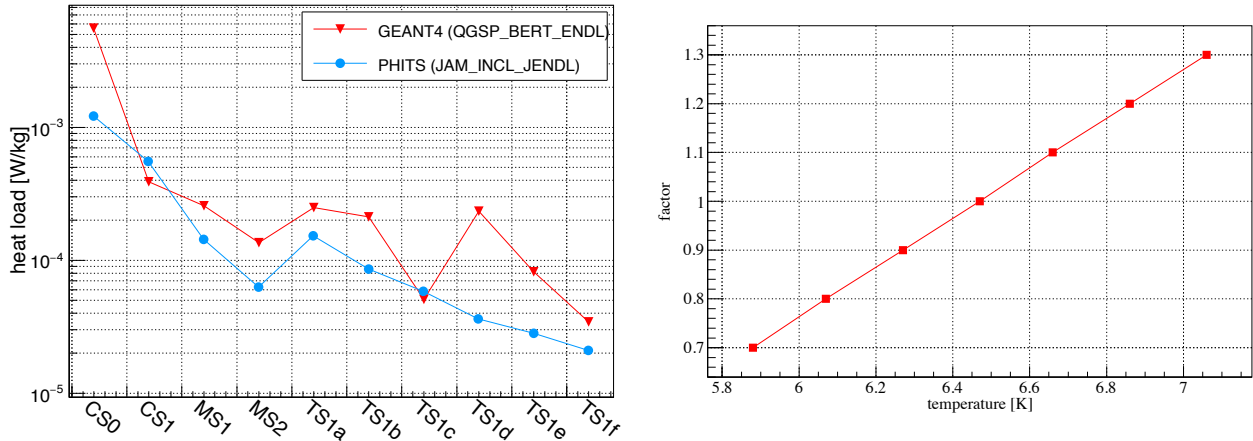


Figure 5.15: The temperature peak increases linearly with the energy deposition factor.

### Improvement of CS1 coil

Due to cooling issue of the CS1 coils, the new scenario should be considered if the CS1 cannot be cooled for a long time. There are two ways to optimize the CS1 coils to enlarge the operating time.

- Using the original design but enlarged the thickness of aluminium strip.
- Separating the CS1 coils to two parts.

As shown in figure 5.16, the maximum temperature calculated with 90 day operation is able to be reduced by increasing the thickness of aluminium strip. If the thickness of aluminium strip can be increased from 1 mm to 2 mm, the peak temperature of 90 day operation is possible to be reduced under current sharing temperature. However, increasing the thickness of aluminium strip may make the coil winding become difficult. It still needs to discuss in future.

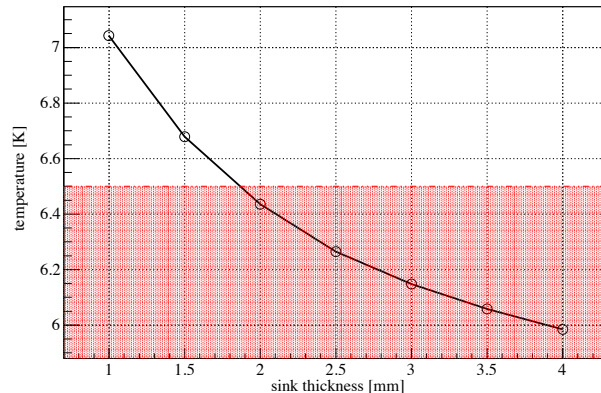


Figure 5.16: The CS1 coils can be optimized by increasing the thickness of aluminium strip.

The second scenario is to separate the CS1 coils to two parts. Since the energy deposition peak in the middle of the CS1 coils, separating the CS1 coils and inserting the aluminium strip in the middle of the CS1 coils, which is shown in figure 5.17, can help CS1 to be cooled down very well.

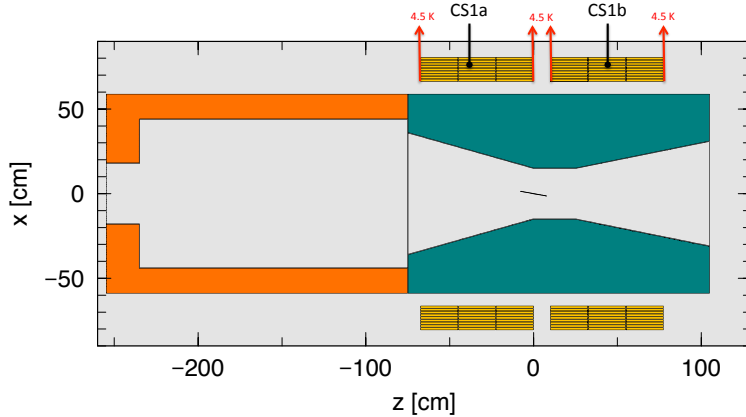


Figure 5.17: The scenario of CS1 seperating.

To validate this scenario, the cooling, quench, magnetic field, muon yield and mechanical issue must be estimated.

# Chapter 6

## Conclusion

To search for the  $\mu^- \rightarrow e^-$  conversion with more precision experimental sensitivity, COMET experiment requires the high intense muon. 8 GeV proton beam with  $4.4 \times 10^{13}$  pps is going to be employed to achieve the high intense muon beam. Thus as the major issue for designing a superconducting magnet system to generate muons, the radiation on COMET superconducting magnet system has been studied in this thesis.

Firstly, radiation on both COMET phase I and phase II are estimated with realasitc geometry by using Monte Carlo code.

- COMET superconducting magnets suffer from  $1.03 \times 10^{10}$  n/cm<sup>2</sup>/sec neutron irradiation ( $> 0.1$  MeV) for phase-II experiment, which corresponds to  $2.49 \times 10^{21}$  n/m<sup>2</sup> neutron fluence totally.
- About 3.74 mSv/h residual radiation is still remained after 1-month operation and 10-month cooling for phase-I experiment.
- A new radiation shield is designed for both phase-I and phase-II experiment to protect CS and MS superconducting coils from the radiation.

Secondly, considering the radiation induced damage on material used in COMET superconducting magnet system, several irradiation tests for GFRPs, quench protection diode, insulation tape and 5N aluminium is carried out.

- The tensile strength of BT is about 375 MPa without irradiation and drops to about 320 MPa after 200 MGy irradiation, which is stronger than G10 and CE
- The forward voltage of quench protection diode increases about 0.08 V after total  $9.7 \times 10^{11}$  n/m<sup>2</sup> neutron irradiation.
- With fitting the cryogenic property of quench protection diode, we estimate its forward voltage will grow up from 0.9 V to about 1.5 V at 210 A and 4.2 K after  $10^{12}$  n/m<sup>2</sup> neutron irradiation, and its temperature rises from 4.2 K to 11 K.
- Among the several samples of insulation tape, BTGK-C has good mechanical property which has tensile strength of 14 MPa.
- The enhanced tensile strength of insulation tape has been observed after 10 MGy irradiation by cobalt source.
- According to the neutron irradiation test of 5N aluminium, the RRR of stabilizer drops lower than 100 after 3-month operation.

Thirdly, due to the degradation of the stabilizer and aluminium strip which may lead to the issue of cooling and quench, the temperature during the cooling is estimated by solving the three dimensional heat equation. As for the most dangerous coil in COMET superconducting magnet system, CS1, which is longest one and close to the production target, its temperature margin is estimated to 6.8 K for 30-day operation which exceeds to the current sharing temperature, 6.5 K. Therefore, to design a superconducting magnet what can operate under the high radiation environment for long time, original design of CS1 solenoid is optimized as follows.

- Shorten the length of aluminium strip from edge of coils to cooling pipe.
- Enlarge the length of inner aluminium strip.
- Insert the aluminium strip into each layer from two sides.

The temperature can be controlled around 5.6 K for 30-day operation with these modifications. As for the quench issue, the maximum temperature of pion capture solenoid is estimated by the worst circumstances. The quench will lead the temperature to 250 K with 500 V power supply if the RRR of aluminium drops to 100. The voltage of power supply should be increased to 600 V to secure the temperature after quench.

Therefore, as for nowadays' design for the superconducting magnets of CS1 coils, 30 day operation is fully possible. However, if the experiment requires for more operation time, the optimization of design should focus on how to cool the CS1 coils efficiently.

# Acknowledgement

本研究を進めるに当たって多くの方にご協力いただきました。この場を借りて感謝を申し上げます。九州大学工学府エネルギー量子工学部門の石橋健二教授には自由に研究できる環境を与えていただき、研究の機会を与えてくださいました。また、修士1年間で研究に関してご指導をいただきました九州大学工学府エネルギー量子工学部門の執行信寛助教に深く感謝致します。高エネ研における一年間で九大の手続きをしてくれて助かりました。研究だけでなく学生生活にも気にかけて下さった九州大学工学府エネルギー量子工学部門の前畠京介准教授及び伊豫本直子准教授に心から感謝します。

修士2年から高エネルギー加速器研究機構に移り、多くの方々によく面倒を見ていただきました。本論文に有益なご助言を頂きました高エネルギー加速器研究機構低温超伝導工学センターの荻津透教授を深く感謝致します。

修士二年間で研究を進める上に多くご助言、直接のご指導をいただきました高エネルギー加速器研究機構素粒子原子核研究所の吉田誠助教に深く感謝致します。

修士課程を入学する前に、COMET 実験に誘っていただきました高エネルギー加速器研究機構低温超伝導工学センターの中本建志教授に心から感謝します。

COMET 超伝導磁石の熱計算やクエンチ計算にご指導をいただきました高エネルギー加速器研究機構低温超伝導工学センターの佐々木憲一准教授に深く感謝します。

超伝導磁石に有益なご助言を頂きました高エネルギー加速器研究機構低温超伝導センターの飯尾雅実助教に深く感謝します。

また、高エネルギー加速器研究機構低温超伝導工学センターの榎本舜特別助教、事務の長井加寿子さん、小瀧えみこさん及びJ-PARC 低温セクション事務の菊池みどりさんに生活や出張手続きを色々手伝って頂き、非常に助かりました。

COMET コラボレーションで、研究にご助言及びご検討を頂きました高エネルギー加速器研究機構素粒子原子核研究所の三原智教授に深く感謝致します。研究の機会のみならず、中国とグルジアでのコラボレーションミーティングの参加に御出資、ありがとうございました、今年もよろしくお願ひします。また、多くご助言を頂きました大阪大学理学研究院物理学専攻の久野良孝教授、佐藤朗助教、板橋隆久博士、坂本英之助教、ロンドン帝国大学(Imperial College London)理学研究院高エネルギー物理グループの Yoshi Uchida 博士、Ajit Kurup 博士に感謝致します。

放射線計算で、PHITS の使い方を教えてくれた日本原子力研究開発機構 PHITS グループの岩元洋介博士、佐藤達彦博士、仁井田浩二博士、橋本慎太郎博士、小川達彦博士、安部晋一郎博士を始めの方々に感謝致します。また、ともに COMET 実験のためのソフトウェア ICEDUST を開発しているロンドン帝国大学(Imperial College London)理学研究院高エネルギー物理グループの Ben Krikler 氏、ロンドン学院大学(Uinversity College London)理学研究院高エネルギー物理専攻の Andrew Edmonds 氏、大阪大学理学研究院物理学専攻の林央樹氏、岡本慧太氏、中国高エネルギー物理研究所の藤井祐樹博

士、中国南京大学理学研究院の Chen Wu 氏を深く感謝致します。照射実験で、多くのご協力及びご指導を頂きました九州大学理学研究院素粒子物理実験専攻の東城順治准教授、山口博史博士、大石航氏、中居勇樹氏を心から感謝致します。

J-PARC に引っ越しした際にチャリンコ屋まで連れていただきました日本原子力研究開発機構の佐藤大樹博士を感謝しますが、次回、置いて帰らないでください。

次は同九州大学石橋研究室の上原春彦氏(現明電舎)、米倉睦人氏(現原子燃料工業)、前田亮氏(現日本原子力研究開発機構)、安部英恵氏(現富士電機)、筋肉シンチレーター氏(現三菱重工業)を始めの先輩方々に感謝致します。また、現石橋研究室の今林洋一先生、安部将史坊主、善本翔太君、川上久雄君、須田翔哉君、板敷祐太郎君、西表優太君、木佐優太君、吉峰郁洋君を感謝致します。

最後、日本への留学を御出資してくれた上海の両親と両親のお金を深く感謝致します。

最後の最後は現役の自分のパソコン Macbook Air Jr. に感謝します。先代の Macbook はグルジアで犠牲したのはとても気の毒でした。また、吉田さんの計算機を感謝致します。ずっと計算ばっかりされてごめんね。

# References

- (1) Broeders, C. and Konobeyev, A., Journal of nuclear materials **328** (2004) 197.
- (2) Collaboration, A., Physics Letters B **716** (2012) 1.
- (3) Thomson, M., *Modern particle physics*, Cambridge university press, Cambridge, UK, 2013.
- (4) data group, P., Particle physics booklet, LBNL and CERN, 2012.
- (5) R.R. Crittenden, e. a., Phys. Rev. **121** (1961) 1823.
- (6) S. Freedman, e. a., Phys. Rev. D **47** (1993) 811.
- (7) R.D. Bolton, e. a., Phys. Rev. Lett. **56** (1986) 2461.
- (8) U. Bellgardt, e. a., Nucl. Phys. B **299** (1988) 1.
- (9) de Gouvea, A. and Vogel, P., Progress in Particle and Nuclear Physics **71** (2013) 75.
- (10) Hincks, E. P. and Pontecorvo, B., Phys. Rev. **73** (1948) 257.
- (11) J. Adam, e. a. M. C., Phys. Rev. Lett. **110** (2013) 201801.
- (12) Collaboration, M., Meg upgrade proposal, Technical report, 2013.
- (13) G. Lynch, J. O. and Rosendorff, S., Phys. Rev. Lett. **1** (1958) 471.
- (14) for the Mu3e Collaboration, N. B., Nucl. Phys. B **248-250** (2014) 25.
- (15) H. Nose, e. a., Journal of Nuclear Science and Technology **42** (2005) 2.
- (16) T. Sato, e. a., J. Nucl. Sci. Technol. **50:9** (2013) 913.
- (17) A. Boudard, e. a., Phys. Rev. C **87** (2013) 014606.
- (18) Y. Sawada, e. a., Nucl. Instr. and Meth. B **291** (2012) 38.
- (19) A. Fassò, e. a., Fluka: present status and future developments, La Biodola, Italy, 1993, IV Int. Conf. on Calorimetry in High Energy Physics.
- (20) F. Ballarini, e. a., Nuclear models in fluka: present capabilities, open problems and future improvements, Stanford, CA, 2004, Nuclear Data for Science and Technology (ND2004).

- (21) V.N. Ivanchenko, e. a., NIM A **502** (2-3) (2003) 666.
- (22) collaboration, M., Mu2e conceptual design report, Technical Report DE-AC02-07-CH-11359, Fermi Nation Accelerator Laboratory, 2012.
- (23) T. Kai, e. a., Validation of radioactivity calculation code system dchain-sp, Düsseldorf-Neuss, Germany, 2003, ICANS-XVI.
- (24) on Radiological Protection, I. C., Annals of ICRP **26** (1996) 3/4.
- (25) M. Brugger, e. a., Radiation Protection Dosimetry **116** (2005) 12.
- (26) Kalia, S. and Fu, S., *Polymers at cryogenic temperatures*, Springer, Berlin Heidelberg, 2013.
- (27) Matsuda, K. and Nagai, S., Appl. Radiat. Isot. **42** (1991) 1215.
- (28) T. Nakamoto, e. a., in *Takasaki advanced radiation research symposium*, volume 2P-2, 2014.
- (29) *Irradiation of quench protection diodes at cryogenic temperatures in a nuclear research reactor*, USA, 1995, ICEC Conference.
- (30) Tsoulfanidis, N., *Measurement and detection of radiation*, Taylor & Francis, Washington, 1995.
- (31) K. Kobayashi, e. a., *Measurement of neutron spectrum at irradiation facilities of Kyoto University Reactor*, 1987.
- (32) Horak, J. and Blewitt, T., Journal of nuclear materials **49** (1973) 161.
- (33) P. Ehrhart, W. S., Phys. Rev. B **8** (1973) 2604.
- (34) P. Ehrhart, H.G. Haubold, W. S., Adv. Solid State Phys. **14** (1974) 87.
- (35) J.B. Roberto, B. Schoenfeld, P. E., Phys. Rev. B **18** (1978) 2591.
- (36) Lucasson, P. and Walker, R., Phys. Rev. **127** (1962) 485.
- (37) Neely, H. and Bauer, W., Phys. Rev. **149** (1966) 535.
- (38) Simpson, H. and Chaplin, R., Phys. Rev. **185** (1969) 958.
- (39) Jung, P., J. Nucl. Mater. **117** (1983) 70.
- (40) Dimitrov, O. and Dimitrov, C., Radiat. Eff. **84** (1985) 117.
- (41) Jung, P., Radiat. Eff. **51** (1980) 249.
- (42) Kittel, C., *Introduction to solid state physics*, John Wiley & Sons, Inc, Tokyo, 1953.
- (43) Touloukian, Y. and Buyco, E., Thermophysical properties of matter, the tprc data series, vol.4: Specific heat metallic elements and alloys, New York, 1971.
- (44) Manfreda, G., *Review of ROXIE's material properties database for quench simulation*, 2011.

- (45) E.S. Drexler, R. R. and Simon, N., Properties of copper and copper alloys at cryogenic temperature, Gaithersburg, 1992, NIST.
- (46) Woodcraft, A., Cryogenics **45(6)** (2005) 421.
- (47) *Thermal conductivity of aluminum, copper, iron and tungsten for temperature from 1 K to the melting point*, Boulder, Colorado, 2013, National Bureau of Standards.
- (48) P.D. Desai, H. J. and Ho, C., J. Phys. Chem. Ref. Data **13(4)** (1984) 1131.
- (49) Corruccini, R., NBS Tech Note **218** (1964).
- (50) Fickett, F., Cryogenics (1971).
- (51) *Properties and preparation of high-purity aluminum*, Boulder, Colorado, National Bureau of Standards.
- (52) P. von Böckh, T. W., *Heat Transfer*, Springer, Heidelberg, 2012.
- (53) D.L. Rule, D. S. and Sparks, L., Cryogenics **36(4)** (1990) 283.
- (54) Kuno, Y. and Okada, Y., Reviews of modern physics **73** (2001) 151.
- (55) Collaboration, T., Physical Review Letters **112** (2014) 061802.
- (56) Y. Kuno, o. b. o. t. C. C., Prog. Theor. Exp. Phys. **022C01** (2013) 1.
- (57) Hisano, J. and Nomura, D., Phys. Rev. D **59** (1999) 116005.
- (58) W. Altmannshofer, e. a., Nuclear Physics B **830** (2010) 17.



# Michel decay

Michel decay is the most dominated decay mode of muon. It can be calculated by Fermi theory, and the muon decay rate can be written as

$$\Gamma(\mu^- \rightarrow e^- \bar{\nu}_e \nu_\mu) = \frac{1}{\tau_\mu} = \frac{G_F^{(e)} G_F^{(\mu)} m_\mu^5}{192\pi^3} \quad (1)$$

where the weak couplings to the electron and muon are  $G_F^{(e)}$  and  $G_F^{(\mu)}$ , respectively. The weak coupling is measured by experiment and can be concluded that  $G_F^{(e)} = G_F^{(\mu)} = G_F^{(\tau)} = 1.16638 \times 10^{-5} GeV^{-2}$ . The muon differential deacay rate is given by (54)

$$\begin{aligned} \frac{d^2\Gamma(\mu^- \rightarrow e^- \nu \bar{\nu})}{dx \cdot d(\cos\theta_e)} = & \frac{m_\mu}{4\pi^3} W_{e\mu}^4 G_F^2 \sqrt{x^2 - x_0^2} \\ & \times [F_{IS}(x) - P_\mu \cos\theta_e F_{AS}(x)] \\ & \times [1 + \vec{P}_e(x, \theta_e) \cdot \hat{\zeta}] \end{aligned}$$

where  $W_{e\mu} = (m_\mu^2 + m_e^2)/2m_\mu$ ,  $x = E_e/W_{e\mu}$  and  $x_0 = m_e/W_{e\mu}$ , respectively.  $\theta_e$  is the angle between the muon polarization  $\vec{P}_\mu$  and the electron momentum  $e^-$ .  $\hat{\zeta}$  is the directional vector of the measurement of electron spin polarization. The function  $F_{IS}(x)$  and  $F_{AS}(x)$  are the isotropic and anisotropic parts of the electron spectrum, which can be written as

$$F_{IS}(x) = x(1-x) + \frac{2}{9}\rho(4x^2 - 3x - x_0^2) + \eta_0(1-x) \quad (2)$$

$$F_{AS}(x) = \frac{1}{3}\epsilon\sqrt{x^2 - x_0^2}\{1 - x + \frac{2}{3}\delta[4x - 3 + (\sqrt{1 - x_0^2} - 1)]\} \quad (3)$$

where  $\rho, \eta, \epsilon, \delta$  are called Michel parameters. In Standard model, they are  $\rho = \frac{3}{4}, \eta = 0, \epsilon = 1$  and  $\delta = \frac{3}{4}$ , while, the experimental values are

$$\rho = 0.7518 \pm 0.0026, \eta = -0.007 \pm 0.013, \delta = 0.7486 \pm 0.0038, \epsilon = 1.0027 \pm 0.0084 \quad (4)$$

which the SM value is very close to the experimental value.



# cLFV in Standard Model

The most popular explanation of charged lepton flavor violation in Standard model is one W boson is emitted through the neutrino oscillation<sup>(55)</sup> of  $\nu_\mu \rightarrow \nu_e$ . Feynman diagram of  $\mu^- \rightarrow e^- \gamma$  is shown in figure 1.

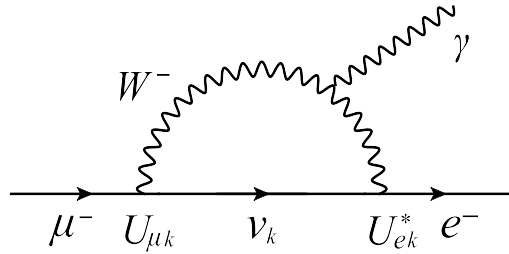


Figure 1: Feynman diagram of  $\mu^- \rightarrow e^- \gamma$  predicted by massive neutrino. cLFV occurs through a neutrino oscillation, and  $\gamma$  is emitted from a  $W^-$

The treatment of neutrino oscillation for three flavors is developed by  $3 \times 3$  PMNS matrix with mixing angle, which is written as

$$\begin{pmatrix} \nu_e \\ \nu_\mu \\ \nu_\tau \end{pmatrix} = \begin{pmatrix} U_{e1} & U_{e2} & U_{e3} \\ U_{\mu 1} & U_{\mu 2} & U_{\mu 3} \\ U_{\tau 1} & U_{\tau 2} & U_{\tau 3} \end{pmatrix} \begin{pmatrix} \nu_1 \\ \nu_2 \\ \nu_3 \end{pmatrix} \quad (5)$$

To solve the neutrino oscillation, we start from the time evolution of the wave function, which is determined by the time evolution of the mass eigenstates and can be written as

$$|\psi(\mathbf{x}, t)\rangle = U_{\mu 1}^* |\nu_1\rangle e^{-i\phi_1} + U_{\mu 2}^* |\nu_2\rangle e^{-i\phi_2} + U_{\mu 3}^* |\nu_3\rangle e^{-i\phi_3} \quad (6)$$

using the PMNS matrix, the probability of  $\nu_\mu \rightarrow \nu_e$  can be described as

$$P(\nu_\mu \rightarrow \nu_e) = |\langle \nu_e | \psi(\mathbf{x}, t) \rangle|^2 = -4 \sum_{k=1,2,3} U_{ek} U_{\mu k}^* \sin^2(\Delta_{ji}) \quad (7)$$

where  $\Delta_{ji} = (\phi_j - \phi_i)/2 = (m_j^2 - m_i^2) \cdot L/4E_\nu$ .  $L$  is the neutrino oscillation occurring distance and  $(m_j^2 - m_i^2)$  is the difference between the square of neutrino mass. Thus, the decay rate of  $\nu_\mu \rightarrow \nu_e$  is fixed

by involving the neutrino oscillation and given by

$$\begin{aligned}\Gamma(\mu^- \rightarrow e^- + \gamma) &= \frac{G_F^2 m_\mu^5}{192\pi^3} \frac{\alpha}{2\pi} P(\nu_\mu \rightarrow \nu_e) \\ &\simeq \frac{G_F^2 m_\mu^5}{192\pi^3} \frac{\alpha}{2\pi} |U_{e3} U_{\mu 3}^* \frac{\Delta m^2}{m_W^2}|^2\end{aligned}\quad (8)$$

where  $\alpha$ ,  $m_W$  is the fine structure constant and the mass of W boson. The ratio of the partial width  $\Gamma(\mu^- \rightarrow e^- \gamma)$  to the Michel decay rate gives the branching ratio

$$Br(\mu^- \rightarrow e^- \gamma) = \frac{\Gamma(\mu^- \rightarrow e^- + \gamma)}{\Gamma(\mu^- \rightarrow e^- \bar{v}_e v_\mu)} = \frac{\alpha}{2\pi} |U_{e3} U_{\mu 3}^* \frac{\Delta m^2}{m_W^2}|^2 < 10^{-54} \quad (9)$$

# cLFV in supersymmetry

Supersymmetry (SUSY) is the most possible candidate in the physics beyond the Standard model, which can explain the hierarchy problem and Higgs' mass perfectly. It is a proposed extension of SM by including the superpartner for each particle. For instance, each fermion has its superpartner, boson, and vice versa. In the prediction of SUSY model which shown in figure 2, the cLFV is occurred by the slepton mixing.

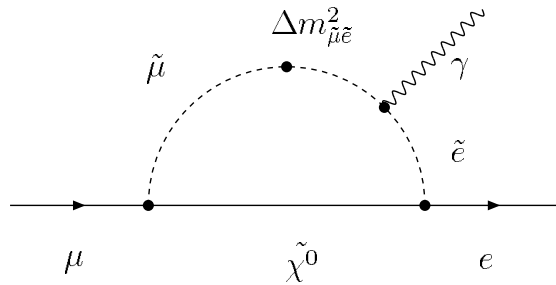


Figure 2: Feynman diagram of  $\mu^- \rightarrow e^- \gamma$  predicted by slepton mixing. it occurs through its superpartner  $\tilde{\mu}$  and  $\tilde{e}$  mixing.

The branching ratio of  $\mu \rightarrow e\gamma$  is given similarly to the SM by <sup>(56)</sup>

$$Br(\mu \rightarrow e\gamma) = \frac{\alpha}{2\pi} \left| \sum_k \tilde{U}_{ek} \tilde{U}_{\mu k}^* \frac{\Delta m_k^2}{m_S^2} \right|^2 \left( \frac{m_W}{m_S} \right)^4 \quad (10)$$

where  $m_S$  is the typical scale of scalar masses,  $\tilde{U}$  is the mixing matrix between sleptons and leptons, and  $\Delta m_k^2$  is the square of mass difference between the  $k$ th and 1st sleptons.

From figure 2, the mixing  $\Delta m_{e\tilde{\mu}}^2$  between a smuon  $\tilde{\mu}$  and a selectron  $\tilde{e}$  plays a key role in cLFV. This slepton mixing parameter,  $\Delta m_{e\tilde{\mu}}^2$  is given by the slepton mass matrix  $m_{\tilde{l}}^2$

$$(m_{\tilde{l}}^2)_{ij} = (m_l m_l^\dagger)_{ij} + (\tilde{m}_l^2)_{ij} = \begin{pmatrix} m_{e\tilde{e}}^2 & \Delta m_{e\tilde{\mu}}^2 & \Delta m_{\tilde{e}\tilde{\tau}}^2 \\ \Delta m_{\tilde{\mu}\tilde{e}}^2 & m_{\tilde{\mu}\tilde{\mu}}^2 & \Delta m_{\tilde{\mu}\tilde{\tau}}^2 \\ \Delta m_{\tilde{\tau}\tilde{e}}^2 & \Delta m_{\tilde{\tau}\tilde{\mu}}^2 & m_{\tilde{\tau}\tilde{\tau}}^2 \end{pmatrix} \quad (11)$$

where  $(m_l m_l^\dagger)_{ij}$  is the lepton mass matrix and  $(\tilde{m}_l^2)_{ij}$  is the term of SUSY breaking, respectively. As the scenario of SUSY, SUSY-GUT and SUSY-Seasaw contribute to the off-diagonal terms.

## SUSY-GUT

Supersymmetric grand unified theories (SUSY-GUT) is the extension of grand unified theories with supersymmetry. Three gauge coupling constants of electromagnetic, weak and strong interaction are unified to SU(5) coupling constant at scale of  $10^6$  GeV, which is also called GUT scale. Due to the generation of the off-diagonal elements in slepton mass matrix, the cLFV is occurred with big branching ratio.  $\Delta m_{\tilde{\mu}\tilde{e}}^2$  is given by

$$\Delta m_{\tilde{\mu}\tilde{e}}^2 \propto \frac{3m_0^2 + A_0^2}{8\pi^2} h_t^2 V_{td}^* V_{ts} \ln \frac{M_{GUT}}{M_{R_3}} \quad (12)$$

where  $m_0$  and  $A_0$  are the universal scalar mass and the universal trilinear coupling respectively.  $V_{td}$  and  $V_{ts}$  are the elements in the CKM matrix.  $M_{R_3}$  is the mass of the right-hand neutrino.  $M_{GUT}$  is the GUT scale ( $\approx 2 \times 10^{18}$  GeV). and  $h_t$  is the Yukawa coupling constant of top quark. Figure 3 shows the prediction of the branching ratio of  $\mu \rightarrow e$  conversion with Ti target in SUSY-GUT model (54), which is higher than the prediction of SM with the order of 1040. Here,  $m_{\tilde{e}_R}$  is the mass of right-hand electron, and  $\mu$  is the parameter defined by Higgs and Higgsino.

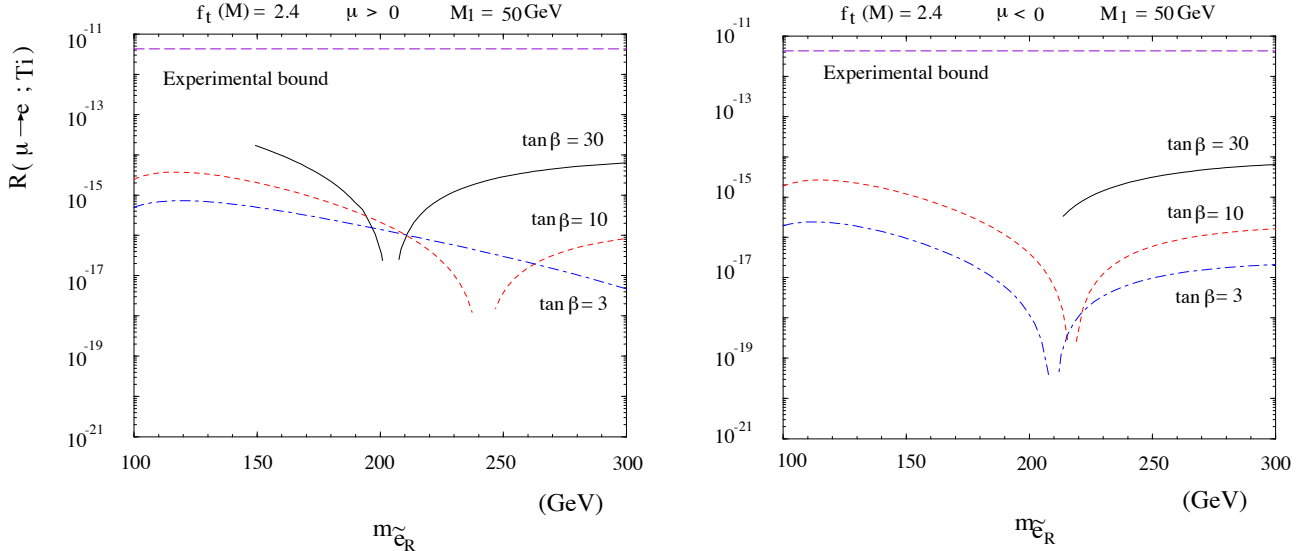


Figure 3: Prediction of branching ratio of  $\mu \rightarrow e$  conversion in SUSY-GUT SU(5). Mass of right-hand  $\tilde{e}$  can be observed indirectly if the  $\mu \rightarrow e$  conversion experiment gets more precision sensitivity.

## SUSY-Seasaw

SUSY-Seasaw model is another scenario for the prediction of cLFV by including the right-hand neutrino. From the right-hand neutrino mass term, the slepton mixing can be obtained as well. The slepton mixing between muon and electron depends on the solar neutrino oscillation and atmospheric neutrino oscillation (57). Thus,  $\Delta m_{\tilde{\mu}\tilde{e}}^2$  can be written as

$$\Delta m_{\tilde{\mu}\tilde{e}}^2 \propto \frac{3m_0^2 + A_0^2}{8\pi} h_\tau^2 U_{\tau e}^* U_{\tau \mu} \ln \frac{M_{GUT}}{M_{R_3}} \quad (13)$$

where  $U_{\tau e}^*$  and  $U_{\tau \mu}$  are the elements of PMNS matrix.  $h_\tau$  is the Yukawa coupling constant of  $\tau$ . The prediction of branching ratio of  $\mu \rightarrow e\gamma$  by SUSY-Seasaw is given in figure 4. Similar to the prediction of

SUSY-GUT model, it also predicts the higher branching ratio for cLFV.

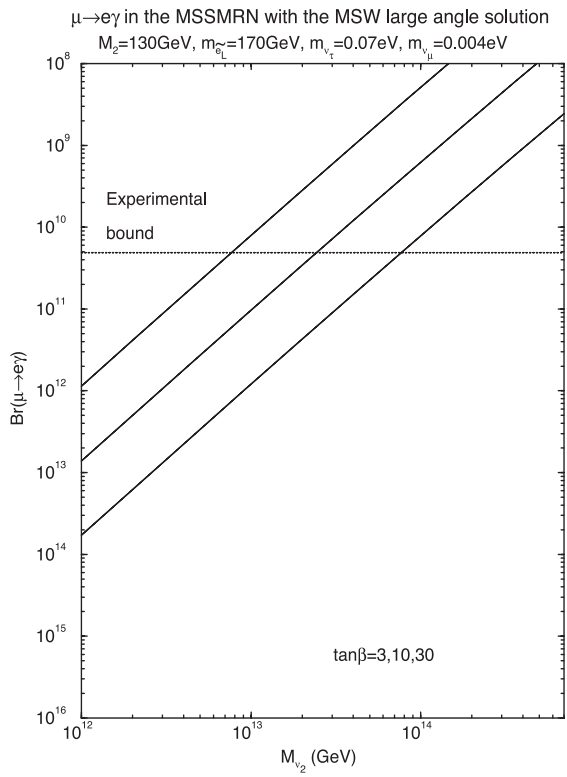


Figure 4: Prediction of branching ratio of  $\mu \rightarrow e\gamma$  in SUSY-Seasaw model.



# Impact of cLFV

Because of the higher branching ratio predicted by BSM, in addition, the branching ratio depends on the experimental sensitivity, the discovery of cLFV plays an important role in seeking for the BSM. In W. Altmannshofer's paper, the sensitivities of several flavor observables to a variety of BSM models are listed in figure 5.

"DNA" of flavour physics effects for the most interesting observables in a selection of SUSY and non-SUSY models  
★★★ signals large effects, ★☆ visible but small effects and ★ implies that the given model does not predict sizable effects in that observable.

	AC	RVV2	AKM	$\delta LL$	FBMSSM	LHT	RS
$D^0 - \bar{D}^0$	<span style="color:red">★★★</span>	<span style="color:black">★</span>	<span style="color:black">★</span>	<span style="color:black">★</span>	<span style="color:black">★</span>	<span style="color:red">★★★</span>	?
$\epsilon_K$	<span style="color:black">★</span>	<span style="color:red">★★★</span>	<span style="color:red">★★★</span>	<span style="color:black">★</span>	<span style="color:black">★</span>	<span style="color:blue">★☆</span>	<span style="color:red">★★★</span>
$S_{\psi\phi}$	<span style="color:red">★★★</span>	<span style="color:red">★★★</span>	<span style="color:red">★★★</span>	<span style="color:black">★</span>	<span style="color:black">★</span>	<span style="color:red">★★★</span>	<span style="color:red">★★★</span>
$S_{\phi K_S}$	<span style="color:red">★★★</span>	<span style="color:blue">★☆</span>	<span style="color:black">★</span>	<span style="color:red">★★★</span>	<span style="color:red">★★★</span>	<span style="color:black">★</span>	?
$A_{CP}(B \rightarrow X_S \gamma)$	<span style="color:black">★</span>	<span style="color:black">★</span>	<span style="color:black">★</span>	<span style="color:red">★★★</span>	<span style="color:red">★★★</span>	<span style="color:black">★</span>	?
$A_{7,8}(B \rightarrow K^* \mu^+ \mu^-)$	<span style="color:black">★</span>	<span style="color:black">★</span>	<span style="color:black">★</span>	<span style="color:red">★★★</span>	<span style="color:red">★★★</span>	<span style="color:blue">★☆</span>	?
$A_9(B \rightarrow K^* \mu^+ \mu^-)$	<span style="color:black">★</span>	?					
$B \rightarrow K^{(*)} \nu \bar{\nu}$	<span style="color:black">★</span>						
$B_s \rightarrow \mu^+ \mu^-$	<span style="color:red">★★★</span>	<span style="color:black">★</span>	<span style="color:black">★</span>				
$K^+ \rightarrow \pi^+ \nu \bar{\nu}$	<span style="color:black">★</span>	<span style="color:red">★★★</span>	<span style="color:red">★★★</span>				
$K_L \rightarrow \pi^0 \nu \bar{\nu}$	<span style="color:black">★</span>	<span style="color:red">★★★</span>	<span style="color:red">★★★</span>				
$\mu \rightarrow e \gamma$	<span style="color:red">★★★</span>						
$\tau \rightarrow \mu \gamma$	<span style="color:red">★★★</span>	<span style="color:red">★★★</span>	<span style="color:black">★</span>	<span style="color:red">★★★</span>	<span style="color:red">★★★</span>	<span style="color:red">★★★</span>	<span style="color:red">★★★</span>
$\mu + N \rightarrow e + N$	<span style="color:red">★★★</span>						
$d_n$	<span style="color:red">★★★</span>	<span style="color:red">★★★</span>	<span style="color:red">★★★</span>	<span style="color:blue">★☆</span>	<span style="color:red">★★★</span>	<span style="color:black">★</span>	<span style="color:red">★★★</span>
$d_e$	<span style="color:red">★★★</span>	<span style="color:red">★★★</span>	<span style="color:blue">★☆</span>	<span style="color:black">★</span>	<span style="color:red">★★★</span>	<span style="color:black">★</span>	<span style="color:red">★★★</span>
$(g-2)_\mu$	<span style="color:red">★★★</span>	<span style="color:red">★★★</span>	<span style="color:blue">★☆</span>	<span style="color:red">★★★</span>	<span style="color:red">★★★</span>	<span style="color:black">★</span>	?

Figure 5: The size of the observable flavor effect for a variety of SUSY and non-SUSY models.

where AC, RVV2, AKM,  $\delta LL$ , FBMSSM, LHT and RS are Abelian U(1) flavor symmetry model, non-Abelian model, Antusch-King-Malinsky SU(3) flavor symmetry model, flavor models with pure CKM-like left handed currents, flavor-blind MSSM, little Higgs with T-parity and Randall-Sundrum model <sup>(58)</sup>. In all these decay modes,  $\mu \rightarrow e$  conversion and  $\mu \rightarrow e \gamma$  contributes a large effect on every theory, which means the BSM is easy to be found in these two modes with high probability.



# Magnetic field interpolation

Suppose there is field map, it only gives us the coordinate ( $x, y, z$ ), magnetic field vector ( $B_x, B_y, B_z$ ) and magnetic field ( $B$ ), so we have many points with magnetic field. If the particle goes through this point, the magnetic field is already there. However, the magnetic field has to be interpolated when the particle goes through the point we haven't. The simple way to interpolate the field is to weight the field in a box.

There is box which vertices are the known coordinate of field map. Each vertices can be written as

$$\begin{aligned}
 \vec{r}_1 &= (x_{lt}, y_{lt}, z_{lt}) \\
 \vec{r}_2 &= (x_{gt}, y_{lt}, z_{lt}) \\
 \vec{r}_3 &= (x_{gt}, y_{gt}, z_{lt}) \\
 \vec{r}_4 &= (x_{gt}, y_{gt}, z_{gt}) \\
 \vec{r}_5 &= (x_{lt}, y_{gt}, z_{lt}) \\
 \vec{r}_6 &= (x_{lt}, y_{gt}, z_{gt}) \\
 \vec{r}_7 &= (x_{lt}, y_{lt}, z_{gt}) \\
 \vec{r}_8 &= (x_{gt}, y_{lt}, z_{gt})
 \end{aligned} \tag{14}$$

where the  $x_{gt}$  is the greater value and  $x_{lt}$  is the less value along the x direction. Thus, the weight of x, y and z axis in this box can be written as

$$t = \frac{x_0 - x_{lt}}{x_{gt} - x_{lt}}, \quad u = \frac{y_0 - y_{lt}}{y_{gt} - y_{lt}}, \quad v = \frac{z_0 - z_{lt}}{z_{gt} - z_{lt}} \tag{15}$$

where  $(x_0, y_0, z_0)$  is the position of the particle and  $(t, u, v)$  is the weight on this position.  $(x_0, y_0, z_0)$

must be inside this box. Therefore, the magnetic field of this position is

$$\begin{aligned}
 B_i(\vec{r}_0) = & (1-t)(1-u)(1-v)B_i(\vec{r}_1) \\
 & + (1-u)(1-v)tB_i(\vec{r}_2) \\
 & + tu(1-v)B_i(\vec{r}_3) \\
 & + tuvB_i(\vec{r}_4) \\
 & + (1-t)u(1-v)B_i(\vec{r}_5) \\
 & + (1-t)uvB_i(\vec{r}_6) \\
 & + (1-t)(1-u)vB_i(\vec{r}_7) \\
 & + t(1-u)vB_i(\vec{r}_8)
 \end{aligned} \tag{16}$$

$(x_{lt} \leq x_0 \leq x_{gt}, y_{lt} \leq y_0 \leq y_{gt}, z_{lt} \leq z_0 \leq z_{gt})$